Experimental Measurements of Turbulent Heat Fluxes over Melting Ice

Sheldon Harrison
Department of Mechanical Engineering

McGill University, Montreal

September 2022

A thesis submitted to McGill University in partial fulfillment of the requirements of the degree of

Master of Science

© Sheldon Harrison, 2022

DEDICATION

To my family: Dilys, Jordan, Keenan, Joe, and Rowena, who have always supported me everywhere my studies have taken me.

Since there is always another level to learn, mastery actually means that you're a master of what you know, and an apprentice of what you don't. We become masters of what is behind us, and apprentices of what is ahead.

– Gary Keller *(The One Thing)*

ACKNOWLEDGEMENTS

At long last, an era of university has ended! First and foremost, I would like to thank Professor Mydlarski, who was always available to offer helpful advice, valuable insight, and (on occasion) even a good joke. Besides being an excellent supervisor in general, you have taught me to strive for a level of quality in my work that did not exist before.

I would also like to thank everyone in the Aerodynamics Laboratory here at McGill. I would like to especially thank: Sam Lortie, for training me in the lab (et m'apprendre quelques mots Quebecois!); Dr. Hewes, for answering every lab-related question I could come up with, or just commiserating about the life of a hot-wire user; Milind Singh, for being a friend from afar throughout this pandemic-infused degree; and Ben Brown, for both helping with my experiments (perhaps not by choice) and keeping me motivated during the final push for my thesis.

Outside of the lab, I would like to extend my gratitude to some exceptional people in the McGill community: Greg Doyle, who ensured that everything ran smoothly administratively, while also offering good conversation during quiet office hours; Professor Frost, who showed a kindness that made McGill feel more like home; and David Speller from the School of Architecture, who machined the MDF pieces for the wind tunnel. Furthermore, I am grateful to Professor Meyer of Dartmouth University, who provided insight into the world of glaciology and helped shape the direction of this project.

I would like to thank the Natural Sciences and Engineering Research Council of Canada and McGill University for providing financial support during my studies.

Last, but certainly not least, I would like to thank all of my family and friends, from the 514, to the 613, back to the 416, without whose support I would not be able to finish this degree. A special thanks to Josh Medicoff, for helping to edit my French abstract. Most importantly, I would like to thank my girlfriend, Nora Wong, for her endless love, support, and patience in everything I do.

CONTRIBUTION OF AUTHORS

This thesis is written in the traditional monograph style, consisting of five chapters and three appendices. I would like to declare that I am the sole author of each of these chapters and appendices, and therefore the sole author of this thesis as a whole. My supervisor, Professor Mydlarski, provided guidance, comments, and editorial revisions of the thesis.

ABSTRACT

As the effects of climate change grow increasingly significant across the globe, it has been shown that Canada is warming 2-3 times faster than the rest of the world. This is largely due to rapidly melting glaciers in Canada's arctic, which hold the greatest potential contribution from Canadian territory to global sea level increases and make the need for accurate glacier melt predictions critical. One of the most prominent models makes use of a surface energy balance, in which sensible turbulent heat fluxes play an important role. Since their complexity makes them difficult to model, and direct measurements of turbulent heat fluxes over real glaciers are both rare and impractical, this work attempts to understand the velocity and temperature fields over melting ice, and parameterize the turbulent heat fluxes in a controlled setting to improve glacier melt predictions. To this end, hot-wire anemometry and cold-wire thermometry were used to make simultaneous measurements of two-components of velocity and temperature fluctuations above a melting glacier model in a series of wind tunnel experiments. Probability density functions (PDFs), spectra, joint PDFs, and coherence spectra were used to compare the velocity field measured over melting ice to those of a similar flow in the absence of ice. Comparison of their statistics showed that the ice's presence decreased the magnitude of the Reynolds stresses and vertical velocity variance as expected, but also increased the streamwise velocity variance – an observation that has not been previously noted in stably stratified flows over solid surfaces. The transient evolutions of the locally-averaged temperature-related statistics throughout the melt process were also investigated, where it was found that their evolutions were similar when non-dimensionalized by the initial local average. The temperature and combined velocity-temperature fields were evaluated at an equivalent non-dimensional time during the melt process, in which the PDFs and spectra of the temperature field, and joint PDFs and coherence spectra of the vertical velocity and temperature were evaluated. Lastly, a novel method was developed for predicting the turbulent heat flux over melting ice which offers improved accuracy when compared to the most common existing method used in field studies.

RÉSUMÉ

Les effets mondiaux du changement climatique deviennent de plus en plus importants, et le Canada se réchauffe de deux à trois fois plus rapidement que d'autres pays. Cette conséquence importante est attribuée à la fonte accélérée des glaciers de l'Arctique canadien, qui i) détient la plus grande contribution canadienne potentielle à l'augmentation du niveau global de la mer et ii) démontre l'importance de pouvoir prédire (de manière précise) la fonte des glaciers. Pour y parvenir, un bilan énergétique de surface, dans lequel les flux de chaleur turbulents sensibles jouent un rôle important, se trouve au sein d'un des modèles de prédiction de fonte des glaciers le plus célèbres. Étant donné i) la complexité de la modélisation des flux de chaleur turbulents au-dessus des glaciers, et ii) que la mesure de tels flux sont à la fois rares et difficiles, ce travail vise, par conséquent, une meilleure compréhension des champs de vitesse et de température au-dessus de glaciers fondants et de paramétrer les flux de chaleur turbulents dans une étude contrôlée, pour améliorer les prévisions de fonte des glaciers. À cette fin, l'anémométrie à fil chaud et la thermométrie à fil froid ont été utilisées pour effectuer des mesures simultanées de deux composantes de vitesse et de température au-dessus d'un modèle de glacier dans une série d'expériences en soufflerie. Des fonctions de densité de probabilité (PDF), spectres, PDFs joints et des spectres de cohérence ont servi à comparer le champ de vitesse mesuré au-dessus de la glace fondante à un écoulement similaire au-dessus d'une surface solide refroidie. Cette comparaison a démontré que la glace diminuait l'ampleur des tensions de Reynolds et de la variance de la vitesse verticale, comme prévu, mais augmentait également la variance de la vitesse dans la direction principale de l'écoulement – une observation originale qui se distingue des écoulements stratifiés de manière stable au-dessus de surfaces solides. Les évolutions transitoires des statistiques de température (moyennées de manière locale) pendant la fonte de la glace ont également été étudiées. Il a été constaté que leurs évolutions étaient similaires lorsqu'elles étaient adimensionnées par leurs moyennes locales initiales respectives. Pendant la période de fonte de la glace, les champs de température et de vitesse-température combinés ont été évalués à un temps

adimensionnel équivalent par moyen de PDFs, spectres du champ de température, PDFs joints et spectres de cohérence de la vitesse verticale et de la température. En dernier lieu, une nouvelle approche pour la prédiction de flux de chaleur turbulent au-dessus de la glace fondante a été développée. Cette méthode offre une précision améliorée par rapport à la méthode actuelle la plus courante.

Contents

List of Figures

List of Tables

Chapter 1:

Introduction

1.1 Background and Motivation

As the effects of climate change become increasingly relevant to the lives of people across the globe, the need for accurate climate prediction models is critical. In a Canadian context, loss of perennial snowfields and accelerated glacier melt is causing Canada to warm two to three times faster than the rest of the world (Natural Resources Canada, 2019). Canada's melting ice caps, which drain to the Arctic ocean, hold the greatest potential contribution from Canadian territory to global sea level increases (Radić et al., 2014). Mountainous glaciers in Western Canada are an important source of meltwater runoff (Bash & Marshall, 2014) and hold significant influence over water availability in downstream areas extending far beyond the source.

To reliably predict the melting of glaciers and perennial snowfields, accurate models of the heat fluxes occurring between the glacier surface and environment are required. However, these interactions are extremely complex, involving different energy sources and sinks that govern the melt process, making them difficult to model accurately. One of the most common models for predicting glacier melt involves the use of a surface energy balance, which is given by:

$$0 = Q_N + Q_H + Q_L + Q_G + Q_R + Q_M. \tag{1.1}$$

It accounts for the net heat fluxes from solar radiation (Q_N), sensible heat fluxes from convection (Q_H), latent heat fluxes from evaporation and condensation at the surface (Q_L), heat flux to the ground via conduction (Q_G), and heat fluxes caused by rainfall (Q_R). Since they are both transported by turbulent velocity fluctuations in the air above the surface, the sensible and latent heat fluxes are often together referred to as "turbulent

heat fluxes" by the glaciology community. The sum of the aforementioned components in the surface energy balance determines the total amount of energy available for melting the glacier's ice (Q_M).

To predict glacier melt, it is crucial to accurately quantify each of the different heat fluxes in the surface energy budget. In real-world glacier environments, the dominant term is the net radiation term, followed by the sensible heat flux term, which can contribute up to 20-40% of the melt energy (Denby & Greuell, 2000). Moreover, the importance of the turbulent fluxes in the surface energy budget increases during situations where radiative fluxes are reduced, such as in cloudy conditions. Although the radiative heat fluxes are generally well-understood and have adequate models (Fitzpatrick, Radić, & Menounos, 2017), there exists a demonstrated need for improved modelling of turbulent heat fluxes, as current methods can significantly under- or over-estimate overall glacier melt by poor estimations of sensible heat fluxes, which tend to be much larger than latent heat fluxes (Suter, Hoelzle, & Ohmura, 2004). It also bears noting that because the models for latent fluxes are similar to those for sensible fluxes, improvements to sensible heat flux modelling will likely also improve latent heat flux modelling.

There presently exist three primary methods for estimating sensible heat fluxes over melting glaciers in field experiments. They are discussed in detail in section 2.5, but a brief introduction is provided below.

The most accurate method for measuring sensible heat fluxes is by measurement of simultaneous time series of temperature and (three-dimensional) velocity, which are used to directly calculate the sensible heat flux. In the glaciology community, this method is known as the eddy-covariance or eddy-correlation method, and generally uses sonic anemometers to make accurate, high-frequency measurements of velocity. Although it is the most accurate method, the required equipment is expensive, difficult to maintain, and delicate, making it impractical for widespread use in harsh polar climates (Chambers et al., 2020; Hock, 2005).

Due to the difficulties associated with the eddy covariance method, the aerodynamic

profile method (herein referred to as simply the profile method) was derived as a way to estimate the sensible heat fluxes using the theories of Prandtl (1935) and Monin and Obukhov (1954). It assumes pre-determined shapes of the velocity and temperature profiles in the atmospheric boundary layer that are fit to actual conditions using measurements of velocity and temperature taken at two or more heights above the glacier's surface. However, this method is prone to measurement error (Hock, 2005), and tends to under-estimate the sensible fluxes (Denby & Greuell, 2000). Furthermore, the underlying assumptions for the theory surrounding the profile method are typically not valid for true glacier flow, due to the presence of a local wind speed maximum caused by katabatic (downslope) flows (Oerlemans & Grisogono, 2002).

The final and most common method for estimating the sensible heat fluxes is known as the bulk method. This method is built upon the profile method, but is further simplified by way of assumptions regarding the surface topography and temperature, such that only one measurement height is necessary. Using the bulk method, sensible heat flux calculations can easily be made with commercially available automated weather stations, which are simple and robust, thus making the bulk method the most popular choice for the estimation of sensible heat fluxes (Chambers et al., 2020). Besides sharing the relatively weak theoretical foundations of the profile method when applied to glacier melting, the bulk method is also exceptionally sensitive to a scaling parameter known as the roughness length (Hock, 2005), which is usually on the order of 10^3 times smaller than the measurement height, making it difficult to quantify accurately.

Despite the obvious importance of accurate glacier melt predictions, researchers and modellers alike are limited by the current offerings of the three methods described above. Unless new technology is developed that allows for both low-cost and high-frequency measurement of three components of velocity in extreme environments, applicability of the eddy covariance method is not likely to improve. The profile method stands in the shadow of the bulk method, which offers better accuracy with fewer operational requirements (Munro, 1989). It would therefore seem that improvements to sensible

heat flux modelling should be derived from the bulk method (or at least from a method that maintains the same, low operational requirements). Radić et al. (2017) suggested that improvements to the current accuracy of the bulk method will only come from improvements to the underlying theory, as opposed to increased measurement accuracy or fine-tuning of existing model parameters.

Given the above, the main motivation of the present research is to experimentally measure and investigate the turbulent velocity and temperature fields over melting ice in a controlled laboratory setting, with the hopes of improving physics-based modelling of glacier melting using direct measurements of the sensible heat fluxes obtained through a series of wind tunnel experiments. Performing these experiments in a controlled environment provides several advantages and opportunities that are not present in field studies.

First, hot-wire anemometry and cold-wire thermometry measurements of two components of velocity and temperature (respectively) can be made at much higher temporal and spatial resolutions than possible in field experiments, providing valuable insight into the small-scale physics of the turbulent fluxes of momentum and heat.

Second, a scaled glacier model (i.e., extended patch of ice) can be studied over its entire melt period, whereby the surface that is initially at a sub-zero temperature is warmed to $0°C$ and undergoes surface melting until a significant portion has turned to water. Measurements performed over an extended period of time can provide valuable insight into the transient evolution of sensible heat fluxes and other relevant statistical quantities over a surface undergoing phase change.

Lastly, due to variability in weather (such as cloud cover, temperature, etc.), isolating the effects of sensible and latent heat fluxes from radiation and conduction effects is near-impossible in real-world observations. However, in experiments that are performed indoors, in a controlled laboratory setting, the net radiative and conductive fluxes would be nearly constant, allowing for direct investigation of the sensible heat fluxes over melting ice.

In summary, existing models for estimation of the contribution of turbulent heat fluxes to the surface energy balance for a melting glacier can benefit from improvement to facilitate accurate prediction of glacier melting. The present work uses a series of wind tunnel experiments to better understand the physics of convective heat transfer to melting ice, and to improve the most common method used by glaciologists for estimating sensible turbulent heat fluxes.

1.2 Objectives

Having described the background and motivation for this research, its specific objectives are to:

1. Produce a series of turbulent flows similar to those typically seen over glaciers.
2. Design and build a wind tunnel test section containing an extended ice patch that can serve as a model of a glacier.
3. Perform direct measurements of sensible heat fluxes over melting ice in a controlled laboratory setting.
4. Evaluate the transient evolution of statistics of velocity and temperature throughout the melting process.
5. Investigate the statistics of velocity and temperature over a phase-changing surface in the presence of stable stratification.
6. Compare the predictions of the bulk method for estimating sensible heat fluxes to directly measured quantities.
7. Improve or modify the bulk method to provide similar accuracy to its existing form, while reducing sensitivity to the aerodynamic roughness length.

The steps taken to accomplish these objectives will be described in the following chapters.

1.3 Thesis Organization

This section briefly describes the organization of the rest of this thesis, which is as follows. Chapter 2 discusses the relevant theoretical background regarding turbulent flows, and reviews the current literature in the field of glaciology regarding sensible heat flux modelling and observations. Chapter 3 discusses the experimental apparatus, instrumentation, and procedures used for this work. Chapter 4 contains the experimental results and corresponding discussion. Lastly, Chapter 5 offers conclusions and recommendations for future work.

Chapter 2:

Theoretical Background and Literature Review

2.1 Turbulent Flows

Most natural and industrial flows are turbulent in nature – including the flow in the atmospheric boundary layer over glaciers. This large-scale atmospheric flow drives convective heat transfer between the air and glacier's surface. To better understand and model the contributions of convective heat transfer to glacier melting, it is critical to understand the nature of the flow in the highly turbulent atmospheric boundary layer.

Turbulent flows are characterized by their high irregularity, or randomness. They contain a continuum of superimposed scales, and typically arise at a high Reynolds number – a non-dimensional quantity representing the ratio of inertial to viscous forces in a fluid flow, defined as:

$$Re \equiv \frac{Ul}{\nu}, \tag{2.1}$$

where U is a characteristic velocity of the flow, l is a characteristic length scale, and ν is the kinematic viscosity of the fluid. Turbulent flows are diffusive in nature, having a strong ability mix (or diffuse) vector or scalar quantities such as momentum or heat, thereby leading to enhanced momentum and heat transfer rates.

The equations of motion for constant-property, Newtonian fluid flow are governed by the equations of conservation of mass (i.e. the continuity equation):

$$\frac{\partial \tilde{U}_i}{\partial x_i} = 0, \tag{2.2}$$

and momentum (the Navier-Stokes equations):

$$\frac{\partial \tilde{U}_i}{\partial t} + \tilde{U}_j \frac{\partial \tilde{U}_i}{\partial x_j} = -\frac{1}{\rho}\frac{\partial \tilde{p}}{\partial x_i} + \nu \frac{\partial^2 \tilde{U}_i}{\partial x_j \partial x_j}, \tag{2.3}$$

where the Einstein summation notation is used, and where $\tilde{U}_i$ represents the instantaneous velocity in the Cartesian direction i. Due to the random nature of turbulent flows, it is typical for the Cartesian components of the instantaneous velocity ($\tilde{U}$, $\tilde{V}$, and $\tilde{W}$) to be decomposed into their respective mean and fluctuating components, e.g.:

$$\tilde{U}_i = \langle U_i \rangle + u_i, \tag{2.4}$$

where the angled brackets ($\langle U_i \rangle$) represent averaging, and lower-case letters represent the fluctuation from the mean (such that $\langle u_i \rangle = 0$). This decomposition is known the Reynolds decomposition (Tennekes & Lumley, 1972). By substituting Equation 2.4 into Equation 2.3 and subsequently averaging, the Reynolds-averaged Navier-Stokes (RANS) equations are obtained:

$$\frac{\partial \langle U_i \rangle}{\partial t} + \langle U_j \rangle \frac{\partial \langle U_i \rangle}{\partial x_j} = -\frac{1}{\rho}\frac{\partial \langle p \rangle}{\partial x_i} + \nu \frac{\partial^2 \langle U_i \rangle}{\partial x_j \partial x_j} - \frac{\partial \langle u_i u_j \rangle}{\partial x_j}, \tag{2.5}$$

where the last term in equation 2.5 contains a new term arising from the Reynolds decomposition, known as the Reynolds stress ($\langle u_i u_j \rangle$). The presence of this term adds additional unknowns to the RANS equations, leading to the famous closure problem of turbulence (Pope, 2000).

Since the study of turbulence relies so heavily on statistical analysis, it is convenient to define a "turbulent" Reynolds number that characterizes the turbulence (as opposed to the mean flow) using statistical quantities for the velocity and length scales:

$$Re_\ell \equiv \frac{u\ell}{\nu}. \tag{2.6}$$

Here, u is a velocity that is characteristic of the turbulent fluctuations (typically the root-mean-square velocity fluctuation), and ℓ is a length scale related to the largest eddies in the flow (typically called the integral length scale).

One method to estimate the scale of the largest eddies in the flow makes use of the

autocorrelation function to quantify the "memory" of the turbulent flow. The autocorrelation of the streamwise (i.e. longitudinal) velocity fluctuations is defined as:

$$\rho_u(\tau) = \frac{\langle u(t)u(t+\tau)\rangle}{\langle u^2\rangle}. \tag{2.7}$$

By integrating the autocorrelation function of the time series of the velocity fluctuations from $\tau = 0$ to the first zero crossing (τ_0), the integral time scale is obtained. Taylor's frozen-eddy hypothesis (Taylor, 1938) can then be used to find the integral length scale:

$$\ell = \langle U\rangle \int_0^{\tau_0} \rho_u(\tau) d\tau. \tag{2.8}$$

Furthermore, the characteristic turbulent velocity fluctuation (u or u_{rms}) is often scaled by the local mean velocity ($\langle U\rangle$) to form another non-dimensional quantity, the turbulent intensity (Ti):

$$Ti \equiv \frac{u_{rms}}{\langle U\rangle}, \tag{2.9}$$

which quantifies of the level turbulence in a flow.

After observing turbulent flows, Richardson (1922) suggested the existence of a hierarchy of turbulent eddies superimposed within a turbulent flow. Large-scale eddies were speculated to be unstable, breaking down into smaller-scale eddies until the size of the eddies were small enough to have their energy dissipated by the viscosity of the flow. This notion was referred to as the energy cascade (or the turbulent cascade). Large-scale eddies are typically quantified using the integral length scale (ℓ), but the size of small-scale eddies (where viscous effects start to become significant) was unknown.

It wasn't until the work of Kolmogorov (1941) that a major advance in the study of turbulence was made. In his seminal work, Kolmogorov postulated that in the limit of an infinite Reynolds number, there is a sufficient separation of scales in the turbulent flow such that small-scale motions become independent of large-scale ones. The implications of this theory would be remarkable, implying a universal characterization of the small-scale fluctuations for all turbulent flows, such that they become locally isotropic. The

two major hypotheses that resulted from Kolmogorov's 1941 work (herein referred to as K41) were that:

1. In any turbulent flow, the statistics of the small-scale motions should have a universal form uniquely determined by the rate of dissipation of turbulent kinetic energy (ϵ), and the viscosity (ν).

2. For length scales much smaller than the largest scales of the flow (ℓ), and much larger than the smallest scales (η), there exists an intermediate range of scales called the inertial subrange in which the statistics of the turbulent motion are uniquely determined by ϵ (and independent of ν).

In other words, a universal small-scale behaviour of turbulence should only be characterized by the dissipation rate and kinematic viscosity. The dissipation rate represents the rate at which turbulent kinetic energy is converted into internal energy, and is defined as follows:

$$\epsilon \equiv 2\nu \left\langle s_{ij} s_{ij} \right\rangle , \tag{2.10}$$

where s_{ij} is the fluctuating strain rate of the flow, such that $s_{ij} = \frac{1}{2}\left(\frac{\partial u_i}{\partial x_j} + \frac{\partial u_j}{\partial x_i}\right)$. Hinze (1959) demonstrated that in isotropic turbulence, ϵ can also be calculated using:

$$\epsilon = 15\nu \left\langle \left(\partial u_1/\partial x_1\right)^2 \right\rangle . \tag{2.11}$$

Using the dissipation rate, a length scale can be formed by a combination of ϵ and ν to quantify the size of the smallest eddies (η). This length scale is referred to as the Kolmogorov scale, and is defined as follows:

$$\eta \equiv \left(\frac{\nu^3}{\epsilon}\right)^{1/4} . \tag{2.12}$$

The Kolmogorov scale is typically the representative scale of the smallest eddies in the flow. The Taylor microscale (λ) is another scale often used, however, in the study of

turbulence (Tennekes & Lumley, 1972). It is defined by the following:

$$\left\langle \left(\frac{\partial u}{\partial x} \right)^2 \right\rangle \equiv \frac{\langle u^2 \rangle}{\lambda^2}. \tag{2.13}$$

The importance of the dissipation rate (ϵ) in the study of turbulence cannot be understated, as it is a quantity which relates the large-scale features of the flow (at which turbulent kinetic energy is injected) to the small-scale features of the flow (at which that energy is dissipated by viscosity).

Turbulent flows are equally capable of transporting scalar quantities such as heat. If the mean temperature gradient inside a turbulent flow is small enough that it does not induce significant changes in fluid properties (such as density, viscosity, etc.), then heat can be treated as a passive scalar that is advected and diffused by the flow. The governing advection-diffusion equation for a passive scalar with instantaneous concentration $\tilde{\Theta}$ (in this case temperature) is given by:

$$\frac{\partial \tilde{\Theta}}{\partial t} + \tilde{U}_i \frac{\partial \tilde{\Theta}}{\partial x_i} = \alpha \frac{\partial^2 \tilde{\Theta}}{\partial x_i \partial x_i}, \tag{2.14}$$

where α represents the thermal diffusivity of the fluid, which is assumed to be constant, and has the same dimensions as the kinematic viscosity, ν. The Prandtl number (Pr) is defined as the ratio ν/α. In air, the Prandtl number is typically 0.7, denoting that heat is diffused by molecular processes more readily than momentum.

Much like for velocity, the Reynolds decomposition can be applied to the advection-diffusion equation to obtain an evolution equation for the mean scalar concentration:

$$\frac{\partial \langle \Theta \rangle}{\partial t} + \langle U_i \rangle \frac{\partial \langle \Theta \rangle}{\partial x_i} = \alpha \frac{\partial^2 \langle \Theta \rangle}{\partial x_i \partial x_i} - \frac{\partial \langle u_i \theta \rangle}{\partial x_i}, \tag{2.15}$$

where $\langle u_i \theta \rangle$ is a new term, similar to the Reynolds stress in equation 2.5, often referred to as a turbulent heat flux. It is worth noting that this new heat flux term $\langle u_i \theta \rangle$ does not have dimensions of a true heat flux (which has units of $\frac{W}{m^2}$), and only does so when

multiplied by ρc_p.

While the ratio of advective to diffusive transport of momentum in a flow is characterized by the (turbulent) Reynolds number, the (turbulent) Péclet number is used to quantify the ratio of advective to diffusive transport of the scalar, and is defined as:

$$Pe \equiv \frac{u\ell_\theta}{\alpha}. \tag{2.16}$$

The similarities between equations (2.5) and (2.15) are striking, suggesting that turbulence should transport passive scalars (such as heat) much the same way as momentum. This realization brought forth the idea of the passive scalar cascade, which was proposed as an extension to the pioneering work of Kolmogorov by Oboukhov (1949) and Corrsin (1951). This extension is also known as KOC theory. Whereas K41 is posed in the limit of an infinite Reynolds number, KOC theory is posed in the limit of infinite Reynolds and Péclet numbers. Analogous to the first and second hypotheses of Kolmogorov theory, the fundamental hypotheses of KOC theory are that:

1. The statistics of the small-scale motions of scalar fluctuations should have a universal form uniquely determined by the dissipation rate of turbulent kinetic energy (ϵ), the dissipation rate of scalar variance (ϵ_θ), the viscosity (ν), and the thermal diffusivity (α).

2. For length scales much smaller than the largest scales of the flow (ℓ, ℓ_θ), and much larger than the smallest ones (η, η_θ), there should be an appropriate part of the scalar spectrum in which ν and α are unimportant.

Playing a similar role to the dissipation rate of TKE, the dissipation rate of (one half of the) scalar variance ($\frac{1}{2}\langle\theta^2\rangle$) is found to be:

$$\epsilon_\theta = 3\alpha \left\langle (\partial\theta/\partial x_1)^2 \right\rangle, \tag{2.17}$$

and the thermal integral length scale as:

$$\ell_\theta = \langle U \rangle \frac{\int_0^{\tau_0} R_\theta(\tau) d\tau}{\langle \theta^2 \rangle}. \tag{2.18}$$

The dissipation scale for the passive scalar (η_θ), is dependent on the Prandtl number. In the case of air, where $Pr < 1$, the dissipation length scale for the passive scalar is known as the Corrsin scale, and is given by:

$$\eta_\theta \equiv \left(\frac{\alpha^3}{\epsilon} \right)^{1/4} = \eta Pr^{-3/4}. \tag{2.19}$$

For further reading on K41 and KOC theory, interested readers are encouraged to refer to Tennekes and Lumley (1972) and Pope (2000).

2.2 Turbulent Boundary Layers

Many important turbulent flows, including those commonly observed in the atmosphere, are classified as wall-bounded shear flows. Such flows have additional complications, because the presence of the wall imposes constraints on the flow. Moreover, in the region nearest the wall, viscous effects cannot be neglected, no matter how large the Reynolds number (Tennekes & Lumley, 1972). The most simple expression of a wall-bounded shear flow is the case of fully developed channel flow, however, most atmospheric flows (including the atmospheric boundary layer) are considered boundary layer flows, since they evolve in the streamwise direction of the flow.

Consider a steady, incompressible flow with uniform velocity U_∞ over a smooth and flat surface. Due to the no-slip condition at the surface, a boundary layer with height δ will grow in the streamwise (x) direction. The mean velocity $\langle U \rangle$ will increase with distance from the wall, until it eventually reaches the value of the free-stream velocity U_∞. A common empirical method for finding the boundary layer height is by defining it as the height at which $\langle U \rangle / U_\infty$ is equivalent to some value close to 1, usually 0.99.

Determining the nature of the velocity profile within the boundary layer is of particular interest, and will be discussed in this section.

Assuming a steady-state, two-dimensional flow, the RANS equation for the streamwise direction is given by:

$$\langle U\rangle \frac{\partial \langle U\rangle}{\partial x} + \langle V\rangle \frac{\partial \langle U\rangle}{\partial y} = \frac{-1}{\rho}\frac{\partial \langle P\rangle}{\partial x} + \frac{\partial}{\partial y}\left(-\langle uv\rangle + \nu\frac{\partial \langle U\rangle}{\partial y}\right) + \frac{\partial}{\partial x}\left(-\left\langle u^2\right\rangle + \nu\frac{\partial \langle U\rangle}{\partial x}\right). \tag{2.20}$$

Additional assumptions can be made to further simplify this equation and gain insight about the nature of the velocity profiles. A boundary layer is characterized by the assumption that quantities change much faster in the wall normal direction (y) than they do in the streamwise direction (x) (in other words, $\frac{\partial}{\partial y} \gg \frac{\partial}{\partial x}$), such that the last term in equation (2.20) is negligible. It can be shown using scaling arguments for the flow outside the boundary layer that the two terms on the left hand side of equation (2.20) are small when compared to the stress terms, and are of similar order, such that they can be reasonably neglected. Further assuming that there is no mean pressure gradient, or that the mean pressure gradient is negligible, equation (2.20) reduces to:

$$0 = \frac{d}{dy}\left(-\langle uv\rangle + \nu\frac{d\langle U\rangle}{dy}\right), \tag{2.21}$$

which is the governing equation of motion for a turbulent boundary layer given the assumptions listed above.

Consider an outer region of the boundary layer, where viscous effects are negligible. Here, it is expected that the governing equation of motion will have a solution that satisfies a velocity defect law when y/δ>0.1 (Tennekes & Lumley, 1972):

$$\langle U\rangle - U_\infty = u_* F\left(\frac{y}{\delta}\right), \tag{2.22}$$

where F is some non-dimensional scaling function for the velocity defect, and u_* is a flow-dependent constant called the friction velocity, related to the wall shear stress. The

shear stress at the wall (τ_w) is:

$$\tau_w = \mu \frac{d\langle U \rangle}{dy}|_{y=0}, \tag{2.23}$$

and can be related to the friction velocity by:

$$\tau_w = \rho u_*^2. \tag{2.24}$$

While the wall shear stress in a turbulent boundary layer is not constant in the x direction, it is assumed that the wall shear stress is significantly smaller than the free-stream dynamic pressure outside of the boundary layer (ρU_∞^2). It can then be considered effectively constant in the context of the boundary layer, thus keeping the friction velocity u_* as a constant (Tennekes & Lumley, 1972).

However, the velocity defect law is not expected to hold in the region closer to the wall, where viscous effects are no longer negligible (but not completely dominant). In this region, referred to as the inertial sublayer, the solution to equation 2.21 is the well-known law of the wall, which is derived in detail in the literature (Pope, 2000; Tennekes & Lumley, 1972). The law of the wall for the inertial sublayer of the boundary layer yields a logarithmic velocity profile:

$$\frac{\langle U \rangle}{u_*} = \frac{1}{\kappa}\left(\ln\left(\frac{y u_*}{\nu}\right) + B\right), \tag{2.25}$$

where κ is the von Kármán constant (taken to be approximately 0.41), and B is an integration constant equal to 5.2 (Pope, 2000).

Since the inertial sublayer and outer region of the turbulent boundary layer eventually meet, equations (2.22) and (2.25) must match up for some value of y. If this is the case, then $F\left(\frac{y}{\delta}\right)$ must also be logarithmic in nature. Combining these two equations yields the logarithmic friction law for a turbulent boundary layer, where it can be shown that:

$$\frac{U_\infty}{u_*} = \frac{1}{\kappa}\ln\left(\frac{\delta u_*}{\nu}\right) + A, \tag{2.26}$$

where A is some flow-dependent constant (Tennekes & Lumley, 1972).

As in the previous section, the analytical results for the velocity profile in a turbulent boundary layer can be extended to the concentration of a passive scalar $\tilde{\Theta}$, governed by the Reynolds-averaged advection-diffusion equation (equation (2.15)). An analogous friction scalar concentration, θ_* is defined as:

$$\theta_* = \frac{\alpha}{u_*} \frac{d \langle \Theta \rangle}{dy}|_{y=0}. \tag{2.27}$$

A similar result to equation (2.26) can then be obtained for the passive scalar (Kader, 1981), whereby:

$$\frac{\langle \Theta \rangle - \Theta_\infty}{\theta_*} = \frac{1}{\alpha} \ln \left(\frac{\delta_\theta u_*}{\nu} \right) + C. \tag{2.28}$$

Here, the thermal boundary layer height δ_θ takes the place of the aerodynamic boundary layer δ.

2.2.1 Roughness Effects

The theoretical results for the logarithmic velocity profile are valid for an aerodynamically smooth surface. However, most real-world atmospheric flows take place over a wall which has some level of surface roughness. For a surface with an RMS (root-mean-square) roughness k, the effect of the roughness on the flow will be negligible so long as k is small. It is useful to define a parameter to quantify the size of k relative to the viscous scales of the wall. To accomplish this, a "roughness" Reynolds number is defined as:

$$R_k = \frac{k u_*}{\nu}. \tag{2.29}$$

For small values of R_k (i.e. $R_k < 30$), surface roughness will have no effect on the shape of the logarithmic velocity profile, and instead only modify the additive constant B in equation (2.25). For very small values of R_k (i.e. $R_k < 5$), the law of the wall remains unchanged (since the roughness elements are submerged in a viscous sublayer in which

no Reynolds stresses are generated), and the surface may be considered aerodynamically smooth. For larger values of R_k, the scaling of the rough-wall velocity profile becomes:

$$\frac{\langle U \rangle}{u_*} = \frac{1}{\kappa} ln \left(\frac{y}{k} \right) + B. \tag{2.30}$$

2.3 Stratified Turbulent Flows

The above findings for turbulent boundary layer flow over a flat wall assume that the fluid is neutrally buoyant. However, if large temperature gradients exist such that the effects of changes in density of the fluid are non-negligible, the effects of thermal stratification will influence the nature of the turbulence. Consider the case of stable stratification, where the density decreases (and temperature increases) in the direction opposite to the gravitational vector, which is common for atmospheric flows.

In stratified flows, the density is no longer constant and the incompressible fluid assumption used in classical boundary layer theory (e.g. the law of the wall) is invalid. To simplify these types of flows, the Boussinesq approximation is often used. It states that changes in fluid density are usually small, and can be neglected unless they are multiplied by the acceleration due to gravity (g) in the governing equation of motion. These changes in fluid density are said to be linearly related to the change in fluid temperature relative to an adiabatic reference point (Tennekes & Lumley, 1972).

Using the Boussinesq approximation, Monin and Obukhov (1954) developed a similarity theory for stratified, statistically-stationary, horizontally-homogeneous flows in the absence of a mean pressure gradient. They argued that there are universal relationships between non-dimensional quantities in the surface layer above a wall-bounded turbulent flow. Similar to the preceding section, a length scale is introduced for the wall-normal direction. This scale is referred to as the Monin-Obukhov length scale, and is given by:

$$L \equiv \frac{1}{\kappa} \frac{u_*^2}{g \alpha \theta_*}. \tag{2.31}$$

In the context of stratified flows, the region in which the quantity y/L (i.e. the Monin-Obukhov stability parameter) is less than unity is referred to as the surface layer. In this region, turbulent fluxes of momentum ($\langle uv \rangle$) and heat ($\langle v\theta \rangle$) are presumed constant. Given that the friction velocity will always be a positive value, the sign of θ_* will dictate the sign of the Monin-Obukhov length scale, wherein $L > 0$ for stable stratification, and $L < 0$ for unstable stratification. One of the key results of Monin-Obkuhov theory is that logarithmic profiles of mean quantities can be recovered, similar to the non-stratified case.

In a stratified turbulent flow, the vertical temperature gradient $\beta = \frac{\partial \Theta}{\partial y}$ will induce a fluctuating body force that performs work. This is referred to buoyant production, and will tend to enhance or suppress turbulent mixing depending on the nature of the temperature gradient. For a stably stratified flow, where β is positive, the buoyant production will act counter to the turbulent production of kinetic energy, suppressing turbulent mixing. Beyond a certain point, the effects of stratification will completely suppress the turbulence, generating internal gravity waves (Tennekes & Lumley, 1972). The level of stratification present in a flow is usually quantified through a Richardson number, which has many different formulations (as will be discussed below). Fundamentally, it is a non-dimensional number relating the magnitude of the buoyancy gradient to that of the shear generated by the flow. Larger (positive) Richardson numbers imply stronger stability (i.e. higher levels of stratification), while the importance of the shear-generated turbulence is stronger as the Richardson number tends to zero.

Due to its impact on turbulent mixing, the effects of stratification on turbulence have been widely investigated. Beyond the important work of Monin and Obukhov, accurate modelling and description of a stably stratified turbulent boundary layer is a difficult task to accomplish (Stull, 1988). Therefore, experimental and computational studies are often performed. Some of the relevant work in this area is reviewed here.

Arya (1975) performed one of the first studies on the effects of stratification over a flat-plate boundary layer, simultaneously measuring two velocity components (longitudinal and transverse) and temperature. They reported that turbulent quantities (such as

intensities, fluxes, and correlation coefficients) were sensitive to buoyancy effects, noting the suppression of turbulence in stronger stable stratification. However, they observed that the nature of the spectra of velocity and temperature fluctuations did not exhibit a so-called buoyant subrange, wherein mechanical production is expected to be less significant than the energy extracted by overcoming the mean buoyancy gradient.

Yoon and Warhaft (1990) performed wind-tunnel experiments to investigate the downstream evolution of grid-generated turbulence under stable stratification. Although these experiments were performed in the absence of mean shear, they found a similar destruction of the turbulent fluxes with increasing Richardson number, and also observed counter-gradient fluxes under very high levels of stratification. Furthermore, they observed increased dissipation rates of scalar variance with increasing stratification. They defined a turbulent Richardson number as:

$$Ri_t \equiv \frac{g\beta}{\Theta_\infty}\left(\frac{\ell}{v_{rms}}\right)^2, \tag{2.32}$$

to quantify the level of stratification.

Piccirillo and van Atta (1997) performed a similar study on the downstream evolution of grid-generated turbulence under stable stratification, this time in a uniformly sheared flow. They found that the critical Richardson number to distinguish between weak and strong stable stratification correlated well with the level of shear in the flow, whereby increased shear levels corresponded to a larger critical Richardson number. Furthermore, they found that stably stratified turbulent flows were highly anisotropic at all scales, persisting down to the smallest scales of the turbulent cascade. They found that additional anisotropy was induced by the shear when compared to free-shear stratified flows, and observed an increase in large-scale anisotropy with increasing downstream distance (i.e. decreasing turbulent kinetic energy).

Ohya, Neff, and Meroney (1997) performed a wind tunnel investigation of the structure of turbulence in a stably stratified boundary layer for a wide range of bulk Richardson

numbers (ranging from 0.12 to 1.33), which were calculated as follows:

$$Ri_\delta = \frac{g\delta}{\Theta_\infty}\frac{\Theta_\infty - \Theta_s}{U_\infty^2}, \tag{2.33}$$

where Θ_∞ and Θ_s represent the free-stream and surface temperatures, respectively. They found that the magnitudes of turbulent intensities and fluxes of both momentum and heat were greatly reduced by the effects of stable stratification, and that the level of suppression correlated well with the bulk Richardson number. Furthermore, they found significant differences between weakly stable flows ($0 < Ri_\delta < 0.25$) and strongly stable flows ($Ri_\delta > 0.25$), where 0.25 is the critical Richardson number found by a linearized theory for inviscid flow (Ohya et al., 1997). Under very stable stratification, turbulent fluxes tended to vanish, or even occurred against the buoyancy gradient.

Ohya (2001) then extended this work to investigate the effects of roughness on the profiles of turbulent fluxes in a stable boundary layer. They found that the presence of roughness elements tended to significantly increase turbulent fluxes for weakly stable cases when compared to the smooth wall experiments. However, for strongly stable flows, turbulent fluxes tended to vanish and were replaced by wave-like motions cause by Kelvin-Helmholtz instabilities.

More recently, Williams, Hohman, Van Buren, Bou-Zeid, and Smits (2017) investigated the effects of stable stratification on turbulent boundary layer statistics, attempting to consider the effects of both the Reynolds number as well as the Richardson number. In their work, the gradient Richardson number was argued to be a superior parameter for measuring stratification and differentiating between weak and strong stability cases. It was calculated as:

$$Ri_g = \frac{g}{\Theta_\infty}\frac{\partial\Theta/\partial y}{(\partial U/\partial y)^2}. \tag{2.34}$$

They found that for weak to moderately stable flows, turbulent fluxes scaled with the wall shear stress. They suggested that this scaling was useful for differentiating between Reynolds and Richardson number effects. However, for higher levels of stratification, this

shear stress scaling ceased to hold. Furthermore, they found that turbulence was preferentially damped in the outer region of the flow, maintaining its intensity near the wall even for the case of strongly stable stratification. A consequence was that characteristics such the large-scale anisotropy were unaffected by the effects of stable stratification up until a critical point. They argued that there was no change in the structure of turbulence under weak stratification, but under strong stratification (beyond the critical Richardson number) there was a "marked change in the flow response."

2.4 Atmospheric Turbulence over Glaciers

The previous sections provided an overview of turbulent flows over a smooth, rigid wall in the presence of stable stratification. To a certain extent, such flows can be representative of the flow in the atmospehric boundary layer over glaciers. However, further elements, such as topography, surface albedo/snow coverage, and other wind elements add further complexity.

An important distinction between real-world glacier flows, and the previously discussed stably stratified boundary layer flows, was investigated by Denby and Smeets (2000), who noted that the atmospheric boundary layer flow over glaciers is dominated by katabatic (downslope) winds. They subsequently derived a momentum budget used for modelling for katabatic glacier flows. Such flows typically originate from high-elevation air which cools enough to increase its density and travel downstream at high speeds. Simulated profiles of different quantities in a katabatic boundary layer were presented by Denby and Greuell (2000), using their derived energy and momentum budgets.

An investigation of the katabatic flow over glaciers was performed by Oerlemans and Grisogono (2002), who found that the katabatic layer (close to the surface) is characterized by a local wind speed maximum, typically within 10 m of the surface. The local wind speed maximum acts as a turbulent jet nested inside the atmospheric boundary layer, providing wind speeds on the order of 6 m/s for small-to-medium glaciers. The height and magnitude of the wind speed maximum served as characteristic length and

velocity scales for the katabatic flow. Using their values of wind speed and temperature, bulk Richardson numbers of approximately 0.04 were observed at the height of the wind speed maximum. Despite intense thermal gradients (up to 10 K/m) which act to stabilize the flow according to Monin-Obukhov theory, high levels of turbulence were observed in the katabatic boundary layer. These high levels of turbulence were found to dominate the exchange of energy and heat near the surface, easily overcoming the suppression from stratification. Profiles of wind speed and temperature near the surface show a non-linear velocity profile and a linear temperature profile in the region between the surface and wind speed maximum. They explain that the temperature profiles are adequately modelled using the large-scale atmospheric boundary layer (since no temperature differential maximum occurs in the katabatic layer), but that velocity profiles require small-scale resolution on the order of the height of the wind speed maximum. Given their findings, a representative model of the katabatic boundary layer over a glacier (such as in a wind tunnel experiment) may be obtained using a highly turbulent background flow in the presence of a linear thermal gradient.

Litt, Sicart, Helgason, and Wagnon (2015) also studied the turbulence characteristics above a melting glacier using sonic anemometers and profile mast measurements within 6 m above the surface. They found that for low-speed wind conditions, the local wind speed maximum was approximately 2 m above the surface. However, for high-speed wind conditions, no wind speed maximum was observed. This would imply that the height of the local wind speed maximum was likely above the 6 m observational envelope of their study, and that its position scales with wind speed. They also reported exceptionally high turbulent intensities (as high as 50% in some cases). For katabatic flows, they observed the typical turbulent intensity to be 32 $\pm$ 12%, while the bulk Richardson number was around 0.09. In another related study, Litt, Sicart, Six, Wagnon, and Helgason (2017) observed turbulent intensities to be around 10-15%, although sometimes reaching as high as 50%. The high turbulent intensities again highlight the dominance of the velocity field over the effects of stable stratification when considering heat transfer near the surface.

Mott, Paterna, Horender, Crivelli, and Lehning (2016) performed a series of wind tunnel experiments to investigate the effects of cold-air pooling observed above melting snow. Topographical depressions can result in detachment of the boundary layer inside the depression, such that a volume of cold-air will fill the space and prevent turbulent mixing of heat at the surface. In their experiments, Mott et al. (2016) found that the effects of local topography features are significant for low to moderate wind speeds, where heat transfer at the snow surface was strongly suppressed. However, at higher wind speeds (in this case, approximately 3 m/s), the difference between a flat and concave snow surface on the magnitude of turbulent fluxes was negligible. Furthermore, they found that for bulk Richardson numbers near 0.25, the region above a flat snow patch in which turbulent mixing was suppressed was very shallow, perhaps suggesting that stratification effects may only be significant for a small region of the boundary layer, and only at lower Reynolds numbers.

Stiperski, Holtslag, Lehner, Hoch, and Whiteman (2020) studied the turbulence of deeper katabatic flows, where the height of the wind speed maximum was between 20-50 m above the surface. They found that the structure of deep katabatic flows was similar to that of shallow katabatic flows in the area below the wind speed maximum. Although this study was not performed for a glacier flow, the structure of the flow (stably stratified katabatic flow) was found to be similar to that of typical glacier flows mentioned above.

Nicholson and Stiperski (2020) compared the structures of turbulence over exposed and debris-covered glacier ice, finding strong similarity of the turbulent quantities for both surface types. Furthermore, they found that although there was strong aerodynamic similarity between the two cases, vertical temperature profiles were different. Debris covering the surface of glacier ice will influence the thermal and radiative properties of the surface, thereby influencing the temperature field.

In summary, the atmospheric flow over glaciers is typically defined by strong katabatic forcing near the surface, providing an internal boundary layer (usually less than 10 m thick) that is nested within the larger atmospheric boundary layer (which is usually on the

order of 100 m thick). This internal boundary layer, combined with effects of topography, surface debris cover, etc. invalidates the similarity assumptions of Monin-Obukhov theory which is typically used for modelling atmospheric glacier flow.

2.5 Estimation of Sensible Turbulent Heat Fluxes

Sensible heat fluxes, which represent an important contribution to the surface energy balance for a melting glacier, are difficult to model given the complexity of typical glacier flows as described in the preceding sections. As such, there have been numerous studies devoted to their measurement, estimation, and modelling. The following subsections will summarize the three primary methods for calculating sensible heat fluxes, as well as some of the investigations which have been done to parameterize them.

2.5.1 Eddy Covariance Method

Using sonic anemometers, the eddy covariance method (or eddy correlation method) has been deemed the most accurate method to directly measure turbulent heat fluxes over glaciers (Hock, 2005). However, given the high operational requirements for implementation of this method, studies using eddy covariance methods are rare and highly localized. The accuracy of eddy covariance comes at the cost of instrumental robustness, therefore making it largely impractical. Sonic anemometers used to measure three-component velocity over glaciers are typically expensive, highly sensitive, and difficult to maintain in harsh environments (Chambers et al., 2020). In the eddy covariance method, the sensible turbulent heat flux is calculated as:

$$Q_H \equiv \rho c_p \langle v\theta \rangle . \tag{2.35}$$

When eddy covariance measurements are performed, they are typically used for validating or improving other methods for estimating heat fluxes (such as the profile or bulk methods). Munro (1989) performed one of the first studies in which the turbulent

heat fluxes were directly measured over a glacier surface. They subsequently used the results to estimate parameters used in the bulk method. Denby and Greuell (2000) also performed a similar study for katabatic glacier flow.

Suter et al. (2004) investigated both the radiation and turbulent heat flux components of the surface energy balance, using the eddy correlation results to evaluate the profile and bulk methods for estimating sensible heat fluxes. Fitzpatrick et al. (2017) then attempted to directly measure all heat fluxes above a glacier, hoping to validate the models which are used to close the surface energy balance, including the turbulent fluxes. The results of the direct measurements were then used to evaluate different bulk method parameterizations. Radić et al. (2017) also used sonic anemometer measurements to evaluate the use of Monin-Obukhov similarity theory with the bulk method.

2.5.2 Profile Method

The profile method was derived as a way to estimate the sensible heat fluxes due to the difficulty involved with their direct measurement using the eddy covariance approach. Based on the work of Prandtl (1935), the flux of (momentum or) a passive scalar in a wall-bounded flow can be estimated using the mean gradient and an "eddy diffusivity", such that the turbulent heat flux is estimated as:

$$Q_H = \rho C_p K_H \frac{\partial \langle \Theta \rangle}{\partial y}, \tag{2.36}$$

where K_H is the eddy diffusivity, which is a function of wind speed, surface roughness, and atmospheric stability (Hock, 2005). This approach was first applied to snow and ice by Sverdrup (1935). In practice, measurements of wind speed and temperature are taken at two different points, and the Monin-Obukhov logarithmic profile is assumed in order to interpolate the local wind speed and temperature profiles in the surface layer above a glacier. However, due to the aforementioned presence of a local wind speed maximum caused by katabatic forcing in the first few metres above the surface (Oerlemans & Grisogono, 2002), the similarity laws of Monin-Obukhov theory are invalid. Furthermore,

Monin-Obukhov theory assumes a constant-flux layer near the surface, however, in reality, the thickness of this region is too small to make accurate field measurements (Denby & Greuell, 2000). For these reasons, the profile method is only valid for near-neutral conditions (in which Prandtl's gradient transport theory was derived), in the absence of katabatic forcing (Chambers et al., 2020). A further challenge associated with the profile method is its large sensitivity to measurement errors, which decreases with the number of measurement heights. The practicality of installing and maintaining a tower with several measurement points makes these studies rare (Hock, 2005).

Despite these challenges and shortcomings, some studies have investigated the applicability of the profile method for estimating sensible heat fluxes. Denby and Greuell (2000) also found that the profile method tends to severely underestimate the turbulent heat fluxes in the presence of a wind-speed maximum. Suter et al. (2004) found that use of the profile method was difficult to use due to measurement and instrumental error.

While the difficulties associated with the profile method inhibit its use in surface heat flux estimations, its assumptions used have been extended to develop a more practical and commonly used approach, known as the bulk method.

2.5.3 Bulk Method

The bulk method is the most commonly used method for estimating sensible turbulent heat fluxes, since it requires the least sophisticated equipment, and is easy to set-up and maintain in real glacier environments. Measurements of velocity and temperature are recorded at only one level above the surface and can be easily made through standard commercially available automated weather stations, leading to its widespread adoption. The bulk method is built upon the same underlying theory as the profile method, with the additional assumptions that the surface temperature is 0°C, and that there are other (often empiral) methods to determine the friction velocity (u_*) and temperature scale (θ_*) (Denby & Greuell, 2000). Despite several challenges associated with the bulk method, it is still the method of choice for estimating sensible turbulent heat fluxes in most studies

that are concerned with the surface energy balance for a glacier. Using the bulk method, the sensible heat flux is estimated as:

$$Q_H = \rho C_p C_H \langle U \rangle (\langle \Theta \rangle - \Theta_s), \tag{2.37}$$

where C_H is the so-called bulk exchange coefficient, obtained from the Monin-Obukhov profile equations. Since the bulk method is derived from the profile method, it is also technically only valid for near-neutral stability conditions. The bulk exchange coefficient, (C_H) depends upon on the measurement height, Monin-Obukhov stability parameter (y/L), and an aerodynamic roughness length (y_0), defined as the height above the surface where the mean velocity is equal to zero (Fitzpatrick et al., 2017). This latter parameter is very difficult to measure directly (Hock, 2005), such that correctly estimating the roughness length is the focus of many studies (Chambers et al., 2020). Furthermore, attempts to measure the roughness length by use of aerodynamic profiles are subject to high levels of uncertainty (Sicart, Litt, Helgason, Tahar, & Chaperon, 2014).

Another challenge arises in the calculation of the Monin-Obukhov length scale (L), which is dependent on the turbulent heat flux term, $\langle v\theta \rangle$. To calculate it requires an iterative approach to determine the heat flux, used to find L, which is then used to calculate the bulk exchange coefficient (C_H) and subsequently the turbulent heat flux. In some studies, the bulk exchange coefficient is related to the bulk Richardson number instead of the Monin-Obukhov stability parameter (Webb, 1970), and is calculated as:

$$C_H = \frac{\kappa^2}{\ln(y/y_0) ln(y/y_{0_\theta})} (1 - 5.2 Ri_b)^2, \tag{2.38}$$

where y_0 is the aerodynamic roughness length, and y_{0_θ} is the roughness length for temperature (which, unlike y_0, lacks a clear physical definition, but serves as an analogy for the temperature field nonetheless). For most glacier studies, since measurements of the velocity and temperature at the height of the wind-speed maximum (i.e. boundary layer height, δ) are not possible, the bulk Richardson number (Ri_b) will be calculated using

the local velocity and temperature at the measurement height y, such that:

$$Ri_b = \frac{gy}{\langle T \rangle} \frac{\langle T \rangle - T_s}{\langle U \rangle^2}. \tag{2.39}$$

Due to the large uncertainty involved with estimation of roughness lengths, some studies avoid the stability correction altogether when using the bulk approach, citing larger errors arising from the estimation of roughness lengths than the omission of the stability parameter (Braithwaite, 1995).

Denby and Greuell (2000) found that when comparing the bulk method to direct eddy covariance measurements, the bulk method still managed to produce reasonable estimations of the sensible heat flux (to within approximately 25%), despite a key component of Monin-Obukhov theory being invalidated for katabatic flows. In this study, the bulk method had a tendency to over-estimate the sensible turbulent heat fluxes. They also noted that the assumption that the surface temperature assumption ($\Theta_s = 0$) was reasonable for a melting ice surface, but that for an ice surface that isn't currently melting ($\Theta_s < 0$), the error from this assumption would be much higher.

Fitzpatrick et al. (2017) used eddy correlation measurements to evaluate three different methods for estimating the bulk exchange coefficient (C_H). One method used the bulk Richardson number (equation 2.38). Another neglected the effects of stratification, assuming a logarithmic profile with neutral stability, to estimate the bulk exchange coefficient as (Conway & Cullen, 2013):

$$C_H = \frac{\kappa^2}{\ln\left(\frac{y}{y_0}\right) ln\left(\frac{y}{y_{0_\theta}}\right)}. \tag{2.40}$$

The final method used the Monin-Obukhov stability parameter (y/L) as a scaling coefficient to correct for the effects of stratification. Of the three methods for estimating C_H, they found that the final method (which included the Monin-Obukhov stability parameter) offered the best results. However, this model was inaccurate in the presence of a low-level wind speed maximum which invalidated the Monin-Obukhov assumptions.

Radić et al. (2017) evaluated several different bulk parameterizations against direct eddy covariance measurement of the turbulent fluxes, and came to two important conclusions:

1. Regardless of the inclusion of the stability parameter in the estimation of sensible heat fluxes, the bulk method tends to overestimate the turbulent heat fluxes when compared to direct eddy-covariance measurements, especially during katabatic flow conditions, agreeing with the findings of Denby and Greuell (2000).

2. The uncertainty involved with estimating the roughness lengths (y_0 and y_{0_θ}) did not account for the difference between the measured and modelled heat fluxes. This suggests that improvements to predictions of turbulent heat fluxes using the bulk method must be developed by improving the model itself, as opposed to improving the quality of roughness length estimations.

The second point is especially pertinent as the ability to estimate roughness lengths improves with time, such as through the use of remote sensing applications (Chambers et al., 2020). It would appear that the accuracy of the bulk method in its current form will reach an asymptote in the coming years. Understanding the value of the simplicity of the bulk model for making turbulent heat flux predictions over glaciers, and that continued efforts to fine-tune its specific parameters (such as the roughness lengths) have not led to any general improvements in its performance, the bulk method appears to be in need of modification. In this sense, a modified form of the bulk method that makes use of the same single-height measurements of velocity and temperature without being constrained to the demanding assumptions of Monin-Obukhov similarity theory would deliver great value to those attempting to predict glacier melt through energy balance modelling.

Chapter 3:

Experimental Apparatus, Instrumentation, and Procedures

3.1 Experimental Design

In the present work, a series of wind tunnel experiments were performed to meet the objectives of this research as described in section 1.2. The design of these experiments, as they pertain to these specific objectives, is described below.

The first objective was to produce a series of turbulent flows that were representative of those typically seen over glaciers. It was shown in section 2.4 that glacier flows are characterized by high turbulent intensities (usually between 10-30%), bulk Richardson numbers on the order of 0.04 to 0.09, and a katabatic velocity profile which exhibits a distinct peak in the first few metres above the surface. Since it was found that the region below the wind speed maximum was the only region of relevance for characterizing the surface heat transfer, the region above the wind speed maximum can be reasonably neglected. This region below the wind speed maximum can then be adequately replicated by the typical turbulent boundary layer found in a laboratory-scale wind tunnel. To attain similar turbulent intensities to those of real-world flows, an active grid was used to generate homogeneous isotropic turbulence inside the wind tunnel.

The second objective was to develop and build a test section containing an extended ice patch that could serve as a model of a glacier. A novel glacier model was constructed from a large ice tray with an insulated bottom, which sat in line with the floor of the wind tunnel. The ice was kept as smooth as possible to minimize aerodynamic roughness effects, which could not otherwise be parameterized within the scope of the present work. A corresponding test section was then built to house the glacier model.

Having met the first two objectives, the third objective of the present work was to per-

form direct measurements of sensible turbulent heat fluxes over melting ice in a controlled laboratory setting. This required simultaneous measurement of two components of velocity and temperature over melting ice. The two-component velocity measurements were made using hot-wire anemometry, whereas the temperature measurements were made using cold-wire thermometry.

In the experiments performed in this work, three free-stream velocities (approximately 1.1, 2.0, and 3.2 m/s) and three measurement heights (corresponding to y/δ of 0.13, 0.33, and 0.53) were chosen such that there were nine different cases in the test envelope. These free-stream velocities were chosen to maximize the stratification as quantified using the Richardson number, while also being representative of the speeds typically observed in glacier flows (Mott et al., 2016). In this case, 1.1 m/s was the slowest speed attainable in the wind tunnel, corresponding to a bulk Richardson number (Ri_δ) of 0.04. The heights were selected to cover a range of y/δ in the region below the wind speed maximum, but still above the "constant-flux" surface layer. The intention was for these non-dimensional heights to be reasonably attainable by those performing field observations in the atmospheric boundary layer over a glacier using commercially available weather stations. For example, given a wind speed maximum height of 5 m over a glacier, $y/\delta = 0.33$ corresponds to a height of 1.65 m, within the reach of an average person.

This chapter describes the experimental apparatus, instrumentation, and procedures used in the present work to satisfy the first three objectives as explained above. The remaining four objectives are addressed in Chapter 4, which discusses the results obtained during the experiments.

3.2 Wind Tunnel

The experiments in this work were performed in an open-circuit wind tunnel in the Aerodynamics Laboratory at McGill University. A summary of the wind tunnel and its components is provided herein, however it is described in further detail in Cohen (2019). A schematic of the wind tunnel is presented in Figure 3.1. The air flow was generated by

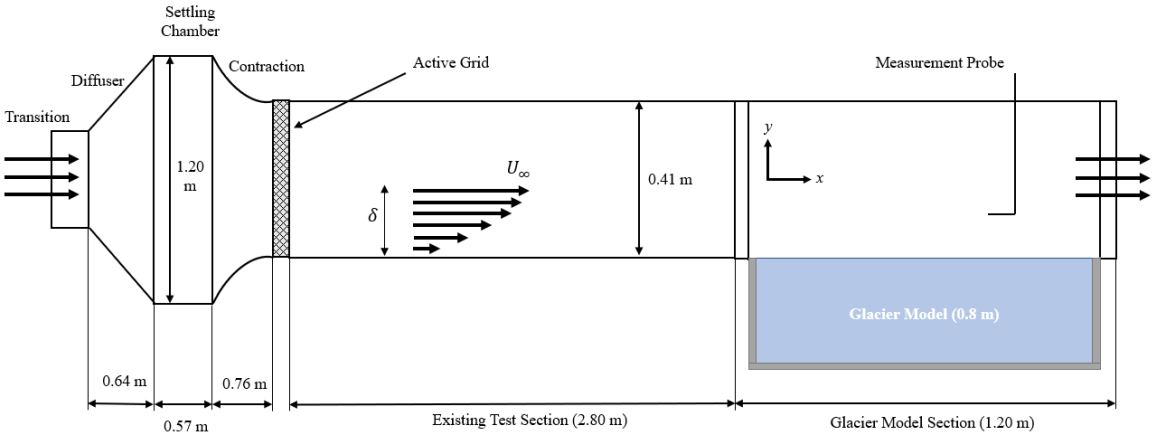

Figure 3.1: Schematic of wind tunnel (not to scale).

a Cincinnati HDBI-240 blower equipped with a 10 horsepower AC motor placed at the tunnel's inlet, which was controlled by a variable frequency ABB ACH550-UH controller. A transitional section was used to connect the blower outlet to a flow conditioning section, the outlet of which was connected to the inlet of the test section.

The purpose of the flow conditioning section was to ensure that the flow entering the test section was uniform, with little background turbulence. It was composed of a diffuser, settling chamber, and contraction (providing a 9:1 reduction in the cross-sectional area), and totalled approximately 2 m in length. Within the settling chamber, a series of screens were placed to break up large eddies (Mehta & Bradshaw, 1979).

The test section was approximately 2.8 m long, with a cross-sectional area of 0.407 m x 0.407 m, and had a slightly diverging ceiling to offset boundary layer growth on the tunnel walls, thereby maintaining a constant centreline velocity. Finally, the test section was followed by the glacier model section, which is described in detail in Section 3.2.2, and in which the experiments in this work were performed.

3.2.1 Active Grid

The use of a grid has historically been the standard method for generating homogeneous isotropic turbulence in wind tunnel experiments (Comte-Bellot & Corrsin, 1966). However, the use of typical (passive) grids generally yields low turbulent intensities (on the

Figure 3.2: Close-up of active grid.

order of 1-5%). There exist other methods for generating highly turbulent flows, such as random jet arrays (Pérez-Alvarado, Mydlarski, & Gaskin, 2016), however, to best emulate highly turbulent atmospheric glacier flow – which has turbulent intensities on the order of 10% (Litt et al., 2015) – in a laboratory wind tunnel, an "active" grid (Makita & Sassa, 1991) was used herein.

The active grid used for this work consisted of a 7x7 grid of rotating aluminum bars that were 6.4 mm in diameter. The mesh spacing, M, was 50.8 mm, or $\frac{1}{8}$ of the tunnel width (Mydlarski & Warhaft, 1996). Attached to the rotating bars were 0.38 mm thick, square aluminum wings. Static triangular wings of the same thickness were attached to the frame of the grid. The wings had holes drilled through them to reduce the downstream velocity deficit and improve the overall homogeneity of the flow. The square wings on the rotating bars were covered with tape, making them effectively solid and impenetrable, while the triangular wings on the grid frame were left uncovered. A photograph of the active grid is shown in Figure 3.2.

The rotating bars were each driven by a Superior Electric Slo-Syn 5W stepper motor with 200 steps per revolution. The stepper motors were connected to a controller made of a combination of Arduino and Elegoo microcontrollers, which controlled the rotating bars in one of several different modes (Cohen, 2019). The modes allowed the user to control the rotation speed of the bar, and the time interval before a bar would change direction.

The preferred method for generating homogeneous isotropic turbulence is the so-called double-random asynchronous mode (Mydlarski, 2017), in which both the rotation rate and time interval between changes in rotation directions for each bar are independently randomized. The double-random asynchronous mode was the one used for all experiments in this work. In this mode, the range of rotation speeds and time intervals were between 6.3 and 15.7 rad/s and 0.1 and 1.5 s, respectively.

3.2.2 Glacier Model

To represent a melting glacier inside the wind tunnel, an ice patch was constructed to sit flush with the tunnel floor. The glacier model was formed inside of a fibreglass tray with an inner length of 78 cm, width of 36 cm, and depth of 20 cm. This specific tray was selected since its outer width matched the inside width of the test section (40.7 cm), while also maximizing the length of the ice patch. Halfway along the length of the glacier model, a type E thermocouple wire was embedded along the outer edge approximately 5 mm below the surface to estimate the surface temperature. The thermocouple was embedded below the surface since the temperature measurements obtained by placing it directly on the ice surface would be contaminated by the air passing over top. The glacier model was designed and constructed to meet a series of practical constraints associated with its use inside of a laboratory-scale wind tunnel, which are discussed below.

Weight Considerations

Since the tray was so deep, filling its entire volume with water (which would later be frozen into ice) made it far too heavy to be safely manipulated by one person. To reduce the overall weight of the glacier model, the volume was effectively halved by filling the bottom half of the tray was with two layers of 5.1 cm thick styrofoam. Besides reducing the overall weight, this also served to provide insulation, restricting most of the ice melting to the surface. The insulated portion was partitioned from the water basin by placing a thin (0.5 mm thick) aluminum sheet on top of the styrofoam, and then sealing the edges

using a marine-grade sealant. The upper portion of the tray was then filled with water and frozen solid. The result was an ice block that was approximately 78 cm long, 36 cm wide, and 10 cm deep.

Surface Roughness

Although glacier ice is typically characterized by surface roughness (Hock, 2005), the existence of roughness elements in a turbulent boundary layer can change the nature of the turbulence (Tennekes & Lumley, 1972), and even slight changes in the initial conditions (such as the presence of roughness elements at the leading edge of the ice patch) can lead to differences in the nature of the temperature fluctuations (Beaulac & Mydlarski, 2004a, 2004b). Since there was no satisfactorily rigorous way to control the roughness within the scope of this work, the decision was made to limit the present investigations to turbulent heat fluxes over a smooth ice surface for the experiments of the present work, which represent an initial attempt to replicate glacial ice in a laboratory-scale wind tunnel.

During the freezing process, the water inside the tray would freeze from the top to bottom. This is mainly because of the lower density of ice compared to water, but is also enhanced by the fact that the floor of the water basin inside the ice tray was insulated with styrofoam. As a consequence of this directional freezing, a layer of ice would form on top of the water before all of the water was fully frozen. When the water underneath the surface ice layer eventually froze, its expansion during phase change would cause the surface to crack, inducing topographical elements into the ice surface. This process is herein referred to as "doming," since the topography would normally take the shape of a dome on the ice surface.

To flatten a domed ice surface after freezing, the surface needed to be conditioned to be nominally smooth. This was done by use of an ice scraper and/or chisel. The dome would be chiseled away, such that there was a slight concave shape in the ice surface. The cavity would then be filled with water and allowed to re-freeze. After refreezing, smaller topographical elements were scraped away using the ice scraper. After scraping,

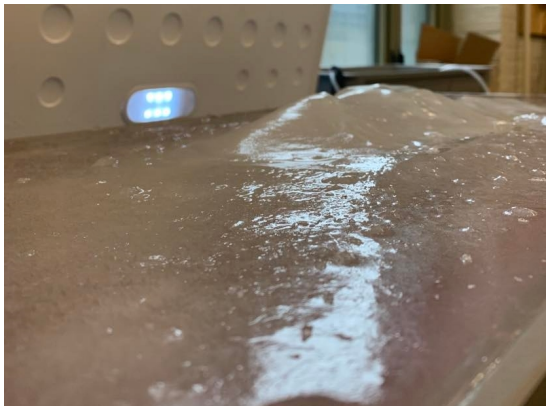

(a) Domed ice surface

(b) Conditioned ice surface

Figure 3.3: Ice tray before and after surface conditioning.

a thin layer of water was applied to the entire surface and allowed to freeze, thus forming a nominally smooth ice surface. Figure 3.3 shows an extreme example of doming in the centre of the ice tray, as well as the same ice surface after being conditioned.

The surface roughness for was quantified by using a Vernier caliper and a bar of known thickness. The bar was laid flat across the fibreglass tray, and the caliper was placed on top of the rod such that the distance from the top edge of the rod to the ice surface could be measured. Measurements of surface roughness were taken at 20 evenly-spaced points along the centreline of the ice surface. Surface roughness measurements were taken for three different glacier models, totalling 60 data points. The root-mean-square roughness value was found to be approximately 0.4 mm, and was subsequently used in section 4.1 to determine whether the ice surface could be reasonably considered as an aerodynamically smooth surface. The centreline surface roughness profiles are presented in Figure 3.4

Ice Formation

Since glacial ice is typically formed by the compression of snow into firn, which then becomes solid ice (Cuffey & Paterson, 2010), different methods of forming ice were considered for best replicating glacial ice in a lab experiment. One such method to recreate glacial ice in a laboratory setting is called sintering, in which chunks of already frozen ice are combined with water and then re-frozen. The larger air gaps between chunks of ice

are filled with water, which then seals them off, mimicking the compression that occurs in real-world glaciers. In practice, using chunks of ice resulted in a rougher surface when compared to simply filling the tray with liquid water and freezing it all at once. Since it was important to ensure the ice was as smooth as possible, the sintering method was not used in this work. Instead, the empty tray was filled to approximately 80% of its capacity with liquid water, then allowed to freeze solid over the course of several days. Once the water had frozen into ice, the remaining 20% was filled with liquid water, which was once again allowed to freeze solid. This method was used to minimize the doming effect discussed above, as well as prevent fracture of the ice tray caused by the expansion of freezing water. After each experiment, the remaining ice was retained inside the tray, which was then filled to the top with liquid water, and allowed to freeze for at least 18 hours before being used for another experiment.

Managing Meltwater

Another important consideration was the management of meltwater accumulated during the experiment. In a real glacier environment, meltwater will percolate through cracks in the glacier surface (potentially refreezing), or run off into streams and rivers (Bash & Marshall, 2014). In these experiments, however, meltwater was accumulated inside of the tray during the experiment. The two options for managing this meltwater were to:

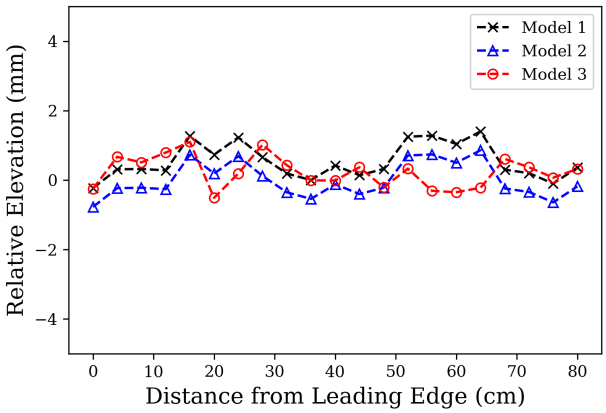

Figure 3.4: Centreline profiles of relative surface roughness for three different glacier models.

a) drain the meltwater throughout the experiment, or b) retain the meltwater inside the tray during the experiment.

Both of these options had advantages and disadvantages. By draining the meltwater during the experiment, the surface over which experiments were made would always be melting ice at 0°C (once the ice had undergone an initial warming period). The ice surface would likely reach a steady state very early in the process, and be more representative of real-world conditions. However, removing meltwater during the experiment would change the height of the ice surface, changing the height of the probe relative to the surface during an experiment. In the atmosphere, small changes in height associated with surface ablation take place over long time scales (several months). However, in a laboratory, the smaller length scales mean that even small changes in height would change the results significantly. Furthermore, if the surface moves below the top of the tray, there would be flow separation beyond the leading edge of the ice tray, changing the nature of the turbulent flow above the ice.

Ultimately, it was decided to retain the meltwater, since variations in height would prevent an accurate evaluation of the measured velocity and temperature over melting ice. By retaining meltwater inside the tray, the volume would not change significantly, keeping the height constant and facilitating the observation of the evolution of turbulent statistics throughout the melt process.

During preliminary experiments, a consequence of the decision to retain meltwater inside of the tray was that after a certain volume of meltwater had accumulated, the ice block would float, protruding above the water line and effectively decreasing the height of the probe relative to the ice surface during the experiment. To overcome this issue and prevent floating of the ice block, three wooden rods were embedded inside of the ice block, and secured to the inner walls of the ice tray using an epoxy resin. They were made of wood to minimize conductive heat transfer to the inner core of the ice block from the rods. These rods served to secure the block of ice in place during an experiment.

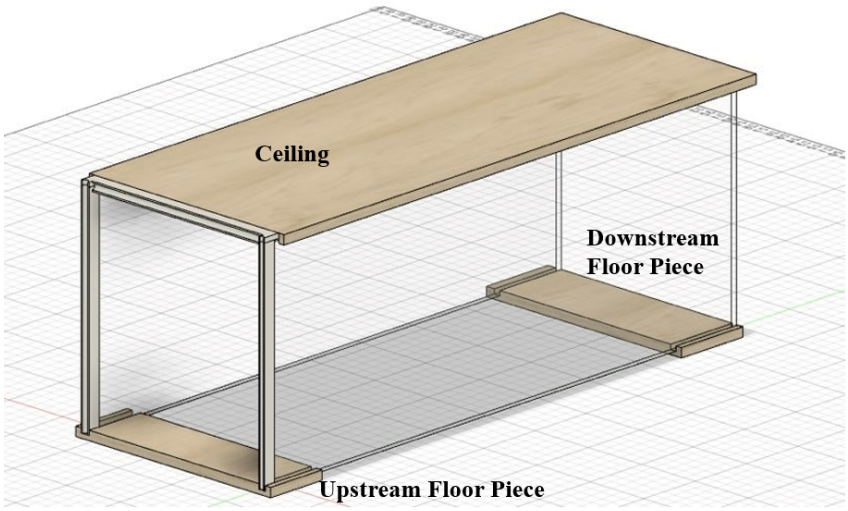

Figure 3.5: Glacier model test section.

3.2.3 Glacier Model Test Section

To fit the glacier model into the tunnel, an extension to the existing test section was designed and built specifically for this work. This glacier model test section had to be designed to facilitate easy insertion and removal of the ice tray. Additionally, it was important that the new section was designed to have sufficiently smooth walls (to prevent additional roughness effects), to be transparent (to allow for photographs and visual observation during experiments), and to be sufficiently water resistant.

To this end, the glacier model section was created with a floorless design, allowing the ice tray to be inserted through the bottom of the tunnel, where it rested on the supporting structure of the test section, sitting flush with the existing tunnel floor. The design of the glacier model section is shown in Figure 3.5, in which the mean flow is from the left to right side of the image, along the length of the section.

The new section consisted primarily of a solid ceiling, made of 1.9 cm thick medium density fibreboard (MDF), measuring 123.2 cm long by 46.4 cm wide, with two long transparent acrylic side walls. The acrylic side walls were 116.8 cm long and 45.1 cm tall, and fit within a long rectangular groove which was machined into the MDF ceiling. The wall material was chosen to be extruded (and not cast) acrylic, to minimize variations in wall thickness. The walls rested on two smaller pieces of MDF of the same thickness

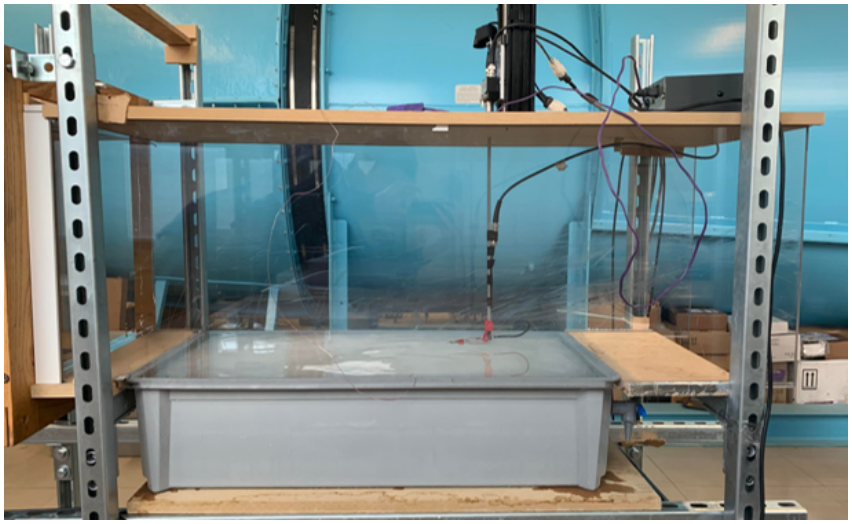

Figure 3.6: Glacier model section as-built.

with a similar groove to that for the ceiling. The upstream floor piece was 12.7 cm long, and the downstream floor piece was 20.3 cm long. The downstream piece fit within the test section support frame such that it could slide back and forth in the downstream direction, to facilitate the positioning of the ice tray within the tunnel. The constructed glacier model test section is shown in Figure 3.6.

The glacier model section was connected to the main wind tunnel test section via two 3D printed transition pieces. The transition pieces matched the tongue-and-groove shapes of the existing wood and acrylic (upstream) wind tunnel walls. Since the wooden side of the existing tunnel had a larger wall thickness than the acrylic side (by 0.64 cm), the channel machined into the MDF ceiling was asymmetrical. The transitional pieces sat within the groove, and were in contact with the acrylic walls, ensuring a continuous and smooth surface on the inner tunnel walls.

3.3 Hot-wire Anemometry and Cold-wire Thermometry

The measurement of turbulent velocity and temperature fluctuations was performed using hot-wire anemometry and cold-wire thermometry, respectively. For an excellent and in-

depth text on hot-wire anemometry, readers are encouraged to consult Bruun (1995). A brief summary of the important principles surrounding these two measurement techniques will nevertheless be provided in the following sections.

The underlying principles of hot-wire anemometry relate to convective heat transfer from a heated cylinder (in this case, a thin wire) to a moving fluid (such as air) – these principles are well-known and understood. The heat transfer is dependent on both the physical properties of the ambient fluid (such as its density, viscosity, thermal conductivity, etc.) and the parameters of the flow – most notably its velocity, temperature, and pressure. Relationships for these parameters are typically expressed using non-dimensional numbers, such as the Reynolds number:

$$Re_D \equiv \frac{\rho U D}{\nu}, \tag{3.1}$$

and the Nusselt number:

$$Nu_D \equiv \frac{hD}{k}, \tag{3.2}$$

where h is the convective heat transfer coefficient, D is the wire diameter, and k is the thermal conductivity of the fluid. Following the work of King (1914), the relationship between these has often been described by:

$$Nu = A + B \cdot Re^n, \tag{3.3}$$

where A, B, and n ($\approx 1/2$) are constants for a specific fluid and anemometer combination.

A constant-temperature anemometer (or CTA) is a device that supplies a variable voltage to a very fine wire (on the order of 2-5 μm) in a cross-flow, such that the wire is heated above ambient temperature. The voltage (E) supplied is such that the wire is maintained at a constant temperature (resistance). The heat transfer from the wire (which is dominated by convection) is balanced by the power input from the CTA. Given

that the convective heat transfer from the wire is given by:

$$Q = hA_s(T_w - T_\infty), \tag{3.4}$$

where A_s is the wire surface area and T_w is the wire temperature. The electrical power provided by the CTA is:

$$P = \frac{E^2}{R_w}, \tag{3.5}$$

where R_w is the resistance of the heated wire. It is then possible to relate the convective heat transfer to the CTA voltage by combining equations (3.1)-(3.5), where one obtains an equation that relates the CTA voltage to the fluid velocity:

$$\frac{E^2}{R_w} = (A + BU^n)(T_s - T_\infty). \tag{3.6}$$

Equation (3.6) exists under the assumption that King's equation (3.3) is accurate, that the fluid properties (k, ν, etc.) are constant, and that the wire surface temperature is known. In reality, there is no practical way to measure the wire surface temperature exactly. Instead, it is assumed that the wire's resistivity changes with temperature. In this way, if the wire is held at a constant resistance during operation, it can be assumed that the wire temperature is also constant. The ratio of the operating resistance (R_w) to the ambient resistance of the wire when the CTA is not being operated (R_a) is called the overheat ratio (Bruun, 1995). Setting the overheat ratio to a constant value allows the user to ensure that the wire temperature T_w is constant. Equation (3.6) can be simplified to the commonly-used hot-wire calibration equation:

$$E^2 = A^* + B^* U^n. \tag{3.7}$$

If the hot-wire is calibrated in a flow with a known velocity at a known temperature, the temperature-dependent constants A^* and B^*, and exponent n can be calculated and used to transform CTA voltage into velocity measurements in an experiment. The exponent n

is not expected to change significantly with temperature (Lienhard, Helland, et al., 1989), such that an average value ($\bar{n}$) across several calibrations is often used in place of the exponent n in equation (3.7). Lienhard, Helland, et al. (1989) found relations between the coefficients (A^* and B^*) and the fluid temperature (T), such that:

$$A^* = \bar{A}(T_{w_A} - T)T_f^{0.84}, \tag{3.8}$$

and:

$$B^* = \bar{B}(T_{w_B} - T), \tag{3.9}$$

where $\bar{A}$ and $\bar{B}$ are constants, T is the fluid temperature, T_f is the film temperature between the wire and fluid temperatures, and T_w is a constant representing the wire surface temperature. It is not necessary that T_{w_A} and T_{w_B} be equal, though they should be relatively similar.

Similar to hot-wire anemometry, cold-wire thermometry is a technique to measure temperature with high spatial and temporal resolution within a flow. A cold-wire thermometer is simply a type of resistance temperature detector (RTD), in which the resistance of a fine wire changes in response to changes in local fluid temperature. The setup is similar to that of the hot-wire, but the wire material itself is often different. Hot-wires are commonly made of Tungsten, whereas cold-wires usually consist of Platinum or a Platinum alloy. However, the main difference between a hot-wire anemometer and cold-wire thermometer are the methods of operation. Cold-wires are operated using a "constant-current anemometer" (or CCA), which supplies a constant, low current to the wire. The current must be low enough as to not heat the wire, so that the wire is only heated or cooled by the flow – this is usually on the order of 0.1 mA, such that the wire will experience no electrical heating, thereby remaining insensitive to velocity changes (Bruun, 1995). Given a constant current, the voltage drop across the cold-wire can be related to the wire resistance and therefore the temperature.

Hot-wire anemometry and cold-wire thermometry offer good signal-to-noise ratios,

excellent temporal and spatial resolutions, and are also relatively low-cost and practical to implement for wind tunnel experiments. Hot-wires and cold-wires allow a user to resolve turbulent fluctuations down to dissipation scales, making them useful tools for making measurements of the full range of scales in turbulent flows.

Together, two hot-wires oriented in an X-pattern (usually referred to as an X-wire) while operated in very close proximity to a cold-wire (as shown in Figure 3.7) render possible the simultaneous measurement of turbulent fluctuations of two-components of velocity and temperature, facilitating the calculation of joint statistics of velocity and temperature (Berajeklian & Mydlarski, 2011). This was the primary measurement technique used in this research. Section 3.4 describes the procedure used for calibrating hot- and cold-wires in this work.

Figure 3.7: Simultaneous operation of an X-wire (left) and cold-wire (right). The X-wire is aligned with the mean flow, while the cold-wire is angled by 12° relative to the mean flow since it is insensitive to changes in velocity.

3.4 Calibration

3.4.1 Calibration of Hot-wire Probes

The hot-wire probes were calibrated using a TSI 1128 Air Velocity Calibrator, in which a controllable jet of compressed air was was cooled to sub-ambient temperatures by passing the compressed air line through an ice-water bath. Once the air temperature at the jet exit had stabilized, the compressed air line was removed from the ice-water bath and allowed to naturally return to room temperature, slowly increasing the jet exit temperature.

Before calibrating the hot-wires, the combined resistance of the cable (R_c) and probe support (R_p) was measured on each channel using a shorting probe. This resistance, along with the lead resistance (R_L) was subtracted from the overall resistance measured after the shorting probe was replaced with the actual hot-wire probe. The total resistance (R_T) measured can be described as (Hewes, Medvescek, Mydlarski, & Baliga, 2020):

$$R_T = R_a + R_c + R_p + R_L, \tag{3.10}$$

where R_a is the ambient resistance of the wire. It was assumed that the resistance of the cable, probe support, and leads remained constant, such that R_T was only sensitive to changes in the temperature of the wire. The overheat ratio ($\frac{R_w}{R_a}$) was then set to 1.8 during the anemometer's operation.

The hot-wires were then placed at the jet exit, where the flow was effectively laminar. The axis of the probe support was aligned with the mean flow direction. A differential pressure transducer was used to measure the pressure difference between the jet plenum and exit, which was used to calculate the true velocity at the jet exit. The velocity was systematically varied and the corresponding anemometer voltages for both wires were recorded. This process was repeated for several different known flow temperatures, measured using a type-E thermocouple placed very close to the X-wire, to quantify the effect of the temperature on the hot-wire voltages. For each calibration, the fluid tempera-

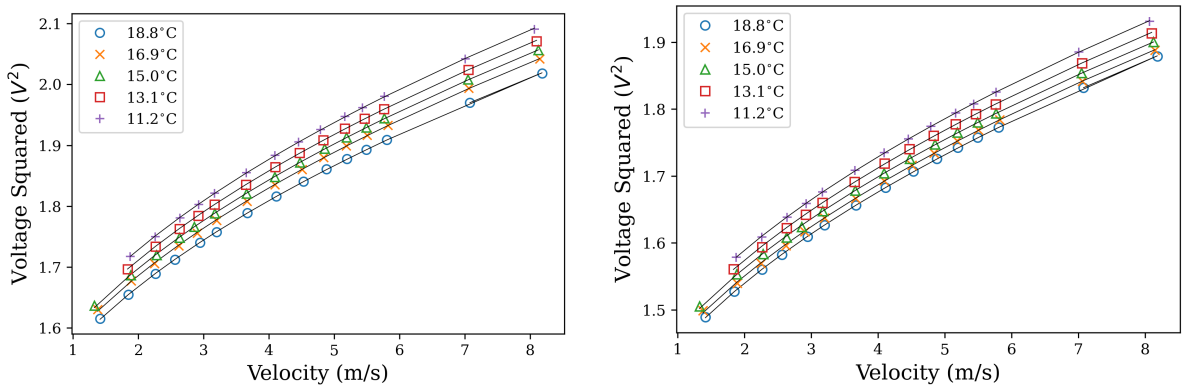

(a) Wire 1 (b) Wire 2

Figure 3.8: Adjusted hot-wire calibration curves for various fluid temperatures.

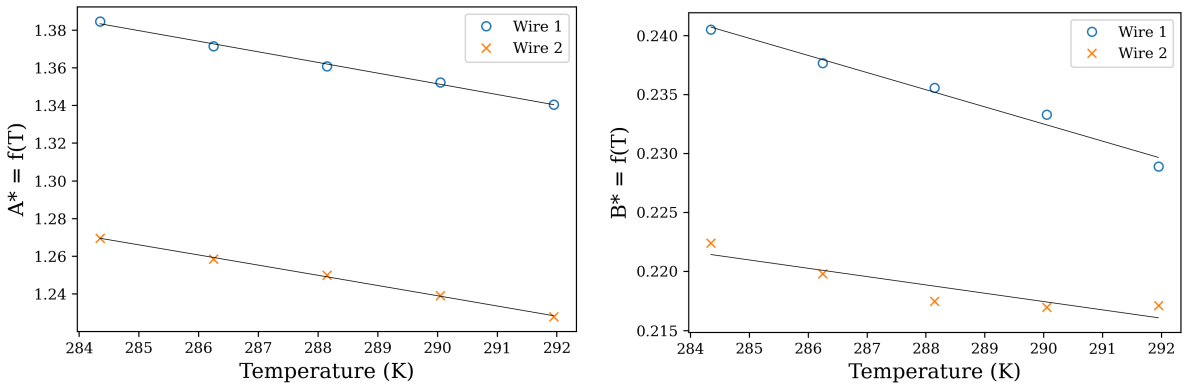

(a) Curve fit for Equation 3.8 (b) Curve fit for Equation 3.9

Figure 3.9: Temperature-dependent hot-wire calibration coefficients A^* and B^*.

ture was held constant to within 0.1°C. The anemometer voltages for each wire were fit to equation (3.7). The average exponent from all of the isothermal calibrations ($\bar{n}$) was calculated, and the voltages were then re-fit using the new, average exponent. The calibration curve fits are shown in Figure 3.8.

The curve fits for A^* and B^* are presented below in Figure 3.9. The data are well-fit by Equations 3.8 and 3.9 in this case, reducing the overall error associated with the calibration. For these calibrations, the difference between T_{w_A} and T_{w_B} was about 30°C, which is less than 10% of T_w, and therefore determined to be adequate. Since the hot-wires in an X-wire configuration are not perpendicular to the mean flow, they experience both longitudinal and transverse cooling effects. Using the velocities for both wires obtained from the calibration equations, it is necessary to transform the apparent

velocities (U_1 and U_2) into instantaneous orthogonal components ($\tilde{U}$ and $\tilde{V}$). To perform this transformation, the method of Browne, Antonia, and Chua (1988) was used, where the so-called effective velocity experienced by a wire, U_{eff}, is defined as the velocity that would produce the same voltage output as if the wire was normal to the flow. Here,

$$U_{eff} = \tilde{U}\left(cos^2(\theta_{eff}) + k^2 sin^2(\theta_{eff})\right)^{1/2}, \tag{3.11}$$

where k^2 represents the effects of longitudinal cooling (set to 0.03, (Bruun, 1995)), and θ_{eff} is the effective angle of the wire. To find the effective angle, the hot-wires were further calibrated by yawing them with respect to the calibration jet from -30° to 30° in 6° increments, while the velocity was held constant. At each position, the effective velocity was calculated for each wire. Since at any point in time, the two hot-wires experience the same instantaneous velocity, the effective angle equations become:

$$U_1\left(cos^2(\theta_1) + k^2 sin^2(\theta_1)\right)^{1/2} = U\left(cos^2(\theta_1 - \psi) + k^2 sin^2(\theta_1 - \psi)\right)^{1/2}, \tag{3.12}$$

$$U_2\left(cos^2(\theta_2) + k^2 sin^2(\theta_2)\right)^{1/2} = U\left(cos^2(\theta_2 - \psi) + k^2 sin^2(\theta_2 - \psi)\right)^{1/2}, \tag{3.13}$$

where U_1 and U_2 are the apparent velocities for each wire, ψ is the incoming angle with respect to the mean flow, and U is the magnitude of the true velocity. Knowing the angle ψ, the effective angles were calculated for each position, and then averaged across all ten yaw angles. For processing of experimental data, the measured velocity could then be decomposed into $\tilde{U} = Ucos(\psi)$ and $\tilde{V} = Usin(\psi)$ if the angle ψ was known. In practice, the Newton-Raphson method was used to iteratively solve for ψ. These effective angles are assumed to be temperature-invariant constants, as they are a geometric property of the actual wire angles, and so the yaw-sweep was only performed at room temperature.

Another important aspect to consider regarding the calibration and use of the hot-wire probes was the influence of humidity on the velocity measurements. Since a sub-ambient temperature flow is likely to have a higher relative humidity than a heated flow, and both the calibration and experiments were performed in flows cooled to some degree, it was

necessary to consider potential effects of humidity on hot-wire measurements. Although humidity corrections for hot-wire anemometry calibration equations exist (Durst, Noppenberger, Still, & Venzke, 1996), these were not implemented in this research for the following reasons:

1. The sensible flux caused by the temperature gradient is expected to far outweigh the latent flux caused by a supposed humidity gradient (Conway & Cullen, 2013);

2. The temperature fluctuations at the experimental measurement heights (typically less than 10°C) were not large enough to induce significant changes in humidity relative to the ambient air;

3. A moisture filter was used to remove excess water droplets and vapour from the flow in the calibration jet;

4. The error associated with humidity in velocity measurements was negligible for the low Reynolds numbers investigated in this work (see Durst et al., 1996).

3.4.2 Calibration of Cold-wire Probes

The calibration procedure for the cold-wire was performed in the same physical apparatus as the hot-wire calibration. The jet of compressed air was brought down to approximately 12°C using the aforementioned ice-water bath, then allowed to naturally return to room temperature while keeping the jet velocity constant. Before calibrating the cold-wire, it was necessary to dynamically balance the CCA using the current injection method of Lemay and Benaïssa (2001) to improve the sensor's response to small temperature fluctuations. After dynamically compensating the CCA, the current was set to 0.15 mA, and a gain was applied to the output signal to adequately cover the ± 5V range of the A/D board. The cold-wire was then placed at the jet exit, near a type-E thermocouple connected to a digital display. As the temperature of the jet increased, the cold-wire voltage was measured. Measurements were taken in increments of 0.50°C. Data were averaged across 10 blocks of 512 samples recorded at a sampling frequency of 200 Hz.

The temperature measured by the thermocouple was plotted as a function of the average voltage, and then curve fit using least-squares linear regression. A typical calibration is presented below in Figure 3.10. To validate the linearity of the cold-wire calibration, a second-order polynomial was also fit to the data, wherein the second-order coefficient was found to be 0.0848 °C/V^2. The magnitude of the second-order term was found to be less than 10% of the first-order term, such that the curve was deemed sufficiently linear.

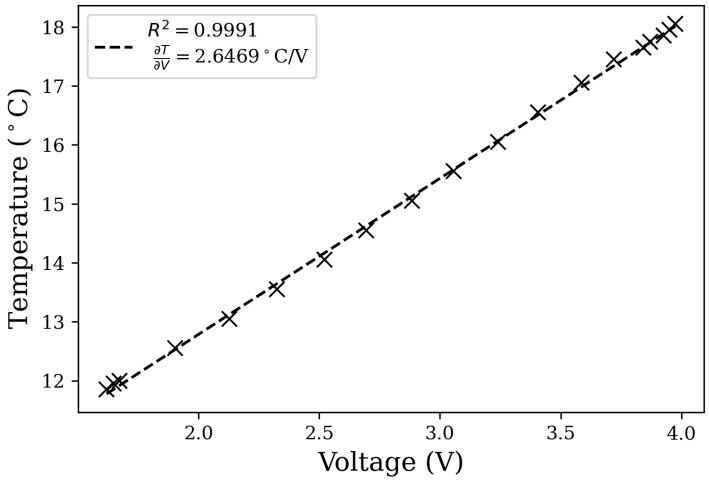

Figure 3.10: Calibration curve for cold-wire.

3.5 Data Acquisition and Analysis

Data for the experiments in the present work were acquired using a National Instruments BNC-2110 16-bit A/D board. The velocity measurements were obtained using a Dantec Streamline Pro CTA connected to a TSI 1241 X-wire probe, made of 5 μm Tungsten wire. The temperature measurements were obtained using a custom-built CCA by Université Laval that was characterized by Lemay and Benaïssa (2001), and was connected to a 1.25 μm Wollaston wire mounted on a TSI 1210 single-wire probe. The analog CTA signal was low-pass filtered at 3 kHz using the onboard signal conditioner from the Dantec Streamline Pro CTA to remove electronic noise not caused by turbulent velocity fluctuations, then subsequently high-pass filtered at 0.05 Hz using a Krohn-Hite 3384 filter. A gain of 20 dB was applied to the high-pass filtered hot-wire output to optimize the analog-to-digital

conversion range. Both the low-pass and band-pass filtered signals from the hot-wires were recorded using the A/D board. The analog CCA signal was low-pass and high-pass filtered at 3 kHz and 0.05 Hz (respectively) using a Krohn-Hite 3384 filter. No gain was required for the filtered cold-wire signal.

A Dantec Streamline thermistor temperature probe was placed upwind of the hot- and cold-wire assemblies to record the ambient temperature of the flow throughout the course of the experiment. The output of the temperature sensor was transformed into temperature using the calibration curve provided by the manufacturer.

Data were acquired in blocks of 16384 samples, measured at a frequency of 6000 Hz (i.e., twice the low-pass filter frequency) to satisfy the Nyquist criterion. A LabView VI was used to acquire and format the voltage data, writing it to a text file stored on a local hard drive. A FORTRAN code was then used to transform the raw voltages into velocities and temperatures. Due to the transient nature of the experiments, statistical moments and cross-moments of velocity and temperature were calculated by averaging over 50-block (approximately 2 minute) sub-intervals. This interval size was selected to ensure "instantaneous" statistical convergence within any given interval, while simultaneously avoiding transient changes caused by actual physical phenomena over the (4.5 hour) total duration of individual experiments.

3.6 Experimental Procedures

3.6.1 Experimental Set-up

After calibrating the equipment, the hot- and cold-wires were installed inside the wind tunnel test section. The probe support was connected to a 90° elbow, the resistance of which was included as part of the new cable and support resistance. Two custom-designed, 3D-printed pieces were used to position the X-wire and cold-wire within 1 mm of each other. The cold-wire was angled at approximately 12° to the mean flow inside the horizontal plane, since it was largely insensitive to changes in velocity. It was connected

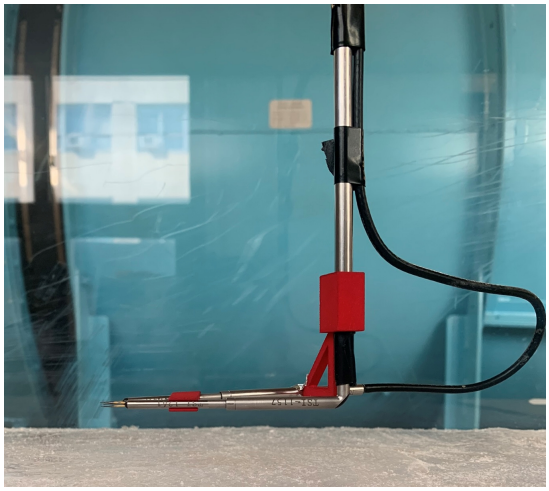

(a) Left side (hot-wire closest)

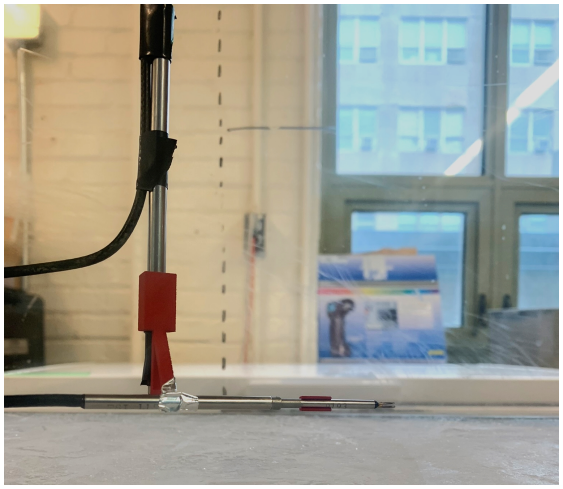

(b) Right side (cold-wire closest)

Figure 3.11: Side views of hot- and cold-wire probe setup.

to a TSI-1151 flexible probe support, which was secured to a probe shield housing the TSI-1155 18" probe support for the X-wire. The flexible probe support was connected to a 5 m BNC cable running from the ceiling of the tunnel out of the back end, in order to avoid disturbing the flow near the ice patch, as well as to avoid cooling of the cable (therefore causing potential changes in the resistance and dynamic balancing of the CCA). The experimental probe setup is shown in Figure 3.11

The X-wire probe support was attached to a MN10-0050-M02-21 Velmex Bislide traversing mechanism, equipped with a Vexta PK264-03A-P1 Stepper Motor. The traversing mechanism had a range of approximately 10 cm, and was used to control the vertical position of the probes within the tunnel. The probe support passed through the ceiling of the tunnel through a hole drilled into the tunnel ceiling along the centreline. In the present work, the measurement probe was approximately 3.5 m downstream from the of the active grid. For these experiments, measurements were made at approximately 60% of the total ice patch length. The unheated starting length (i.e. the distance between the trailing edge of the grid and leading of the ice) was approximately 3 m.

Figure 3.12: Empty tunnel setup for baseline measurements.

3.6.2 Baseline Measurements

Before making simultaneous measurements of velocity and temperature over melting ice, it was important to characterize the background flow in the tunnel in the absence of ice (herein referred to as an "empty" tunnel, as shown in Figure 3.12). Although no temperature fluctuations were expected to occur, simultaneous velocity and temperature measurements were nevertheless recorded. A substitute for the ice tray, composed of a geometrically identical tray with a sealed wooden lid, was inserted into the tunnel floor.

For each free-stream velocity, a baseline profile was established. This was done by positioning the wire as close as possible to the tunnel floor, taking a measurement composed of 50 blocks of 16384 samples recorded at 6000 Hz, then moving the wire towards the tunnel centreline. At the three measurement heights (y = 10, 25, and 40 mm), 200 blocks of 16384 samples were recorded at 6000 Hz to facilitate the calculation of baseline spectra and co-spectra. The profiles were used to define the boundary layer height (δ) as the height at which the local velocity was equal to 98% of the free-stream velocity, approximately 7.5 cm for all three speeds in the test envelope. While 99% is typically

used as the threshold for determination of the boundary layer height (Pope, 2000), 98% was used in this case to improve the estimates of the boundary layer heights given the (small) uncertainty associated with the velocity measurements (see Appendix B).

Finally, noise measurements for the cold-wire were recorded in the wind tunnel in the absence of (the glacier model and) temperature fluctuations, to aid in the post-processing of the data. To this end, spectra of the cold-wire signal in the absence of ice (or any other temperature forcing) were evaluated for three different flow speeds at the middle measurement height (25 mm). The noise spectra and procedure for removing noise from the velocity and temperature spectra are presented in Appendix A.

3.6.3 Experiments over Ice

For the main experiments in this research, statistics of velocity and temperature were measured over the surface of the glacier model as it melted. For each experiment, the glacier model was removed from the freezer and placed inside the glacier model test section. Once it was aligned properly inside the tunnel, the measurement probe was lowered until the wire apparatus was as close as possible to the ice surface (see Appendix B). After bringing the probe as close as possible to the ice surface, it was raised to either 10, 25, or 40 mm (the measurement heights) using the traversing mechanism. Due to the transient nature of the melting ice surface, profile measurements over melting ice were not possible within the scope of the present work, given that the statistics of velocity and temperature were found to evolve in time with the changing surface temperature. After successfully positioning the probe above the ice, the wind tunnel fan was turned on, along with the active grid. Temperature values from the thermocouple embedded in the glacier model were read off a digital display and recorded by hand. Data collection was initiated once the internal thermocouple temperature was approximately -10°C. Figure 3.13 shows the experimental setup during one of the experiments performed over ice.

Figure 3.13: Experiments performed over ice.

3.7 Experimental Uncertainty

A detailed analysis of the experimental uncertainty in this work is performed in Appendix B. The overall uncertainty associated with the velocity measurements, including the effects of the uncertainty in the temperature measurements, was found to be 4.1% to achieve a 95% confidence interval. For the temperature measurements, the uncertainty from the cold-wire was found to be approximately 0.97% for a 95% confidence interval. Finally, the uncertainty on the absolute temperature measurements from the sub-surface type E thermocouple was approximately 0.13%, or 0.35 K with respect to a mean sub-surface temperature of 272 K (-1 °C). The repeatability of the velocity and temperature measurements was evaluated in Appendix C, where it was found to be satisfactory.

Chapter 4:

Results and Discussion

This chapter contains the results and discussion pertaining to the experiments performed as part of this work. Section 4.1 characterizes the turbulent velocity field in the empty tunnel (without ice), serving as a baseline for comparison to the statistics of the (steady) turbulent velocity field over melting ice, which is discussed in section 4.2. Given that the ice was melting throughout the course of the experiments, its transient evolution is investigated in section 4.3, as well as the changing (temperature-related) quantities measured in the turbulent boundary layer above it, using local averages. The statistics of velocity were not found to change significantly in time. To compare the turbulent velocity and temperature statistics measured over melting ice at the three different measurement heights and for the three free-stream velocities, subsets of the data were evaluated at an equivalent non-dimensional time in the melt process for all nine runs. An analysis of the temperature and combined velocity-temperature statistics measured over melting ice during this period is performed in section 4.4, to complement the analysis done for the velocity field in section 4.2. Finally, the turbulent heat fluxes over melting ice are parameterized in section 4.5, wherein the results are compared to the existing bulk method commonly used by glaciologists in surface energy balance studies.

4.1 Characterization of Background Flow

Before performing experiments over melting ice, velocity measurements were undertaken in the turbulent boundary layer of the "empty" tunnel, to characterize the background flow. Measurements of streamwise (horizontal) (u) and transverse (vertical) (v) velocity were made to characterize the turbulent boundary layer. The principal quantities of interest were the mean velocity ($\langle U \rangle$), root-mean-square (RMS) velocity (u_{rms}), and the Reynolds stress ($\langle uv \rangle$). These quantities are presented non-dimensionally in Figure 4.1

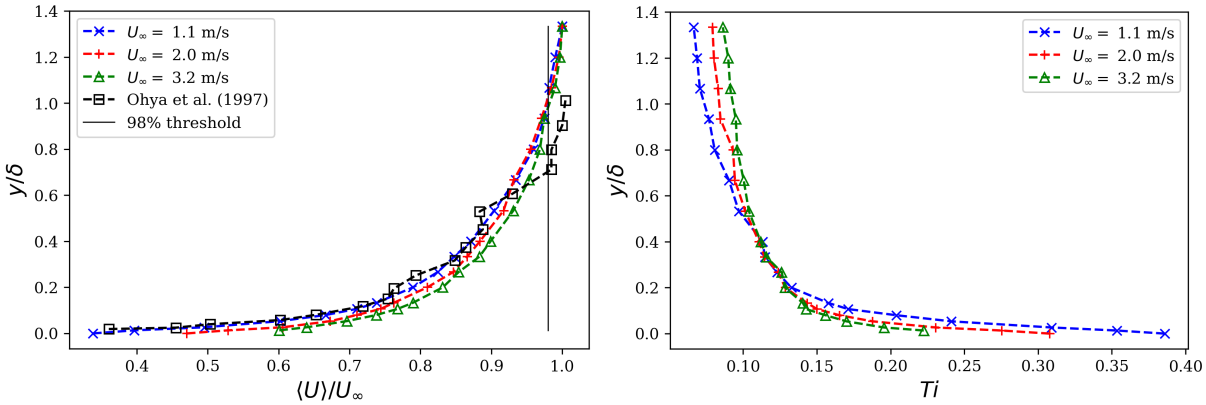

(a) Non-dimensional mean velocity

(b) Turbulent intensity

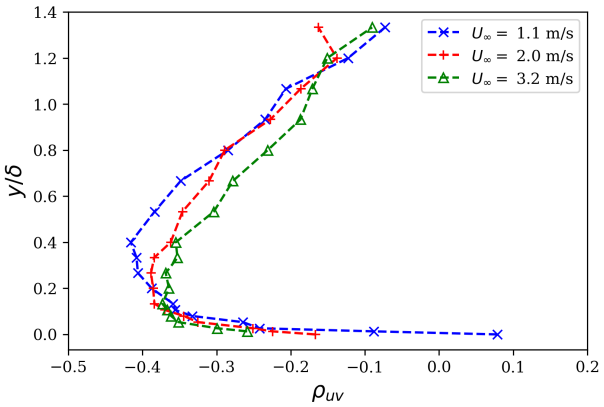

(c) Correlation coefficient

Figure 4.1: Non-dimensional profiles in the turbulent boundary layer.

for free-stream velocities (U_∞) of 1.1, 2.0, and 3.2 m/s, where they are scaled by the free-stream velocity, local mean velocity, and product of u_{rms} and v_{rms}, respectively. The latter two non-dimensional quantities form the turbulent intensity (Ti) and correlation coefficient (ρ_{uv}), respectively.

The non-dimensional mean velocity profiles of Figure 4.1 (a) are similar for all three free-stream velocities investigated, but do show a Reynolds-number dependence as expected. They show good agreement with prior results in the literature for turbulent boundary layers (e.g. Ohya et al., 1997). The shape factors (Pope, 2000) were found to be 1.33, 1.25, and 1.21 for the 1.1, 2.0, and 3.2 m/s free-stream velocities, respectively. From y/δ=0.1 to 0.5, the turbulent intensity profiles (Figure 4.1 (b)) are similar, but diverge outside of this range, where the turbulent intensity is greater for higher free-stream velocities when y/δ >0.5, and the turbulent intensity decreases for higher free-stream

velocities when y/δ <0.1. In general, the correlation coefficient ρ_{uv} should be approximately -0.4 in the core region of a turbulent boundary layer (Tennekes & Lumley, 1972), which is consistent with the observations in Figure 4.1 (c).

The mean velocity profiles were then used to estimate the friction velocity (u_*). While the primary experiments of the present work were performed in the outer region of the boundary layer (y/δ>0.1), such that u_* could not be calculated from the velocity gradient at the wall (which requires a miniature single-wire probe), calculation of the friction velocity was necessary for quantifying the roughness of the ice surface. Two different methods were used to estimate the friction velocity from the baseline velocity profiles.

In the first method, the velocity defect law (Tennekes & Lumley, 1972):

$$\langle U \rangle - U_\infty = \frac{u_*}{\kappa} \ln\left(\frac{y}{\delta}\right), \tag{4.1}$$

was used to model the mean velocity profile. By re-arranging equation (4.1), the friction velocity was calculated for each point in the profiles over the range $0.1 < y/\delta < 1.0$. The average friction velocity was then computed from the values calculated at each height.

In the second method, the normalized wall shear stress (i.e., the skin friction coefficient C_f) was used to find the wall shear stress. The skin friction coefficient is defined as:

$$C_f \equiv \frac{\tau_w}{\frac{1}{2}\rho U_\infty^2}, \tag{4.2}$$

and has been quantified using empirical correlations for a turbulent boundary layer, such as that given by Prandtl (1925):

$$C_f = 0.027\,(Re_x)^{-1/7}, \tag{4.3}$$

where x represents the downstream distance from the grid (approximately 3.5 m). Combining equations (4.2), (4.3), and (2.24) enabled the calculation of the friction velocity.

The estimated friction velocity using both methods is presented in Table 4.1, along

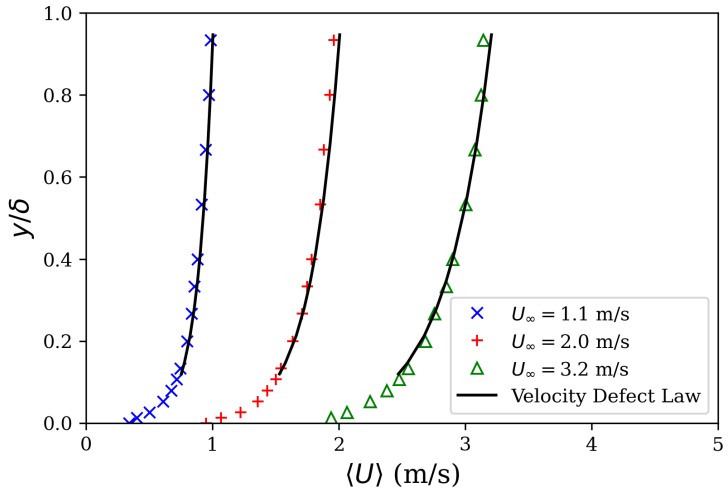

Figure 4.2: Profiles of velocity fitted to theoretical predictions.

with the inferred roughness Reynolds number (R_k) for the ice using the average of the two estimates of u_* for a given free-stream velocity. It can be seen that using the velocity defect law results in slightly larger values of u_*. However, in all cases, R_k is small enough (i.e. < 5) to justify the neglect the effects of surface roughness on the turbulent boundary layer over the ice, and treating the glacier model as an aerodynamically smooth surface.

U_∞ (m/s)	u_* (m/s)			$R_k \left(= \frac{u_* k_{rms}}{\nu}\right)$
	Velocity Defect	Prandtl's Correlation	Average	
1.1	0.0739	0.0486	0.0613	1.63
2.0	0.1467	0.1040	0.1195	3.19
3.2	0.1963	0.1426	0.1695	4.52

Table 4.1: Estimated friction velocities and corresponding values of R_k.

Using the friction velocity obtained using Prandtl's correlation (equation (4.2)), the velocity profiles were validated in Figure 4.2 against the velocity defect law (solid lines) in the region where $y/\delta > 0.1$ for the three free-stream velocities used herein. It can be seen that the velocity defect law fits the profiles well, confirming the accuracy of the friction velocity estimates obtained using Prandtl's correlation.

In addition to the basic statistics presented in Figure 4.1, further characterization of the background flow was performed at the three heights for which the measurements over ice were made. This analysis consisted of calculating of other relevant quantities (such as ϵ, λ, and η), as well as spectra and probability density functions (PDFs) of the velocity

y (mm)	10			25			40		
U_∞ (m/s)	1.1	2.0	3.2	1.1	2.0	3.2	1.1	2.0	3.2
$\langle U \rangle$ (m/s)	0.88	1.58	2.49	0.98	1.76	2.77	1.03	1.85	2.92
T_∞ ($^\circ C$)	18.1	18.0	18.1	18.1	18.0	17.9	18.0	18.0	18.0
u_{rms} (m/s)	0.110	0.198	0.235	0.089	0.177	0.303	0.080	0.162	0.293
v_{rms} (m/s)	0.043	0.095	0.166	0.047	0.099	0.173	0.046	0.100	0.181
$-\langle uv \rangle$ $(m/s)^2$	0.0018	0.0080	0.0229	0.0016	0.0071	0.0199	0.0012	0.0062	0.0180
ϵ (m^2/s^3)	0.117	0.175	0.511	0.103	0.119	0.280	0.098	0.098	0.205
ℓ (m)	0.065	0.075	0.96	0.082	0.090	0.12	0.070	0.11	0.13
λ (mm)	4.8	7.1	6.8	4.1	7.7	8.6	3.8	7.8	9.7
η (mm)	0.41	0.37	0.29	0.43	0.41	0.33	0.43	0.43	0.36
$-\rho_{uv}$	0.38	0.43	0.42	0.38	0.41	0.38	0.33	0.39	0.34
R_ℓ	481	998	2090	486	1068	2381	378	1147	2506
R_λ	35	94	148	25	91	175	20	84	190

Table 4.2: Baseline velocity statistics for the tunnel without the glacier model.

fluctuations. The dissipation rate was calculated using Taylor's frozen-flow hypothesis (Taylor, 1938) and assuming local isotropy such that:

$$\epsilon = \frac{15\nu}{\langle U \rangle^2} \left\langle \left(\frac{\partial u}{\partial t} \right)^2 \right\rangle. \tag{4.4}$$

The Taylor microscale was calculated using equation 2.13 to be able to calculate the Taylor-microscale Reynolds number, R_λ, defined as:

$$R_\lambda \equiv \frac{u_{rms}\lambda}{\nu}. \tag{4.5}$$

These characterizations served as a baseline for comparison of the velocity statistics over melting ice. The baseline quantities of the flow are presented in Table 4.2.

The one-dimensional wavenumber spectra, $E_u(\kappa_1)$ and $E_v(\kappa_1)$, of the velocity fluctuations are presented non-dimensionally in Figure 4.3. A smoothing algorithm was used to minimize peaks in the spectra caused by electronic noise – it is detailed in Appendix A. The width of the inertial range of the spectra was found to increase with Reynolds number, and tended towards a $-5/3$ slope. The slope of the u velocity spectra was typically steeper than that of the v velocity, consistent with prior observations (e.g. Mydlarski & Warhaft, 1996). Overall, the non-dimensional spectra show little sensitivity to the

measurement height. The non-dimensional streamwise velocity spectra collapse well for the two higher speed runs, while the lowest speed runs are smaller in magnitude. This difference is likely attributable to different Reynolds numbers of the 3 flows, given that $R_\lambda > 80$ for the higher-speed cases and $R_\lambda < 40$ for the lower speed one.

PDFs of the streamwise (u) and vertical (v) velocity fluctuations were computed, then non-dimensionalized using their RMS values, and are presented in Figure 4.4. A normalized Gaussian PDF was plotted along with the velocity PDFs. They appear nearly Gaussian, with slight deviations from Gaussian behaviour in the tails. These deviations are more apparent in the vertical than the streamwise velocity fluctuations.

In addition to the spectra and PDFs of the two velocity components presented above, co-spectra and joint PDFs of the velocity fluctuations were also computed. The magnitude of the co-spectrum, $\Lambda_{uv}(\kappa_1)$, was scaled by the corresponding velocity spectra to form the non-dimensional coherence spectrum:

$$H_{uv}(\kappa_1) \equiv \frac{\Lambda_{uv}(\kappa_1)}{E_u(\kappa_1)E_v(\kappa_1)}. \tag{4.6}$$

The coherence spectra for the baseline cases are presented in Figure 4.5. Closer to the wall, there is higher coherence at larger Reynolds numbers (i.e. free-stream velocities) due to the stronger correlations of u and v. Similarly, joint PDFs of u and v were also computed, and were found to be nearly joint-Gaussian. They did not show significant sensitivity to the height or free-stream velocity, such that only three of the nine cases are presented in Figure 4.6 as characteristic representations of the joint PDFs of u and v.

Lastly, PDFs of the instantaneous Reynolds stress (uv) were computed and non-dimensionalized similar to those of the single-component velocity PDFs. They are presented in Figure 4.7, where it is observed that the PDFs collapse at all free-stream velocities for the lowest measurement height. The tails of the PDFs decrease more rapidly at lower speeds for the other two measurement heights. There is an exponential decay in the tails of the PDFs of uv, an expected consequence of the nearly joint-Gaussian distribution, and agreeing well with the literature (e.g. Mydlarski, 2003).

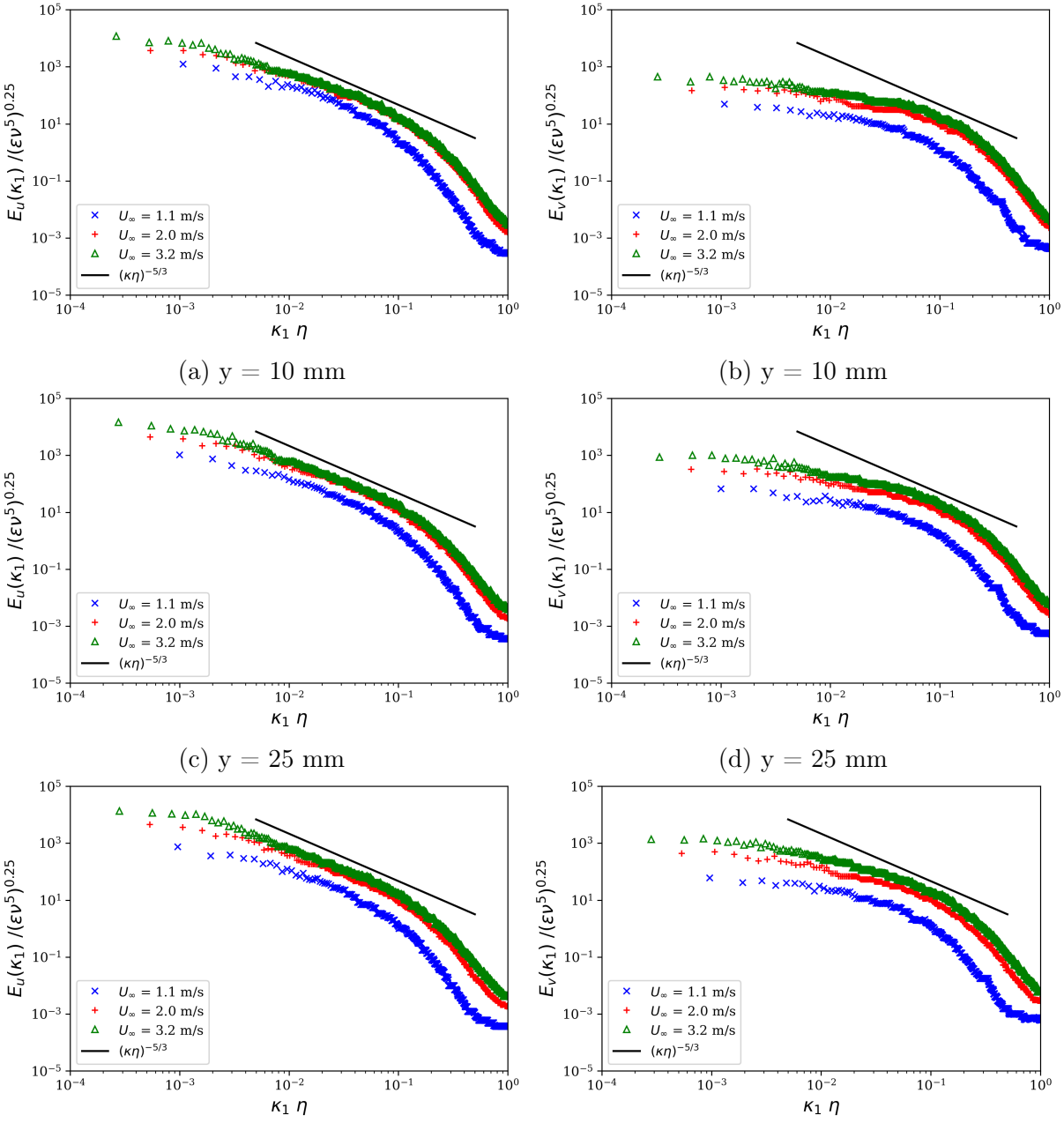

(a) y = 10 mm (b) y = 10 mm

(c) y = 25 mm (d) y = 25 mm

(e) y = 40 mm (f) y = 40 mm

Figure 4.3: Baseline non-dimensional wavenumber spectra of streamwise (a,c,e) and vertical (b,d,f) velocity fluctuations, where $\kappa_1 = 2\pi f / \langle U \rangle$. The straight line is a -5/3 power-law.

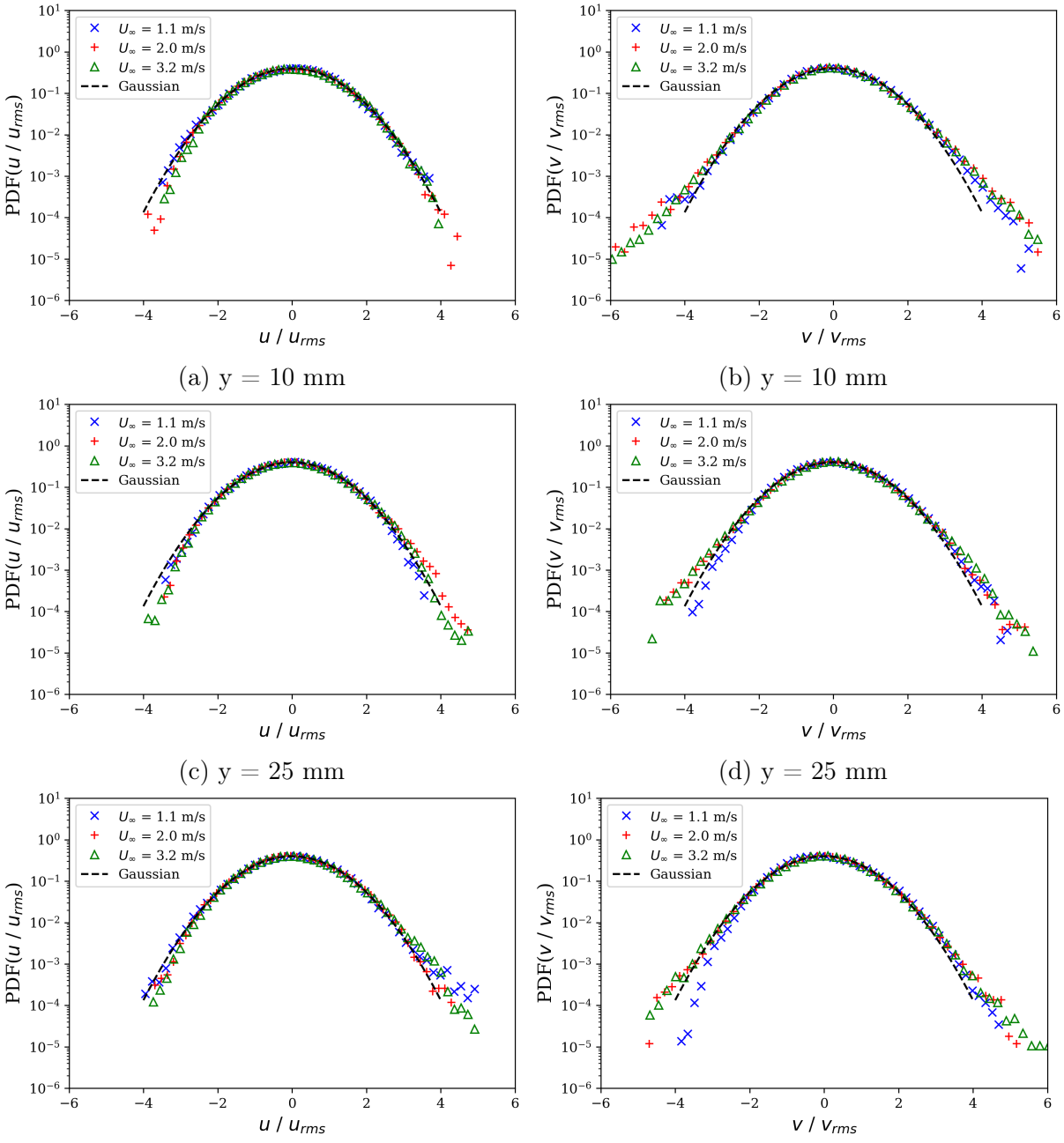

(a) y = 10 mm

(b) y = 10 mm

(c) y = 25 mm

(d) y = 25 mm

(e) y = 40 mm

(f) y = 40 mm

Figure 4.4: Baseline streamwise (a,c,e) and vertical (b,d,f) velocity PDFs.

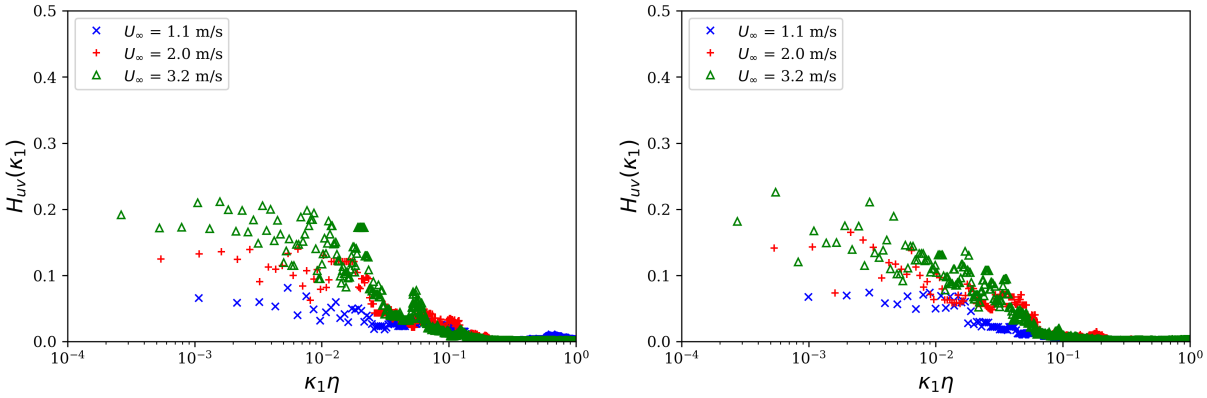

(a) y = 10 mm (b) y = 25 mm

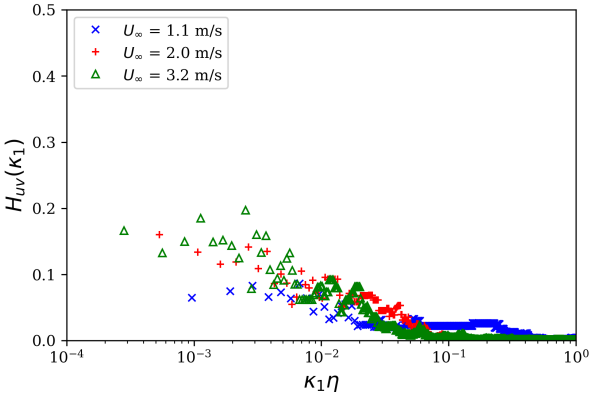

(c) y = 40 mm

Figure 4.5: Non-dimensional coherence spectra of streamwise and vertical velocity fluctuations for the baseline experiments.

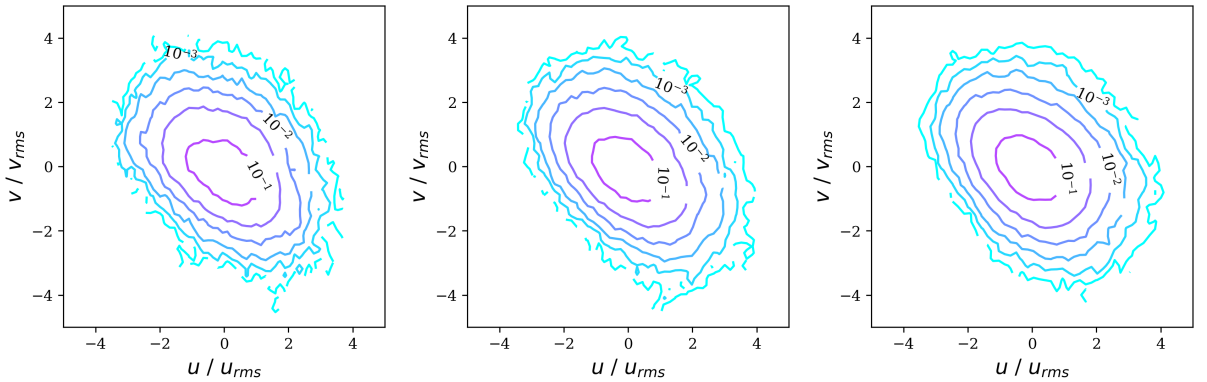

(a) y = 10 mm, U_∞ = 1.1 m/s (b) y = 25 mm, U_∞ = 2.0 m/s (c) y = 40 mm, U_∞ = 3.2 m/s

Figure 4.6: Characteristic contour plots of joint PDFs of the streamwise and vertical velocity fluctuations for the baseline experiments.

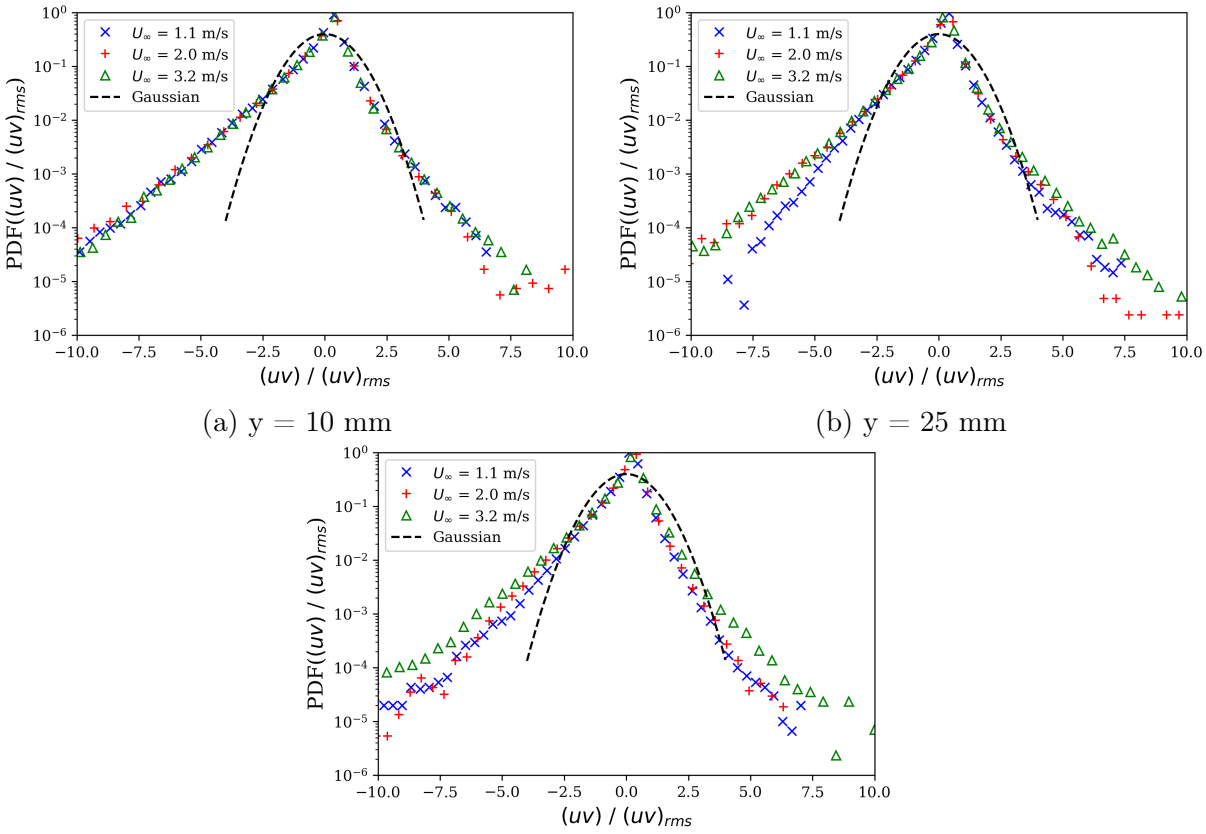

(a) y = 10 mm

(b) y = 25 mm

(c) y = 40 mm

Figure 4.7: Non-dimensional PDFs of uv for the baseline cases.

4.2 Statistically Stationary Turbulent Velocity Field Over Melting Ice

Having characterized the baseline flow in the absence of ice for the nine cases in the test envelope, the results could be compared to those of the experiments over melting ice to understand the effect of the ice surface on the velocity statistics. However, given that the warming and melting of an ice patch is a (thermally) unsteady problem, it is reasonable to expect that the statistics of both velocity and temperature measured in the turbulent boundary layer over melting ice would undergo a transient evolution. The transient evolution of the melting ice is discussed in detail in section 4.3; however, it was found that the velocity field statistics did not change significantly in time throughout the experiments. This is illustrated by plotting the local time-averages of the mean

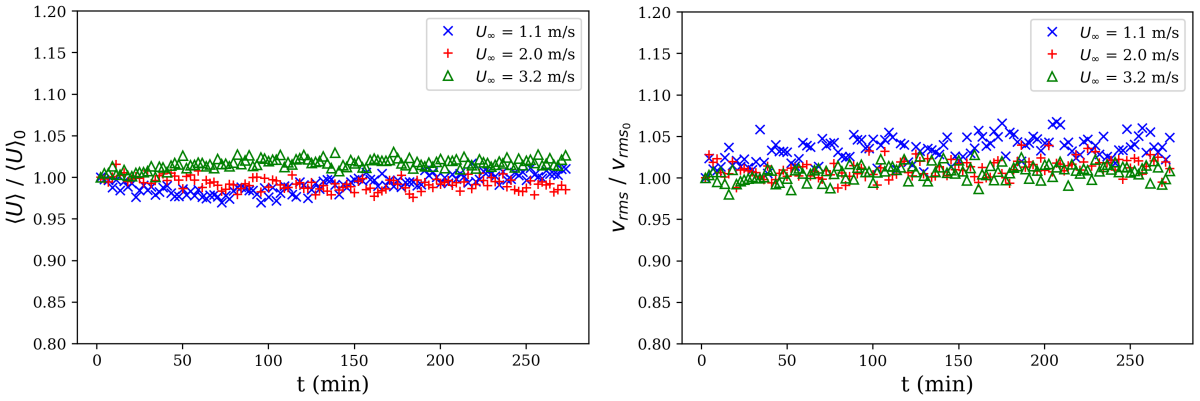

(a) Mean streamwise velocity

(b) RMS vertical velocity

Figure 4.8: Evolution of local time-averages of velocity quantities at y=10 mm. Local averages were calculated in subsets of 8×10^5 samples, lasting approximately 137 s each.

streamwise and RMS vertical velocities as a function of time in Figure 4.8 for the lowest measurement height (which will be the most influenced by changes in temperature). The local averages are non-dimensionalized by their initial value (i.e. from the first averaging period) to visualize the relative changes. It can be seen that the quantities do not change appreciably throughout the course of the experiments, and as such the velocity field measured over melting ice for the experiments of the present work can be reasonably considered statistically stationary.

Having demonstrated the statistical stationarity of the velocity field over melting ice, the preceding analysis for the baseline cases can be repeated for the experiments over ice. In addition to velocity-related quantities, the turbulent Richardson number (Ri_t) was used to quantify the level of stratification in the flow. While the statistics of velocity were found to be steady, temperature-related quantities (including the Richardson number) were not. Even though the Richardson number was not completely stationary, it was found to be generally constant in time after an initial period of rapid change. This is further discussed in section 4.3. However, for the purpose of assessing the potential effects of stable stratification on the turbulent velocity field over melting ice when compared to the baseline cases, the Richardson numbers is nevertheless treated as a constant.

Velocity statistics measured over melting ice are therefore presented in Table 4.3. These are then quantitatively compared to the baseline values in Table 4.4, where the

y (mm)	10			25			40		
U_∞ (m/s)	1.1	2.0	3.2	1.1	2.0	3.2	1.1	2.0	3.2
$\langle U \rangle$ (m/s)	0.84	1.47	2.27	0.86	1.63	2.7	1.07	1.76	2.86
$T_\infty - \langle T \rangle$ (°C)	2.5	2.5	2.9	0.6	1.4	1.3	1.0	1.2	1.1
u_{rms} (m/s)	0.111	0.227	0.333	0.095	0.196	0.321	0.079	0.162	0.288
v_{rms} (m/s)	0.036	0.092	0.155	0.038	0.095	0.17	0.044	0.095	0.176
$-\langle uv \rangle$ $(m/s)^2$	0.0014	0.0078	0.0183	0.0015	0.0076	0.0186	0.001	0.0053	0.0168
ϵ (m^2/s^3)	0.097	0.239	0.682	0.136	0.212	0.322	0.083	0.094	0.21
ℓ (m)	0.05	0.07	0.09	0.06	0.09	0.11	0.09	0.10	0.12
λ (mm)	5.3	6.9	6.0	3.9	6.4	8.5	4.1	7.9	9.4
η (mm)	0.43	0.34	0.26	0.40	0.35	0.32	0.45	0.43	0.35
$-\rho_{uv}$	0.35	0.37	0.35	0.42	0.40	0.34	0.29	0.35	0.33
Re_ℓ	396	1132	2050	395	1147	2452	480	1093	2383
Re_λ	40	106	135	24	84	182	22	86	182
Re_δ	5600	10000	16200	5500	10000	16000	5500	10100	16100
Ri_b	0.008	0.003	0.001	0.021	0.006	0.002	0.021	0.008	0.003
Ri_t	115	37	19	67	20	11	64	16	7

Table 4.3: Velocity statistics measured over melting ice.

y (mm)	10			25			40		
U_∞ (m/s)	1.1	2.0	3.2	1.1	2.0	3.2	1.1	2.0	3.2
$\Delta \langle U \rangle$ (%)	-5.0	-6.9	-9.0	-12.7	-7.3	-2.4	3.4	-5.1	-2.1
Δu_{rms} (%)	1.2	14.6	2.5	6.8	10.7	5.9	-0.7	-0.1	-1.7
Δv_{rms} (%)	-16.8	-2.9	-6.5	-19.5	-3.7	-1.7	-5.2	-5.0	-2.8
$\Delta \langle uv \rangle$ (%)	-23.6	-2.3	-20.0	-5.8	6.6	-6.6	-15.3	-13.9	-6.9
$\Delta\epsilon$ (%)	-16.9	36.8	33.4	32.5	78.1	14.9	-15.1	-3.9	2.4
$\Delta\ell$ (%)	-25.0	-7.3	-8.9	-22.1	-3.1	-4.8	28.9	-8.7	-5.1
$\Delta\lambda$ (%)	10.1	-2.4	-11.8	-7.3	-17.3	-1.3	7.6	1.5	-3.1
$\Delta\eta$ (%)	3.4	-8.2	-7.9	-6.9	-13.9	-3.6	3.9	0.3	-1.0
$\Delta\rho_{uv}$ (%)	-9.3	-12.2	-16.6	9.7	-0.1	-10.3	-10.1	-9.3	-2.6
ΔR_ℓ (%)	-22.8	7.2	-5.4	-16.7	8.0	1.2	28.6	-8.0	-6.2
ΔR_λ (%)	13.4	12.9	-8.4	-0.9	-7.8	4.8	7.3	2.3	-4.2

Table 4.4: Percent change of velocity statistics in experiments over ice relative to baseline cases.

difference between the quantities measured over ice and the baseline cases are expressed as a percentage of the baseline value.

The most significant changes are observed for the experiments closest to the surface (at y =10 mm), as expected, given that this is where the thermal gradient, which induces stratification effects, will be strongest. For all of the experiments, the dissipation rate (ϵ) and integral length scale (ℓ) experienced the most significant changes. However, their changes are not analyzed in further detail in the present work, since they do not play

as significant of a role in understanding stratification as the statistics of the velocity field itself. Therefore, the percent change in the second-order statistics (variance and co-variance) will be the focus of the comparison between the results.

The present results can be compared to prior research relating to stably stratified boundary layer flows (such as Arya, 1975; Ohya et al., 1997; Williams et al., 2017), whereby it is expected that the second-order velocity quantities (variance and co-variance) will decrease with increasing Richardson number, due to the effects of stable stratification. To visualize these changes, the percent changes in the streamwise and vertical velocity variance relative to the baseline cases, as well as that of the co-variance (i.e. the Reynolds stress) are plotted as a function of the turbulent Richardson number in Figure 4.9. As expected, there appears to be a general decrease in the vertical velocity variance with increasing Richardson number, as buoyancy forces extract turbulent kinetic energy from the vertical fluctuations, thereby reducing the Reynolds stress (Arya, 1975).

However, there is a clearly observable increase in the streamwise velocity variance in the experiments over ice, which does not appear to be clearly related to the turbulent Richardson number. This result is unexpected, since profiles of velocity statistics measured in stably stratified boundary layers show a decrease in all velocity components with increasing stratification (e.g. Ohya et al., 1997). Physically, this may be the result of the liquid film on the surface of the ice, changing the boundary condition at the air-water interface. Furthermore, the observed increase in streamwise velocity variance was not found to be correlated with any of the quantities calculated in Table 4.3 (not shown).

Arya (1975) and Williams et al. (2017) state that the suppression of the vertical fluctuations by buoyancy should in turn decrease the Reynolds stress. This is also observed in the present work. However, they also both state that the interaction between the Reynolds stress and mean velocity gradient should decrease the streamwise velocity variance. Given the limited number of measurement heights in the scope of the present work, the velocity gradient could not be accurately calculated and therefore related to the change in the streamwise velocity variance.

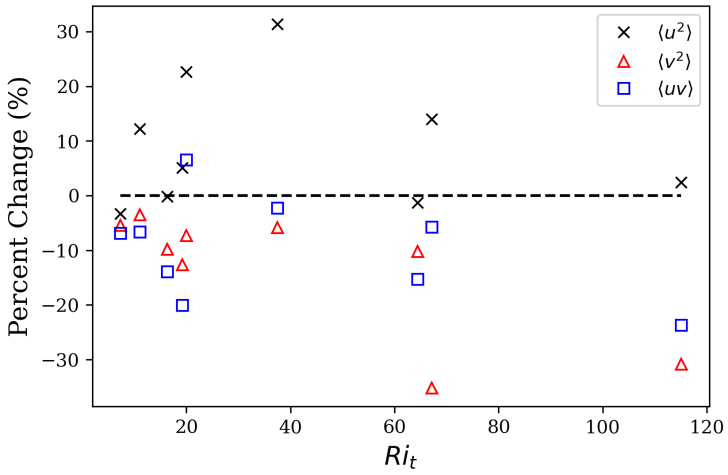

Figure 4.9: Percent change of second-order velocity quantities as a function of turbulent Richardson number.

It was found that the average increase in streamwise velocity variance was approximately 6%, whereas the average decrease in vertical velocity variance was approximately 13%. The average decrease in the Reynolds stress was approximately 11%. When comparing the turbulent kinetic energy (TKE) inside the x-y measurement plane, where:

$$TKE_{xy} \equiv \left\langle u^2 \right\rangle + \left\langle v^2 \right\rangle, \tag{4.7}$$

the change between the baseline cases and experiments over ice was negligible (less than 2%). The magnitude of the decrease in vertical velocity variance was offset by the increase in streamwise velocity variance such that the total TKE measured in the x-y plane over melting ice was nearly unchanged relative to the baseline cases. Another important statistic, the anisotropy ratio, defined as:

$$\phi \equiv \frac{v_{rms}}{u_{rms}}, \tag{4.8}$$

has been demonstrated to be relatively insensitive to the effects of stratification below the critical Richardson number (Williams et al., 2017). The documented insensitivity of the anisotropy ratio in the literature is attributed to decreases in the streamwise velocity variance by the lowered Reynolds stresses that are proportional to those of the vertical

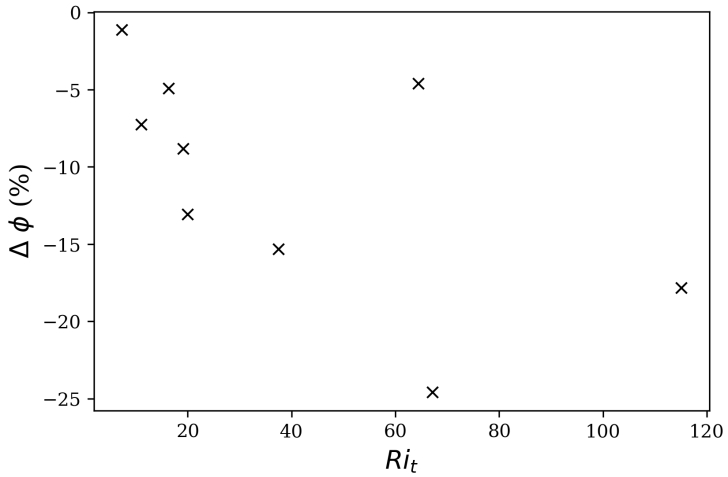

Figure 4.10: Percent change in anisotropy ratio as a function of turbulent Richardson number.

velocity variance due to buoyancy, such that ϕ is unchanged (Arya, 1975). However, in the present work, the change in the anisotropy ratio between the experiments over ice and the baseline cases is shown to generally increase with increasing turbulent Richardson number as depicted in Figure 4.10. Studies of the downstream evolution of grid-generated stratified turbulence in have found a relationship between the anisotropy and Richardson number (Piccirillo & van Atta, 1997; Yoon & Warhaft, 1990), however such has an effect has not been observed in the boundary layer over solid (i.e. non-melting) surfaces, and may therefore be related to the change in the nature of the boundary condition at the surface when it melts.

Since the stratification as quantified by the *bulk* Richardson number (shown in Table 4.3) is relatively weak when compared to the critical value of 0.25 (Ohya et al., 1997), it is possible that the observed changes in second-order statistics measured over melting ice are not directly caused by the stratification, but rather a physical phenomena related to the phase-change at the ice's surface. This physical phenomena could be an aerodynamic effect related to the Reynolds number, or a stratification effect related to the Richardson number, but the relationship between these two quantities makes the distinction unclear. Attempting to explain the observed differences between the baseline cases and experiments measured over ice, the following hypothesis is offered.

As the surface changes from solid ice to liquid water, a thin layer of water forms

atop the ice. The reduced friction between air and water (two fluids) compared to that between air and ice may cause additional streamwise velocity fluctuations in the turbulent boundary layer, thereby explaining the increased velocity variance which was not clearly related to Richardson number. Furthermore, since the velocity gradient may be lower, the wall shear stress will be lower, generating less Reynolds stress. The decrease in vertical velocity variance may then be attributed to either the effects of stratification through the classical mechanism (Tennekes & Lumley, 1972), or to the reduced wall shear stress.

The complex nature of this problem makes the evaluation of this hypothesis challenging, as well as the comparison to prior work. As discussed, the velocity statistics measured herein above melting ice differ from prior results in stably stratified flows over solid surfaces, potentially due to the thin film of liquid water on the surface. Nevertheless, it is beneficial to examine how the present results compare to the literature in adjacent fields of study.

Consider the literature regarding the atmospheric boundary layer over sea ice. While these atmospheric studies do not usually resolve smaller scales of the turbulence (Bou-Zeid, Higgins, Huwald, Meneveau, & Parlange, 2010), differences in the atmospheric flow observed over ice and water can provide insight into the present results. Brümmer, Busack, Hoeber, and Kruspe (1994) observed stronger "air-mass transformations" over water than over sea ice, which they attributed to differences in the surface heat conduction between solid ice and liquid water. The numerical model of Kantha and Mellor (1989) indicates greater surface shear stress observed over ice than water. This was in agreement with the field observations of Overland (1985), who found that the drag coefficient (C_D), related to the surface shear stress, was greater for regions with a larger fraction of ice coverage in mixed (i.e. marginal) sea-ice zones. The increased shear stress in turn generated larger momentum fluxes above ice than water.

Although it is difficult to compare the aforementioned results to the present ones, one notes that the thin layer of liquid water growing atop the surface of the ice is hypothesized to be responsible for the lower Reynolds stresses observed in the experiments over ice

compared to those of the baseline cases. Presumably this layer should also exist over melting ice in the atmospheric boundary layer, however, it is likely insignificant when considering the much larger scales of relevance in atmospheric flows when compared to laboratory flows, combined with the fact that the ice water may run off from the surface in such flows.

This being said, it may be relevant to also consider the prior work pertaining to the smaller-scale turbulence observed in the boundary layer of a gaseous flow over a thin liquid film. Cohen and Hanratty (1965) performed experiments in which two- and three-dimensional surface waves were observed in a liquid film with a thickness between 1.8 and 7.6 mm underneath a gaseous flow of sufficiently large velocity. Kendall (1970) found that the existence of surface waves will greatly influence the structure of the turbulence above a wavy (solid) surface. In the work of Sullivan, McWilliams, and Moeng (2000), the momentum flux above a wavy surface was altered by up to 40%, wherein faster surface waves decreased the skin friction coefficient at the surface. In the presence of stable stratification, the "effective" surface wave speed is increased, further decreasing the skin friction coefficient (Sullivan & McWilliams, 2002).

The required depth of the liquid layer required to observe a significant effect on the turbulent statistics of the boundary layer remains to be seen. It has been observed that even in the case of very thin films, the liquid layer can influence the stability of the boundary layer (Náraigh, Spelt, Matar, & Zaki, 2011), or potentially even lead to localized separation (Pelekasis & Tsamopoulos, 2001). The insignificance of the liquid layer depth with respect to the existence of surface waves that influence the boundary layer is somewhat affirmed in the present work, since the statistics of velocity were not found to vary significantly in time while a water layer formed atop the ice throughout the course of the experiments.

It is clear that the addition of the phase-changing ice surface adds further complexity to the problem of investigating stably stratified boundary layer flows over melting ice, as there now may be effects that are attributable to neither the Reynolds nor Richardson

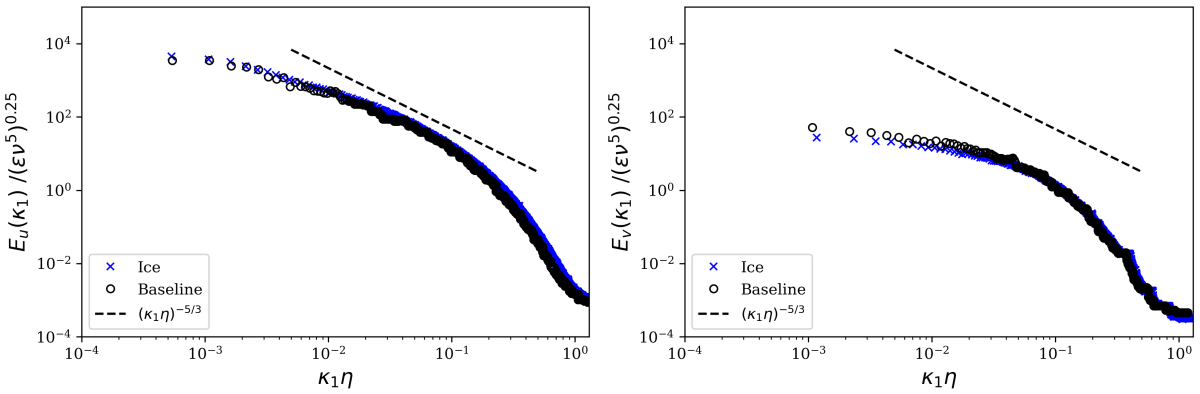

(a) y =10 mm, U_∞ =2.0 m/s (b) y =10 mm, U_∞ =1.1 m/s

Figure 4.11: Comparison of the baseline non-dimensional wavenumber spectra to those measured over melting ice for the streamwise (a) and vertical (b) velocity fluctuations.

numbers. Studies have already attempted to separate the effects of these two parameters (e.g. Williams et al., 2017), however the addition of the phase changing surface in the present work makes it extremely difficult to attribute the changes between the velocity field over melting ice and that of a neutral boundary layer to either Reynolds number, Richardson number, or surface phase effects.

Nevertheless, it remains of interest to further compare the results obtained over melting ice to those of the baseline cases using the PDFs and spectra. For all of the experiments herein, it was found that the non-dimensional wavenumber spectra measured over melting ice did not exhibit a significant change when compared to the baseline cases. To illustrate this observation, a comparison between the streamwise and vertical velocity spectra for the cases with the maximum percent difference (as shown in Table 4.4) is presented in Figure 4.11. These are the $U_\infty = 2.0$ and $U_\infty = 1.1$ cases for the u and v spectra, respectively, both at $y = 10$ mm. Even for these cases of relatively large change in velocity variance, the (non-dimensional) spectra show little-to-no difference between the baseline cases and experiments over ice, implying that the turbulent cascade in these experiments is unchanged by the presence of the ice.

With the observed spectral similarity between the baseline cases and experiments over ice, it is also useful to evaluate how the presence of the ice changes the PDFs of u and v. Figure 4.12 shows the normalized PDFs for the streamwise and vertical velocity

fluctuations, whereby the reference for comparison to the baseline cases is the Gaussian distribution, given their nearly Gaussian behaviour. Such behaviour is observed once again for the experiments over melting ice. However, the greatest deviation from Gaussian behaviour is observed nearest the ice surface (y=10 mm), where the temperature gradient is strongest. Compared to the baseline cases, the deviation from Gaussian behaviour occurs in the tails of the vertical velocity PDFs and is much stronger than that of the streamwise velocity PDFs. Furthermore, while the baseline PDFs of the streamwise velocity at y=10 mm showed no significant deviation from a Gaussian PDF, there is an observable difference at the tails in Figure 4.12 (a). As the height is increased, this deviation disappears, indicating a decreased effect of the temperature field on the streamwise velocity fluctuations. This effect of the ice on the PDFs of the vertical velocity fluctuations does not decrease with height as rapidly as for the streamwise velocity fluctuations. This is illustrated by comparing the PDFs for the streamwise and vertical velocity fluctuations at y=25 mm (Figure 4.12 (c) and (d)). At this height, the tails of the streamwise velocity PDFs retain their Gaussian behaviour as observed in the baseline cases. By contrast, the tails of the vertical velocity PDFs at this height are super-Gaussian. At y=40 mm, both PDFs of streamwise and vertical velocity appear nearly Gaussian, indicating negligible influence of the ice surface on the velocity PDFs at this height.

Having compared the single-velocity-component spectra and PDFs for both velocity components to the respective baseline cases, combined velocity statistics are now investigated. Since no significant difference was observed between the non-dimensional wavenumber spectra for the two velocity components, despite an increase in the streamwise velocity variance and a decrease in the vertical velocity variance, it was expected that the coherence spectra of the experiments over melting ice might exhibit the same similarity to the baseline cases shown by the single-velocity-component spectra. However, this was not found to be the case. Nearest the surface (at y =10 mm), the coherence spectra exhibit a decrease relative to the baseline cases that grows with Reynolds number, as shown in Figure 4.13.

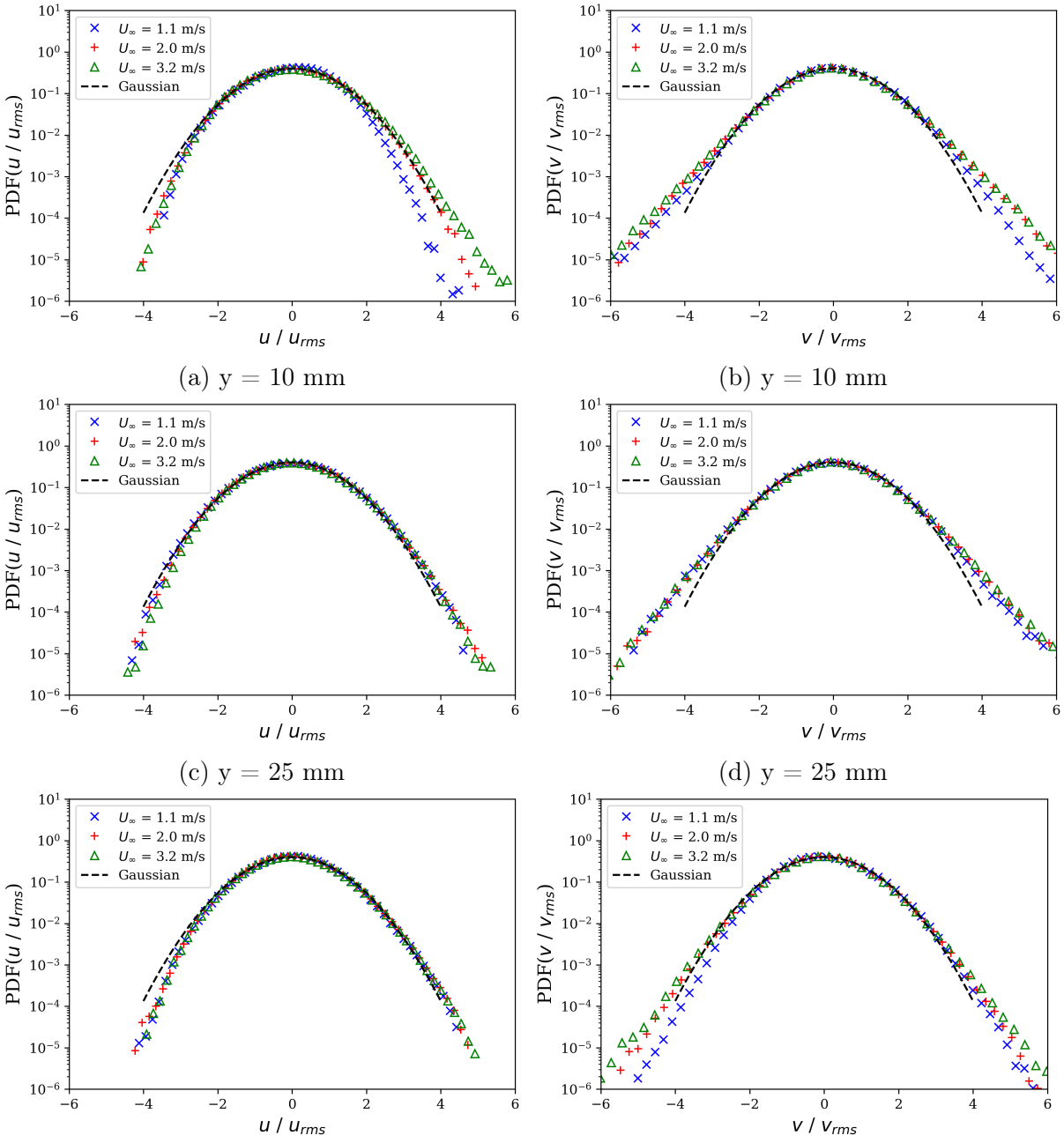

(a) y = 10 mm (b) y = 10 mm

(c) y = 25 mm (d) y = 25 mm

(e) y = 40 mm (f) y = 40 mm

Figure 4.12: Non-dimensional PDFs of streamwise (a,c,e) and vertical (b,d,f) velocity fluctuations.

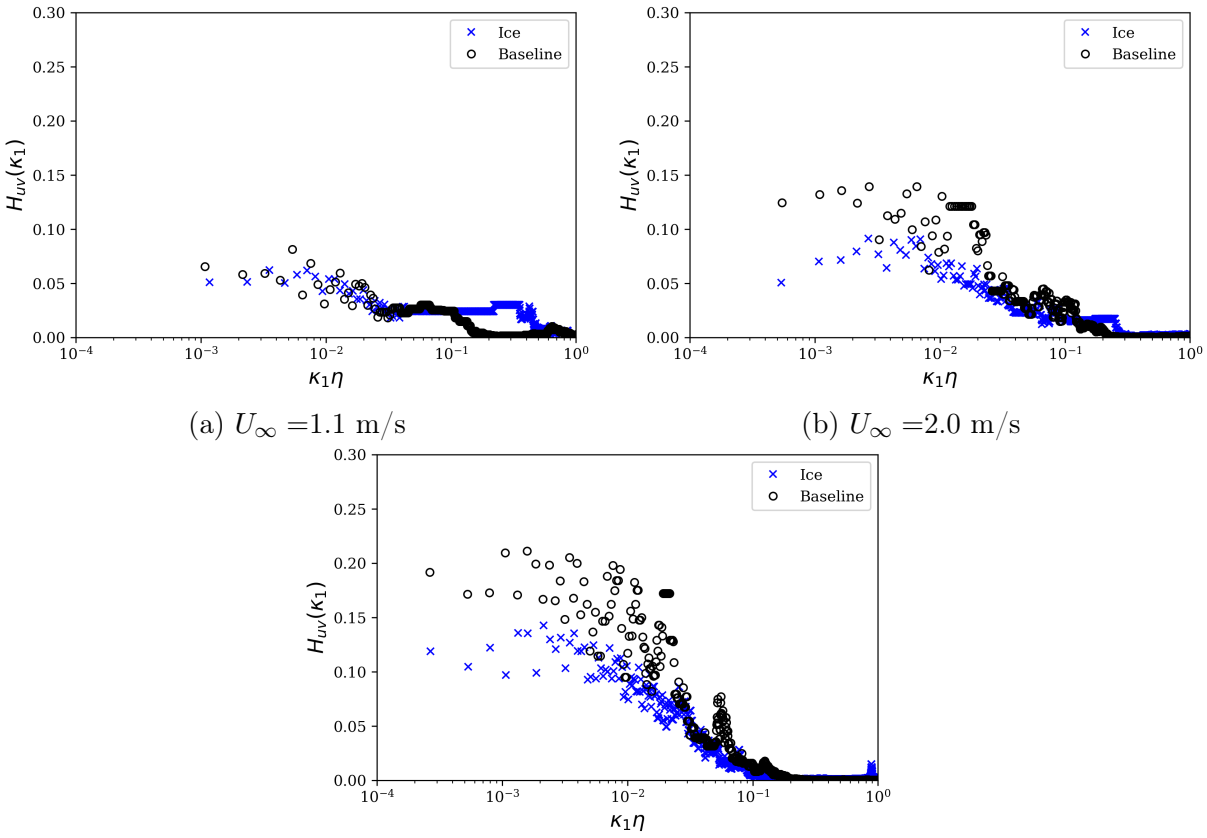

(a) U_∞ =1.1 m/s

(b) U_∞ =2.0 m/s

(c) U_∞ =3.2 m/s

Figure 4.13: Comparison of the baseline coherence spectra to those measured over melting ice at y =10 mm.

For the lowest free-stream velocity (i.e. when the Richardson number is largest), the coherence over melting ice shows the most similarity to the baseline case. The difference increases as the Richardson number decreases, such that it does not seem likely that the decrease in coherence is caused by the effects of stratification. Since the coherence is directly related to the Reynolds stress, this may lend credibility to the previously discussed hypothesis in which the decrease in Reynolds stress is not attributed to the effects of stratification. For the other two heights, there was no observed difference between the coherence of the experiments over ice and the baseline cases for any of the free-stream velocities investigated. The effects of the ice on the coherence appear to be limited to higher Reynolds numbers nearest to the surface, when the shear is highest.

It is then worth comparing the joint PDFs of u and v for two cases with the same free-stream velocity, but measured at different heights, to understand how the stronger

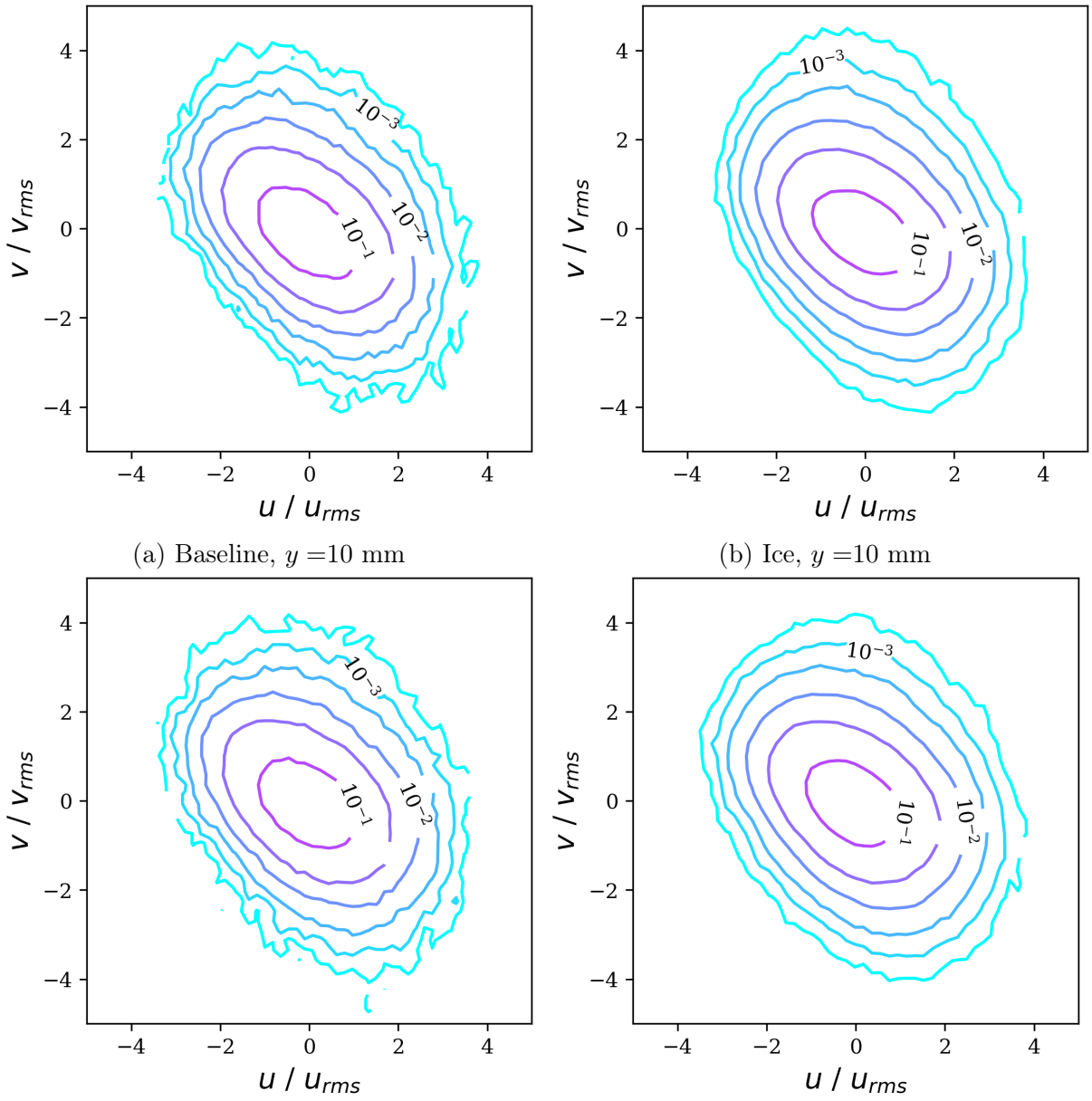

(a) Baseline, y =10 mm

(b) Ice, y =10 mm

(c) Baseline, y =25 mm

(d) Ice, y =25 mm

Figure 4.14: Comparison of the contours of joint PDFs for the baseline cases (a,c) to those measured over ice (b,d) for U_∞ =3.2 m/s.

reduction in Reynolds stress (i.e. coherence) observed near the wall vanishes as the height is increased. To this end, the joint PDFs are plotted for two heights at U_∞=3.2 m/s, beside the baseline joint PDFs for comparison, in Figure 4.14. Unlike the PDFs of u and v, in which differences between the baseline and experiments over ice were visible in the tails, the joint PDFs appear largely similar.

Lastly, the PDFs of uv over melting ice are considered. They are presented in Figure

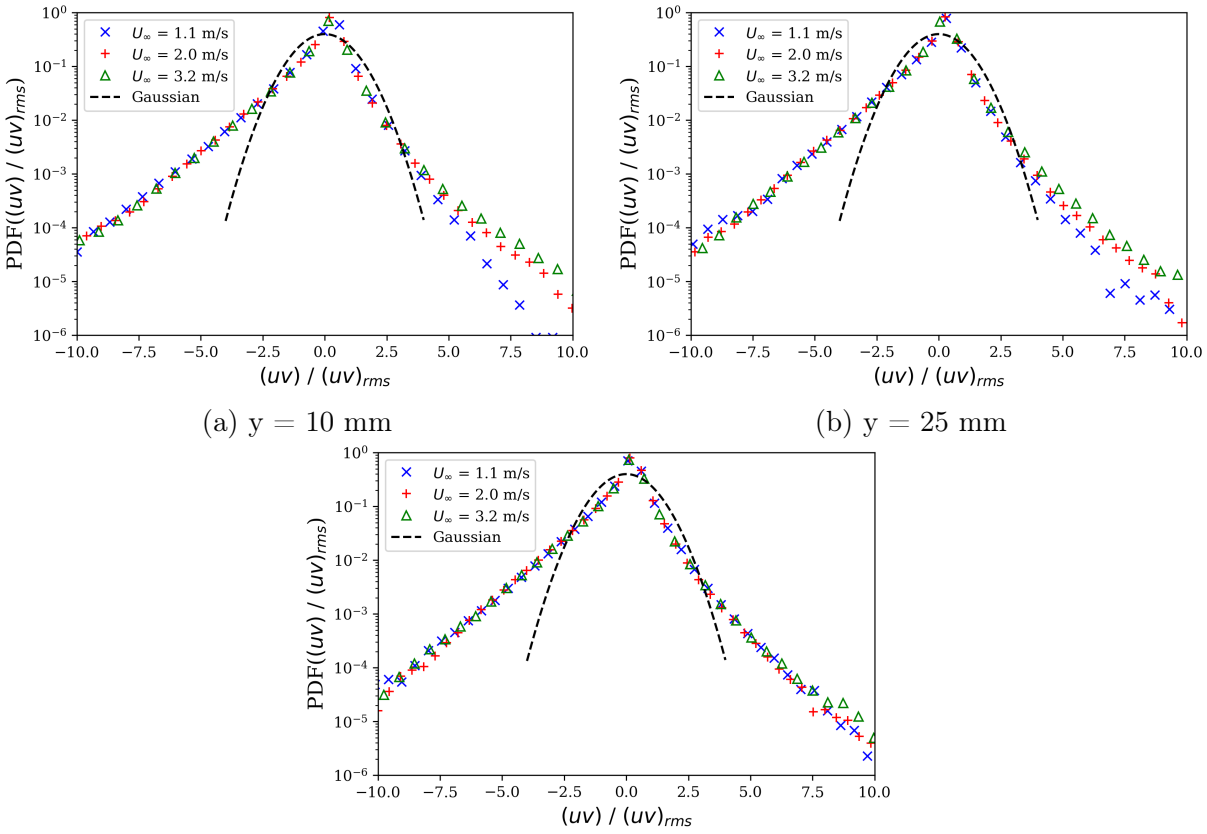

(a) y = 10 mm

(b) y = 25 mm

(c) y = 40 mm

Figure 4.15: Non-dimensional PDFs of uv measured over melting ice.

4.15, and have similar shapes to the baseline cases shown in Figure 4.7. However, the behaviour at the tails is opposite to that of the baseline cases – the PDFs of uv over melting ice show better collapse at all speeds farther from the wall, and show the most sensitivity to free-stream velocity nearest to the wall. The differences with free-stream velocity appear to be restricted to the positive tail of the PDF, whereas the negative tail shows good collapse for all nine cases. Given that that deviations only exist in the region where $(uv) > 5(uv)_{rms}$, the significance of these differences between the baseline cases and experiments over ice is likely small.

Overall, a comparison of the velocity statistics was made between the experiments over melting ice and those measured in the empty tunnel. Although the stratification was relatively weak, there was still a noticeable impact on the measured statistics of turbulent velocity over melting ice. Consistent with the literature regarding stably stratified boundary layers over solid surfaces, decreases in the vertical velocity variance ($\langle v^2 \rangle$) and

Reynolds stresses ($\langle uv \rangle$) were observed. However, there was also an observed increase in the streamwise velocity variance ($\langle u^2 \rangle$), which has not been noted in previous studies of stratified wall-bounded turbulence. These observed differences may not be attributable to the effects of stratification, but rather the presence of a phase-changing boundary. Spectra of the velocity fluctuations did not show a significant difference between those measured over ice and the baseline cases, however, there was an observed deviation from Gaussian behaviour in the tails of the vertical velocity PDFs in the experiments over ice. Coherence spectra of uv showed a decrease in magnitude relative to the baseline cases with increasing Reynolds number only for the measurement height nearest the wall (corresponding to $y/\delta = 0.13$), and not for the other two measurement heights ($y/\delta = 0.33$ and 0.53). However, joint PDFs of u and v, and PDFs of uv showed no appreciable difference between the experiments over ice and those inside the empty tunnel.

4.3 Transient Evolution of Melting Ice

In this section, the transient evolutions of the melting ice surface and the turbulent flow over it are investigated. In the present work, the glacier model was initially at a sub-zero temperature (approximately $-10°$C), and was partially melted during the course of the experiments due to the convective heat transfer from the turbulent air flow in the wind tunnel. The evolution of the glacier model, and the temperature-related statistics measured in the turbulent boundary layer above it, are discussed below.

4.3.1 Evolution of the Glacier Model

During the experiments, the ice surface transitioned through three distinct "phases" of the melt process, which are described herein. Photographs of the ice surface during each phase are presented in Figure 4.16.

At the beginning of each experiment, the sub-surface temperature was around $-10°$C. When the wind tunnel was turned on, the ice would begin to warm due to the convective

heat transfer from the room temperature air blowing over it, and a thin layer of frost would then form on the ice surface. The sub-surface temperature would rapidly increase during this time. This is referred to as the warming phase, shown in Figure 4.16 (a), wherein the surface layer of the glacier model in contact with the airflow was solid ice.

Once the ice surface reached 0°C, it would begin to melt. The layer of frost on the surface would begin to recede, starting from the outside edges of the ice surface and moving towards the centre, as seen in Figure 4.16 (b). This process would also remove any minor surface topographical or roughness features. Since the wind tunnel flow in these experiments is homogeneous (Cohen, 2019; Mydlarski & Warhaft, 1996), initial melting from the outside edges may be attributed to additional conductive heat transfer from the side-walls of the ice tray, increasing the total heat flux near the edges. During this time, it can be assumed that the surface temperature of the ice was constant at 0°C, given that the temperature of a phase-changing substance is constant (Bergman, Bergman, Incropera, DeWitt, & Lavine, 2011). The sub-surface temperature would remain constant during this time, slightly below 0°C since it was embedded slightly below the ice's surface. This phase is referred to as the melting phase, wherein the surface layer of the glacier model in contact with the airflow was a thin layer of water sitting atop solid ice.

As the ice continued to melt, the water layer on top of the ice would continue to grow, since it was not drained during the course of the experiments (see section 3.2.2). Eventually, the water layer would become thick enough to have an internal temperature

(a) Warming phase (b) Melting phase (c) Pooling phase

Figure 4.16: Ice melting process during experiments.

gradient of its own, acting as a heat sink atop the ice surface. This is referred to as the pooling phase. During the pooling phase, the surface was completely smooth due to the surface tension of the water (visible via the reflections on the surface in Figure 4.16 (c)), but the temperature at the air-water interface was unknown. Measurement of the true surface temperature of the liquid was not possible given the standard type E thermocouple used in this work, and given the challenges associated with assessing the temperature jump at the air-water interface (Gatapova et al., 2017). The exact condition necessary for transition between the melting and pooling phases is somewhat arbitrary without knowledge of the surface temperature, but may be observed by an increase in the sub-surface temperature measured by the embedded thermocouple, at which point the water layer depth was approximately 5 mm. By the end of the experiments, the thickness of the water layer was never more than 10 mm.

The point in time at which the ice would transition between these phases was dependent on the free-stream velocity, which controlled the melt rate of the glacier model. An appropriate time scale for the bulk melt rate (τ_m) can be determined using an approximate energy balance between the melt heat flux (Q_M) and convective heat flux (Q_H). The melt heat flux can be expressed as:

$$Q_M = \frac{mL_f}{\tau_m A}, \tag{4.9}$$

where m is the mass of the melting ice, L_f is the specific latent heat of fusion, and A is the surface area in contact with the turbulent airflow. For the rectangular prism-shaped block of ice used in herein, the mass can be re-expressed as $\rho_{ice} \times A \times d$, where ρ_{ice} is the density of the ice and d is the depth of ice. The bulk convective heat flux from the air to the ice surface is given by:

$$Q_H = h\left(T_s - T_\infty\right), \tag{4.10}$$

where h is the convective heat transfer coefficient, related to the Nusselt number through equation (3.2). For convective heat transfer to an isothermal flat plate (a reasonable

approximation of the glacier model), the characteristic length scale in equation (3.2) is given by the streamwise position (x). In this series of wind tunnel experiments, there is an unheated starting length (ζ) over which the velocity boundary layer grows before reaching the ice surface. In this case, semi-empirical correlations from the literature (Bergman et al., 2011) allow the Nusselt number to be estimated as:

$$Nu_\zeta = \frac{0.0296(Re_x^{0.8})Pr^{0.33}}{\left[1-\left(\frac{\zeta}{x}\right)^{0.9}\right]^{1/9}}, \tag{4.11}$$

where x is the total downstream distance from the grid to the measurement probe. Combining equations (4.9), (4.10), and (4.11) the melt time scale can be found as:

$$\tau_m = \frac{\rho_{ice} L_f d}{T_s - T_\infty}\left(\frac{x}{k_f}\right)\left(\frac{\left[1-\left(\frac{\zeta}{x}\right)^{0.9}\right]^{1/9}}{0.0296(Re_x^{0.8})Pr^{0.33}}\right). \tag{4.12}$$

The exact value of the characteristic depth (d) is somewhat arbitrary, since most of the terms in equation (4.12) apart from Re_x are constant for all of the experiments performed herein. In this case, a characteristic ice depth of 1 mm was selected. Given this choice, the melt time scales τ_m were found to be approximately 6.1×10^4, 3.8×10^4, and 2.6×10^4 s for free-stream velocities of 1.1, 2.0, and 3.2 m/s, respectively. Using this melt time scale, the evolution of the sub-surface temperature from the embedded thermocouple was plotted below as a function of the non-dimensional run time (t/τ_m) in Figure 4.17. The sub-surface temperature is herein referred to as T_{ss}, serving as the closest possible estimation of the true surface temperature in this work.

Figure 4.17 shows that the melt time scale (τ_m) is a sensible one, since the plots of the sub-surface temperature collapse reasonably well when plotted as a function of non-dimensional time. The warming phase is observed in the region where T_{ss} is changing the most rapidly. The melting phase begins at approximately $0.06\tau_m$. The increase in temperature at approximately $0.2\tau_m$ corresponds the point in time at which pool of water atop the ice surface reaches the depth of the thermocouple (approximately 5 mm).

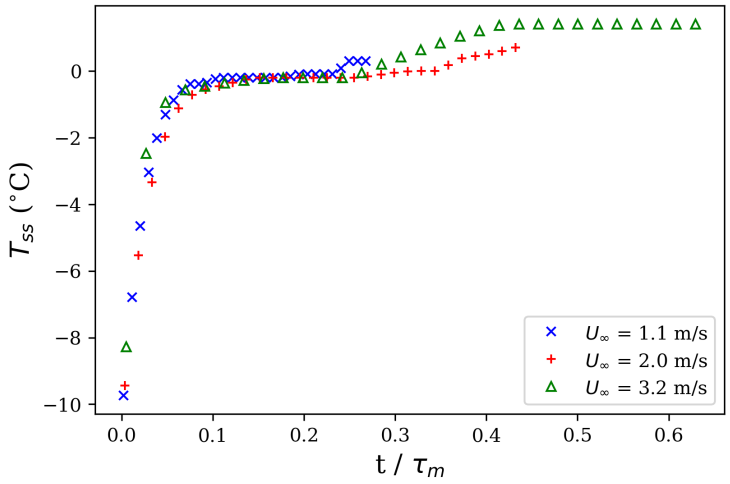

Figure 4.17: Evolution of ice sub-surface temperature in non-dimensional time.

4.3.2 Evolution of Temperature-Related Quantities Above Melting Ice

The surface temperature is a key parameter affecting the statistics of temperature and its related quantities in a thermal boundary layer. Therefore, the transient evolution of the surface temperature resulted in a transient evolution in the temperature and combined velocity-temperature statistics of the thermal boundary layer. To enable a discussion of the evolutions of these quantities as a function of time, local time-averages of these were evaluated in subsets of 8×10^5 samples (corresponding to a duration of 137 s).

Figure 4.18 shows the evolution of the locally-averaged RMS temperature (θ_{rms}) and turbulent heat flux ($\langle v\theta \rangle$), plotted as a function of the experimental run time for each of the measurement heights and speeds investigated in this work. The evolutions of the local averages of θ_{rms} and $\langle v\theta \rangle$ are both non-increasing functions of time. They show the most significant change in the first 100 minutes for all three speeds, but eventually reach a quasi-steady state (for $t > 200$ min), where changes the locally-averaged quantities in time become small (less than 5%).

The evolutions of the local averages θ_{rms} and $\langle v\theta \rangle$ can be used to understand the nature of the changing temperature field, and how it relates to the turbulent heat flux. The magnitude of the RMS temperature is greater for lower free-stream velocities, and towards

the surface. By contrast, the magnitude of the turbulent heat flux increases with surface proximity and free-stream velocity. These observations are not unexpected since the fluctuations of the temperature or velocity will be greatest when there is a higher vertical gradient of the corresponding mean quantity, which occurs closer to the surface (Tennekes & Lumley, 1972). At higher U_∞ (i.e., higher Reynolds numbers), increased turbulent kinetic energy results in better mixing, and decreased RMS temperature fluctuations. At lower U_∞, temperature fluctuations are less readily diffused such that there is a stronger thermal gradient.

The evolutions of the RMS temperature show greater similarity between the lower-speed runs (U_∞ =1.1 and 2.0 m/s), whereas the evolutions of the turbulent heat flux show greater similarity between the higher speed runs (U_∞ =2.0 and 3.2 m/s). For example, consider the dimensional heat flux for the higher speeds at y=10 and 25 mm (Figure 4.18 (b) and (d)), which show strong similarity despite the clear difference in θ_{rms} observed in (a) and (c).

The influence of free-stream velocity on the RMS temperature can also be observed from Figure 4.18. In general, as the height is increased, the sensitivity of θ_{rms} to the free-stream velocity is decreased, such that the difference in θ_{rms} between the fastest and slowest free-stream velocities is greatest at y=10 mm and smallest at y=40 mm. Additionally, the evolutions of the locally-averaged values of θ_{rms} show less variability with increasing height, as the temperature variance in the flow becomes weaker and fluctuations become more rare.

Recall that there was also stronger similarity for the higher speed runs in the spectra of the turbulent velocity field. Due to this observed similarity, and since the turbulent heat flux is larger when the velocity variance is larger, it can be concluded that the turbulent exchange of heat is dominated by the velocity field despite the strong thermal gradient. This finding is consistent with real-world glacier studies, in which turbulent heat fluxes were found to be strongly velocity-dependent despite strong stable stratification (Litt et al., 2015; Oerlemans & Grisogono, 2002), and is typical for weakly stable flows, which are

more dependent upon the Reynolds number than the Richardson number (Ohya et al., 1997).

It is also worth discussing the turbulent heat flux for the $y = 40$ mm, $U_\infty = 1.1$ m/s case, shown in blue on Figure 4.18 (f), in which the sign of the turbulent heat flux becomes positive at large times, implying a counter-gradient heat flux. While these have previously been observed in stratified turbulent flows (e.g. Yoon and Warhaft (1990)), they typically occur only in the presence of very strong stable stratification. In the present (weakly stratified) work, strong conclusions may not be warranted for this specific run, for which the values are low enough in magnitude to be within the uncertainty of the measurements.

To further analyze the statistics of temperature over melting ice, the RMS temperature and turbulent heat flux were plotted non-dimensionally by normalizing the locally averaged values evaluated at time t by their value at time t_0. The non-dimensional evolutions of the local averages are plotted as a function of the non-dimensional time (using the melt time scale determined above) as shown in Figure 4.19.

The non-dimensional evolutions of the local RMS temperature and turbulent heat flux show that the nature of the decay of θ_{rms} and $\langle v\theta \rangle$ in time generally does not change as a function of U_∞. For the non-dimensional RMS temperature fluctuations measured at y=10 mm, the highest-speed run does not fully collapse with the lower speed runs, although the observed deviation from $0.1 < t/\tau_m < 0.3$ was temporary. A notable exception to the generally-observed collapse is the lowest-speed run in Figure 4.19 (f), which did not appear to achieve a quasi-steady state at all. However, as alluded to previously, the values of $\langle v\theta \rangle$ were smallest for this run out of all nine cases studied herein, and approached the uncertainty of the measurements.

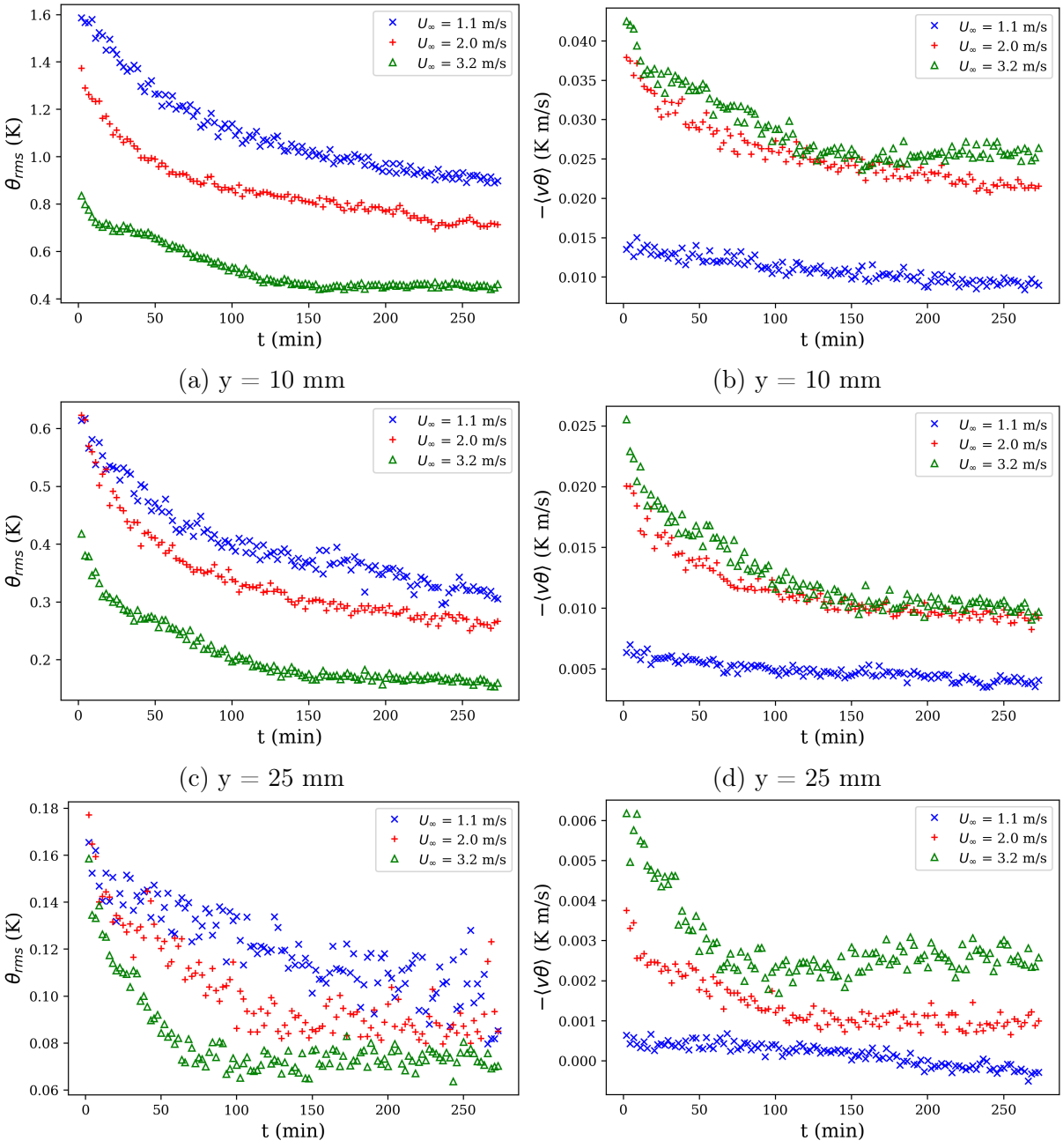

(a) y = 10 mm

(b) y = 10 mm

(c) y = 25 mm

(d) y = 25 mm

(e) y = 40 mm

(f) y = 40 mm

Figure 4.18: Evolution of locally-averaged RMS temperature (a,c,e) and turbulent heat flux (b,d,f) in time.

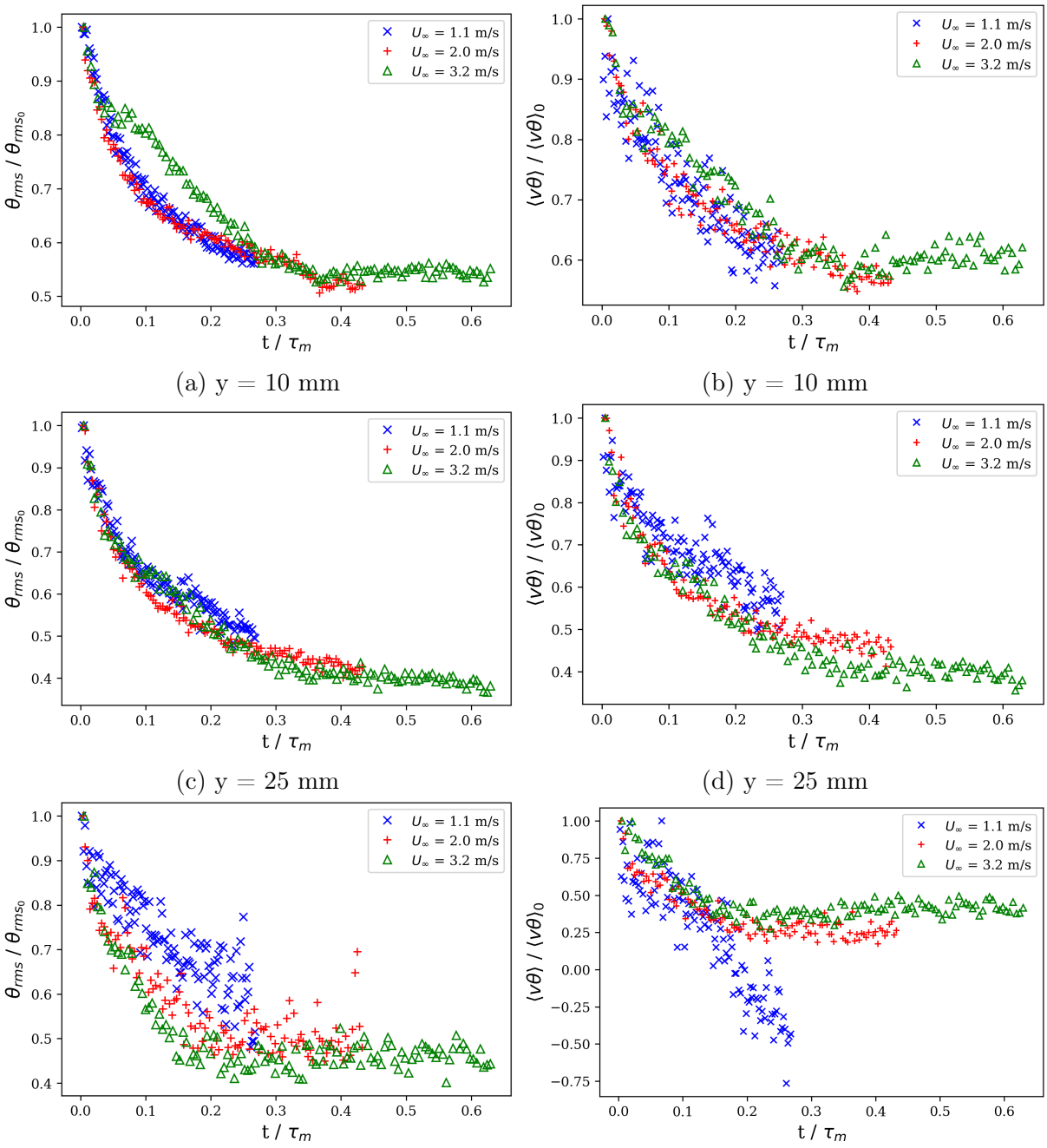

(a) y = 10 mm

(b) y = 10 mm

(c) y = 25 mm

(d) y = 25 mm

(e) y = 40 mm

(f) y = 40 mm

Figure 4.19: Evolution of locally-averaged non-dimensional RMS temperature (a,c,e) and turbulent heat flux (b,d,f) as a function of the non-dimensional experiment run time.

Interestingly, the RMS temperature and turbulent heat flux continue to decrease after $0.1\tau_m$, which corresponds the point in time after which changes in the sub-surface temperature were small (see Figure 4.17). The continued change in the temperature-related statistics measured in the turbulent boundary layer above melting ice may imply that the surface temperature is continually changing while the sub-surface temperature remains relatively constant, otherwise a plateau in the plots of θ_{rms} and $\langle v\theta \rangle$ would be observed in the region where $t > 0.1\tau_m$.

The magnitude of the decrease in θ_{rms} and $\langle v\theta \rangle$ when compared to their initial values was similar for the two larger heights (y= 25 and 40 mm), where they typically decreased to about 40% of the initial value. However, closer to the surface at y = 10 mm, the decrease was to approximately 55-60% of the initial value. Furthermore, the amount of time needed to reach the quasi-stationary state decreased with increasing height, from approximately $0.4\tau_m$ at y = 10 mm to $0.15\tau_m$ at y = 40 mm. In all cases, the period of time needed to reach this quasi-steady state was far beyond the beginning of the melting period (approximately $0.1\tau_m$). This amount of time required for quasi-stationarity may be a good estimation for the start of the pooling period, wherein the thickness of the surface water layer would be sufficient to act as a heat sink as it develops an internal temperature gradient, thereby reducing the rate of change of the surface temperature and corresponding temperature measurements in the boundary layer.

Other non-dimensionalizations for the RMS temperature and turbulent heat flux exist, and can be used to investigate how the changing quantities relate to the physics of the melting surface. The evolutions were mostly similar for different heights, such that only plots for the y =25 mm height are presented. In Figure 4.20 (a), the locally-averaged RMS temperature was scaled by the temperature differential $\langle T \rangle - T_{ss}$, where T_{ss} is used as a proxy measurement of the true surface temperature. In Figure 4.20 (b), the turbulent heat flux was scaled by the molecular heat flux (following the method of Yoon and Warhaft (1990)), to result in an effective, turbulent Nusselt number. In this case, if the temperature gradient $\beta = \frac{\partial T}{\partial y}$ was assumed to be linear, $\frac{\partial T}{\partial y} \approx \frac{\langle T \rangle - T_s}{y}$ (Fitzpatrick

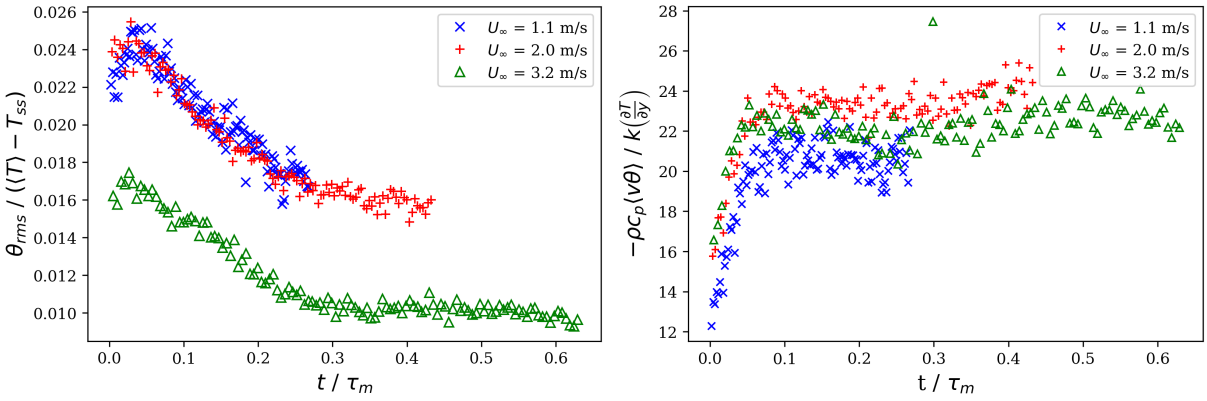

(a) RMS temperature

(b) Turbulent heat flux

Figure 4.20: Non-dimensional evolutions of turbulent quantities at $y = 25$ mm.

et al., 2017). Since T_s was not known precisely in the present work, it was estimated using T_{ss}, such that β was (somewhat crudely) estimated by $\frac{\langle T \rangle - T_{ss}}{y}$.

The non-dimensional local RMS temperature shown in Figure 4.20 (a) increases until reaching a distinct peak at approximately $t = 0.05\tau_m$. After this point, the local non-dimensional RMS temperature decays nearly linearly until the aforementioned quasi-steady state is achieved. The physical explanation of this peak is likely related to the use of T_{ss} as a proxy for T_s. Once T_s reaches 0°C, it will remain constant while the surface layer changes phase. However, the sub-surface temperature will continue increasing, since it is not undergoing melting. After a brief period where T_s is not changing in time, a thin water layer will form and T_s will once again begin to increase. Since θ_{rms} is mostly dependent on T_s (and not T_{ss}), this peak may be interpreted as a "phase lag" between the sub-surface and true surface temperatures. The location of this peak can be indicative of the beginning of the melt phase, consistent with the observations of T_{ss} in Figure 4.17, which place the beginning of the melt phase near $0.1\tau_m$.

Figure 4.20 (b) depicts the evolution of ratio of the turbulent to molecular heat flux. The results show a rapid increase until approximately $0.1\tau_m$, after which point the evolution in time is minimal, again supporting the notion that the melt phase (in which there is not a significantly thick water layer above the ice) occurs at approximately $0.1\tau_m$. Interestingly, the effects of the phase lag between T_{ss} and T_s are not observed in Figure 4.20

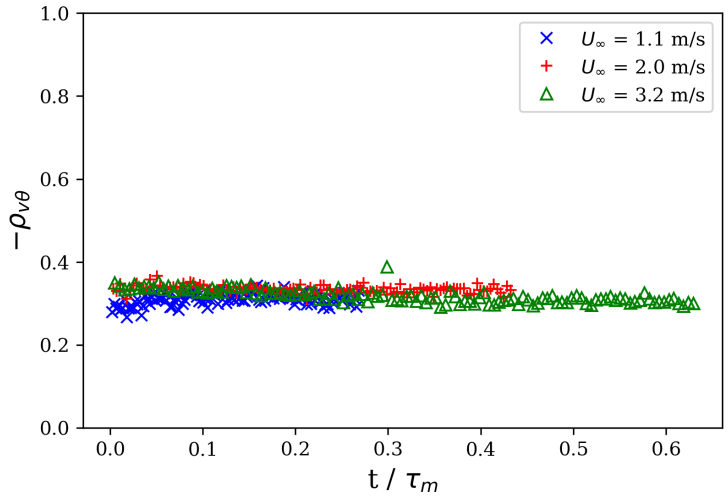

Figure 4.21: Time-dependence of the correlation coefficient $\rho_{v\theta}$ for y=25 mm.

(b). This may be because the temperature gradient β will be determined by the velocity field and boundary conditions, however, the sensitivity of the non-dimensionalization of $\langle v\theta \rangle$ to the difference $T_{ss} - T_s$ is not as high as for the RMS temperature.

A final non-dimensionalization to consider for the turbulent heat flux is the correlation coefficient ($\rho_{v\theta} = \frac{\langle v\theta \rangle}{v_{rms}\theta_{rms}}$). Since it depends upon both $\langle v\theta \rangle$ and θ_{rms} in its formulation, its evolution serves to show how $\langle v\theta \rangle$ evolves with relative to θ_{rms} (since v_{rms} is effectively constant in time). In these experiments it was found that, in general, the correlation coefficient ($\rho_{v\theta}$) did not vary significantly in time. A representative plot of the correlation coefficient as a function of the non-dimensional time is presented in Figure 4.21 for y=25 mm. Its stationarity is notable, since it shows that the change in time of the turbulent heat flux will be proportional to the change in time of the RMS temperature. The values of $\rho_{v\theta}$ observed in the present work generally compare well with those of Arya (1975) for similar levels of stratification ($\rho_{v\theta} \approx -0.3$).

Lastly, it is worthwhile to consider how the stratification changes throughout the melt process. To this end, the bulk Richardson number was calculated as follows:

$$Ri_b = \frac{gy}{\langle T \rangle} \frac{\langle T \rangle - T_{ss}}{\langle U \rangle^2}, \tag{4.13}$$

and the turbulent Richardson number was calculated using:

$$Ri_t = \frac{g\beta}{T_\infty}\left(\frac{\ell}{v_{rms}}\right)^2, \tag{4.14}$$

wherein β was estimated using $\frac{\langle T\rangle - T_{ss}}{y}$, whereby T_{ss} was used as the best approximation for the true surface temperature T_s. These Richardson numbers were plotted against the non-dimensional time and are presented in Figure 4.22 for y=25 mm only, as the effect of U_∞ on the stratification was identical for all three heights (not shown).

After an initial decrease (during the warming period), there is negligible change in the stratification as measured by the Richardson number after approximately $0.1\tau_m$. This result is partially influenced by the use of T_{ss} as an approximation for T_s – as the ice continues to melt and the surface water layer grows, so too will the difference between these two quantities. Given the observed statistical stationarity of the velocity field, the bulk Richardson number will only be a function of the local and surface temperatures, and should change proportionally to $\frac{\langle T\rangle - T_{ss}}{\langle T\rangle}$. Similarly, the turbulent Richardson number will be proportional to $(\langle T\rangle - T_{ss})$. Since T_{ss} is approximately constant after $0.1\tau_m$ (see Figure 4.17), then the changes in Ri_b and Ri_t shown in Figure 4.22 will only be proportional to changes in $\frac{1}{\langle T\rangle}$ and $\langle T\rangle$, respectively. The invariance in time for both of these Richardson numbers shows that $\langle T\rangle$ does not change significantly despite a continued evolution in T_s throughout the melt process. This was confirmed by investigating the percent change in the mean temperature throughout each experiment, which was found to be less than 5% (not shown). Since the bulk and turbulent Richardson numbers as calculated above were not particularly sensitive to the changing surface temperature, their usefulness for parameterizing the turbulent heat fluxes is called into question. In particular, it is important to note that the mean temperature measured at height y, used to calculate the bulk Richardson number for the purpose of estimating the sensible heat flux to melting glaciers (e.g. Fitzpatrick et al., 2017; Hock, 2005), does not show a significant evolution in time as the surface temperature changes, even though there is a continued decrease of the magnitude of the turbulent heat flux, $\langle v\theta\rangle$.

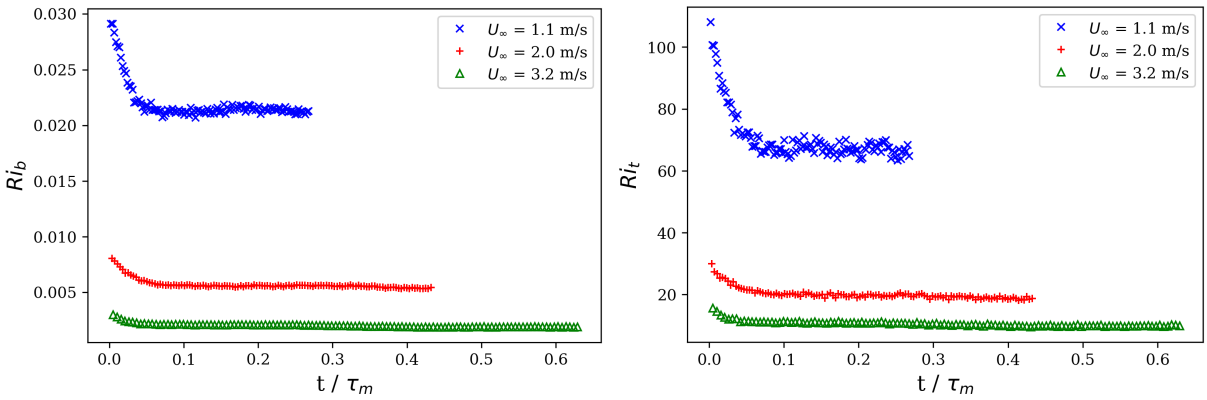

(a) Bulk Richardson number

(b) Turbulent Richardson number

Figure 4.22: Evolution of locally-averaged Richardson numbers for y = 25 mm.

Overall, the temperature and combined temperature-velocity statistics exhibited a transient evolution throughout the course of the experiments as the ice melted. The relative decrease of the locally-averaged RMS temperature and turbulent heat flux was found to be similar for all heights and speeds when non-dimensionalized by their initial values and plotted as a function of the non-dimensional time. Other non-dimensionalizations of the locally-averaged RMS temperature and turbulent heat flux showed that the melt period can be reasonably be expected to occur near $0.1\tau_m$ for all speeds investigated in this work. After an initial decrease during rapid warming of the ice, the stratification was found to be relatively constant throughout the rest of the experiments. In the following section, the temperature and combined velocity-temperature statistics will be evaluated over an interval of time in the melting phase in which they are approximately stationary, and analyzed in a similar manner to the results of the velocity field shown in section 4.2.

4.4 Temperature and Combined Velocity-Temperature Statistics over Melting Ice

The previous section discussed the transient nature of the temperature and combined velocity-temperature statistics over melting ice throughout the course of the experiments. These statistics were measured over solid, warming ice (T_s<0°C), phase-changing melting

ice (T_s=0°C), and liquid water atop melting ice (T_s>0°C). However, the region of interest for the present work is during the melting phase of the experiments, when T_s=0°C (by definition) and there is only a thin film of water atop the ice.

Despite the transient nature of the experiments in which the temperature-related statistics are known to evolve in time, a "snapshot" of the temperature and combined velocity-temperature statistics is required to assess the nature of the temperature field over melting ice (and not warming ice nor liquid water). To this end, a subset of the data containing 3.3×10^6 samples (measured over approximately 10 minutes) was used to serve as a snapshot of the temperature field over melting ice. In the previous section, it was demonstrated that the melt phase begins at approximately $0.1\tau_m$, and so the subsets were taken at this point in time for each of the nine runs in the test envelope. During this period of evaluation, an assumption of statistical quasi-stationarity is necessary to facilitate a similar analysis to that of the velocity field (i.e., PDFs and spectra). To this end, the validity of this assumption was verified by calculating the change in θ_{rms} over the length of a subset, since it underwent a more significant change in time than $\langle v\theta \rangle$. It was found that the average change in θ_{rms} was only 4%, approximately equal to the uncertainty in the velocity measurements, making this assumption of statistical stationarity a sensible one. Given this, the statistics of velocity and temperature quantities measured during this period are presented in Table 4.5.

To investigate the spectra and PDFs of the temperature field in a similar manner to that the velocity field, the non-dimensional wavenumber spectra and PDFs of the temperature fluctuations are presented in Figure 4.23. They are the most similar nearest the wall at $y = 10$ mm, when the temperature gradient is the strongest. As the height is increased, there is more dissimilarity between the spectra for different speeds at the same height. The slope of the spectra also becomes less steep with increasing height, and it is difficult to observe an inertial range with $\kappa_1^{-5/3}$ scaling, indicating that the Reynolds (Mydlarski & Warhaft, 1998) and Péclet (Lepore & Mydlarski, 2012; Lepore & Mydlarski, 2009) numbers are not sufficiently high to satisfy the second hypothesis of KOC theory.

y (mm)	10			25			40		
U_∞ (m/s)	1.1	2.0	3.2	1.1	2.0	3.2	1.1	2.0	3.2
$\langle U \rangle$ (m/s)	0.84	1.47	2.27	0.86	1.63	2.7	1.07	1.76	2.86
$T_\infty - \langle T \rangle$ (°C)	2.5	2.5	2.9	0.6	1.4	1.3	1.0	1.2	1.1
u_{rms} (m/s)	0.111	0.227	0.333	0.095	0.196	0.321	0.079	0.162	0.288
v_{rms} (m/s)	0.036	0.092	0.155	0.038	0.095	0.17	0.044	0.095	0.176
θ_{rms} (°C)	1.115	0.928	0.674	0.399	0.383	0.272	0.126	0.119	0.092
$-\langle uv \rangle$ $(m/s)^2$	0.0014	0.0078	0.0183	0.0015	0.0076	0.0186	0.001	0.0053	0.0168
$-\langle v\theta \rangle$ (Km/s)	0.0112	0.0275	0.0341	0.0048	0.0130	0.0163	0.0003	0.0018	0.0034
ϵ (m^2/s^3)	0.097	0.239	0.682	0.136	0.212	0.322	0.083	0.094	0.21
ϵ_θ (K^2/s)	2.109	1.350	0.674	2.545	0.868	0.270	0.951	0.365	0.14
ℓ (m)	0.050	0.069	0.087	0.060	0.087	0.12	0.089	0.10	0.12
ℓ_θ (m)	0.049	0.053	0.068	0.035	0.051	0.061	0.020	0.029	0.035
λ (mm)	5.3	6.9	6.0	3.9	6.4	8.5	4.1	7.9	9.4
η (mm)	0.43	0.34	0.26	0.4	0.35	0.32	0.45	0.43	0.35
$-\rho_{uv}$	0.35	0.37	0.35	0.42	0.40	0.34	0.29	0.35	0.33
$-\rho_{v\theta}$	0.28	0.32	0.32	0.31	0.34	0.33	0.05	0.14	0.18
Re_ℓ	396	1132	2050	395	1147	2452	480	1093	2383
Re_λ	40	106	135	24	84	182	22	86	182
Ri_b	0.008	0.003	0.001	0.021	0.006	0.002	0.021	0.008	0.003
Ri_t	115	37	19	67	20	11	64	16	7
Pe	256	566	1066	157	473	911	75	221	469

Table 4.5: Average statistics and quantities of velocity and temperature over melting ice, averaged over a 10-minute period centred at $0.1\tau_m$.

Unlike the PDFs of the velocity fluctuations over melting ice, the PDFs of the temperature fluctuations over melting ice are clearly non-Gaussian. The PDFs are asymmetric due to the cooled nature of the flow such that temperatures must be bounded between T_∞ and T_s. The PDFs of the temperature fluctuations are better mixed near the wall, unlike the velocity PDFs, which were less Gaussian near the wall. As the wall-normal distance is increased, the area below the non-Gaussian region of the PDF increases. There is thus an increasing likelihood of measuring a "large" temperature fluctuation relative to θ_{rms} with increasing wall-normal distance from rare, cold fluid particles.

Again mirroring the analysis performed for the velocity field, the coherence spectra between the vertical velocity fluctuations and the RMS temperature fluctuations ($H_{v\theta}$) was evaluated to quantify the spectral composition of the turbulent heat flux over melting ice, and are plotted in Figure 4.24. In all cases, the coherence between v and θ increases with free-stream velocity (i.e. Reynolds number), as increased turbulent activ-

ity increases the turbulent heat transfer. There is a peak coherence at approximately $\kappa_1\eta = 10^{-3}$ for the highest free-stream velocity at all heights, which was not observed on the coherence spectra of uv. The existence of this peak implies that there is a preferential scale for the exchange of heat in the vertical direction that is not the largest scale of the flow. A similar peak was observed by Mestayer (1982) in their investigation of turbulent velocity and temperature statistics in a near-neutral turbulent boundary layer over cooled water, whose bulk Richardson number was approximately 0.0013. Compared to Mestayer's results, the coherence spectra are much lower in magnitude, potentially due to the comparatively lower Reynolds numbers in the present work. In the presence of strongly stable stratification, this peak might be attributable to internal gravity waves at the Brunt-Väisälä frequency ($N_b = \sqrt{\frac{g\beta}{\langle T \rangle}}$ (Tennekes & Lumley, 1972)); however, the stratification in these experiments is too weak for this to be likely. Furthermore, the ratio of the peak frequency to the Brunt-Väisälä frequency was always found to be less than 0.01 for the experiments herein, further reducing the likelihood of this explanation.

The overall magnitude of the coherence (and therefore the correlation coefficient $\rho_{v\theta}$ shown in Table 4.5) was not found to scale predictably with height. This result is consistent with those of Arya (1975) and Ohya et al. (1997), who found that profiles of $\rho_{v\theta}$ exhibited a distinct peak at varying wall-normal distances. For similar levels of stratification to the experiments performed herein, they found this peak to occur around y/δ= 0.33. This corresponds to the $y = 25$ mm height in the present work, in which similar values of $\rho_{v\theta}$ were found to those of Arya (1975) and Ohya et al. (1997).

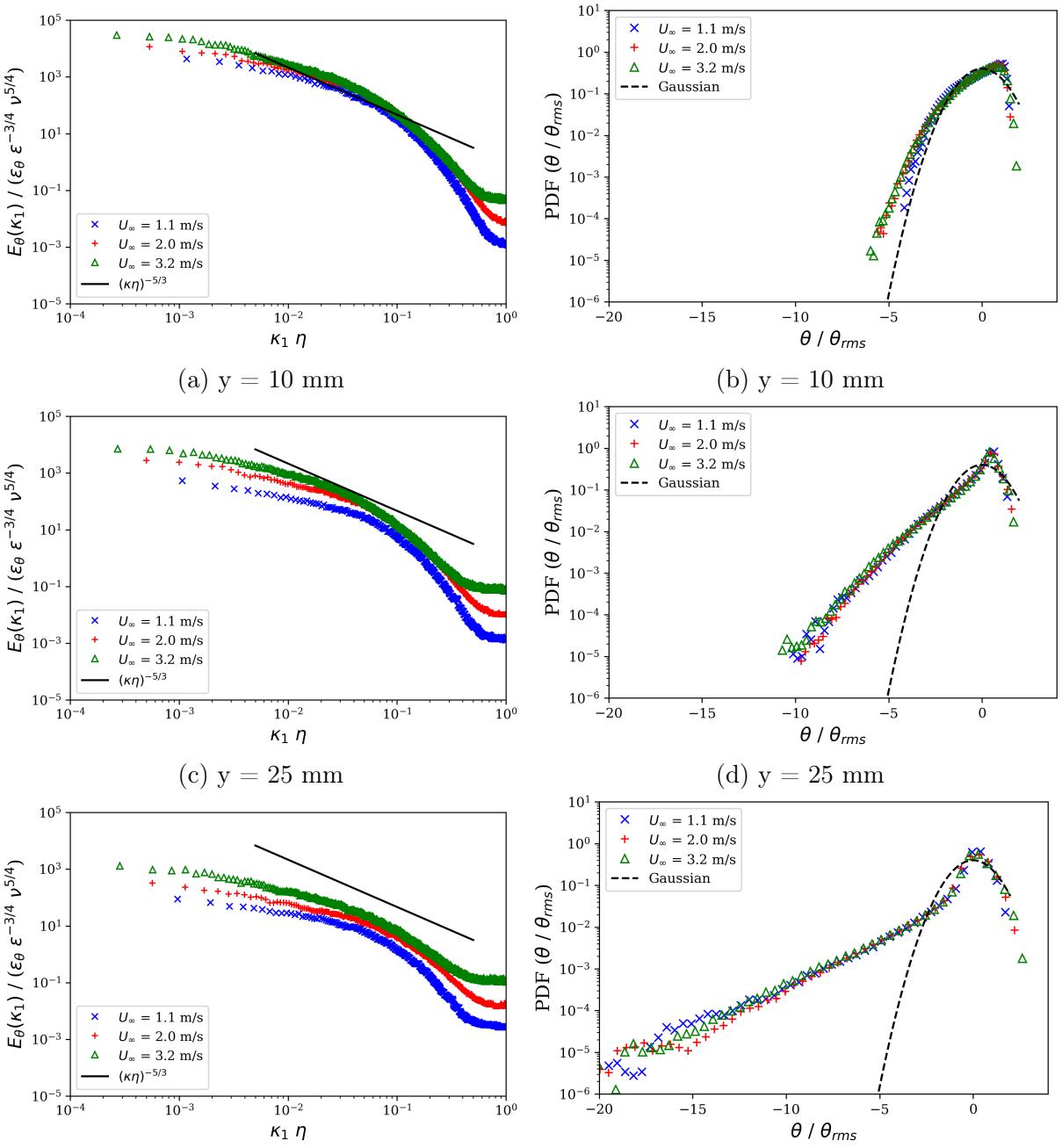

(a) y = 10 mm

(b) y = 10 mm

(c) y = 25 mm

(d) y = 25 mm

(e) y = 40 mm

(f) y = 40 mm

Figure 4.23: Non-dimensional wavenumber spectra (a,c,e) and PDFs (b,d,f) of the temperature fluctuations.

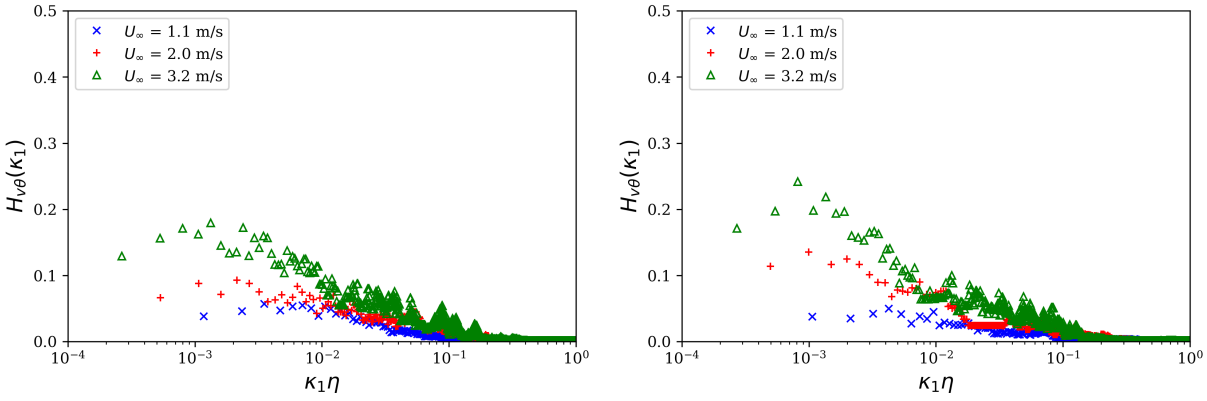

(a) y = 10 mm

(b) y = 25 mm

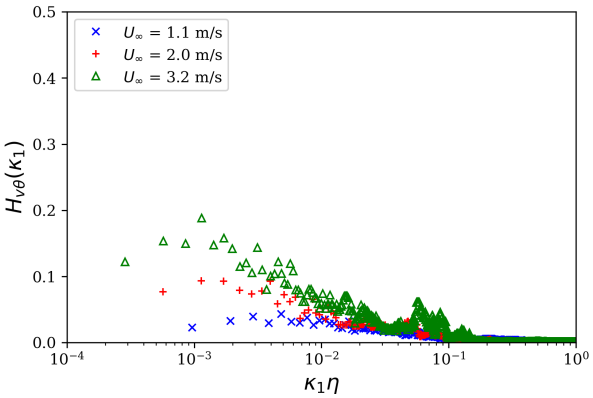

(c) y = 40 mm

Figure 4.24: Non-dimensional coherence spectra of vertical velocity and temperature.

The joint PDFs of the vertical velocity and temperature fluctuations were also computed. Similar to those of u and v, discussed in section 4.2, joint PDFs of v and θ were found to vary primarily with height and showed little dependence on the free-stream velocity. As such, the joint PDFs of v and θ are only shown for the $U_\infty = 2.0$ m/s runs in Figure 4.25. As expected given the PDFs of v (which deviated from Gaussian behaviour in the tails) and θ (which were increasingly non-Gaussian with increasing height), none of the joint PDFs are joint-Gaussian, although the tendency to joint-Gaussian PDFs increases with height apart from a long tail associated with rare temperature fluctuations.

Near the surface, the likelihood of observing a positive (warm) temperature fluctuation where $\theta > \theta_{rms}$ is rare, which explains the flat region in Figure 4.25 (a). As the height is increased, the likelihood of measuring a positive temperature fluctuation relative to θ_{rms} increases, shown by the rounding of the region in the top half of the plots in Figure 4.25 as the joint PDFs approach a joint-Gaussian shape in the region where $\theta > 0$.

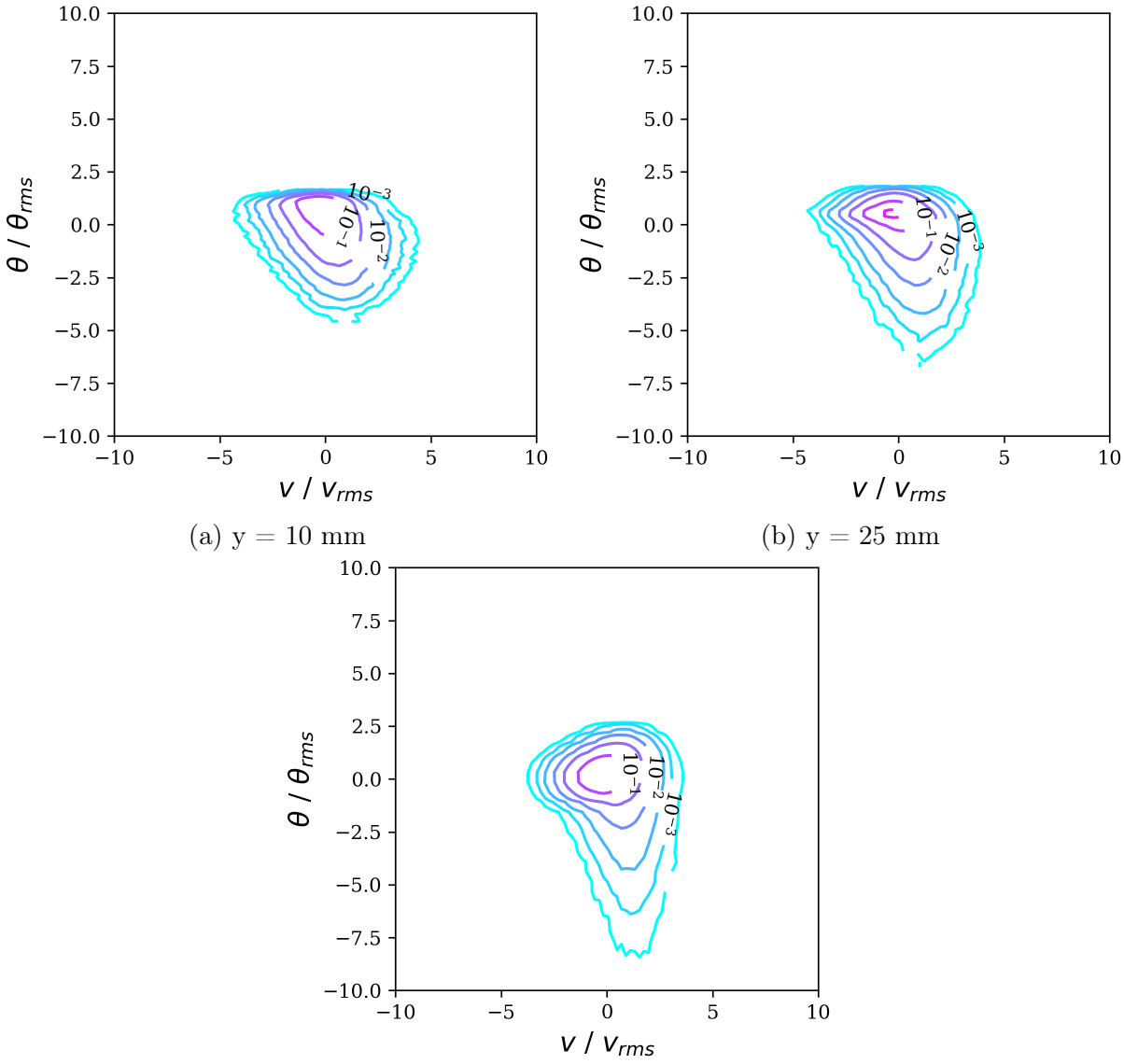

(a) y = 10 mm

(b) y = 25 mm

(c) y = 40 mm

Figure 4.25: Contour plots of joint PDFs of the vertical velocity and temperature fluctuations for $U_\infty = 2.0$ m/s.

It is important to make the distinction between a "large" fluctuation relative to θ_{rms}, and a "large" fluctuation as quantified by its absolute value. Since the RMS temperature decreases with height, and since the bulk temperature differential $(T_\infty - T_s)$ is constant, the magnitude of a certain temperature fluctuation relative to the RMS temperature will also increase with height. For example, consider a warm fluctuation at the top of the outermost contour in Figure 4.25 (a), which will have a magnitude of approximately $1.5 \times \theta_{rms} = 1.4$°C (corresponding to an absolute temperature of $T_\infty - 1.1$°C). The

same fluctuation measured at $y = 40$ mm corresponds to approximately $11.8 \times \theta_{rms}$, an exceptionally rare occurrence as shown by Figure 4.25 (c). This is a consequence of the bounded nature of the temperature field – the minimum temperature measurable is 0°C, whereas the maximum is T_∞. Since $\langle T \rangle$ is closer to T_∞ than T_s, there will be an asymmetry in the joint PDFs of v and θ, which skews towards $\theta < 0$.

The joint PDFs also show that the largest temperature fluctuations are typically associated with smaller velocity fluctuations. Closer to the surface, larger velocity fluctuations are associated with smaller temperature fluctuations. As the height is increased, larger negative velocity fluctuations are still associated with small temperature fluctuations, but larger positive velocity fluctuations are also associated with larger positive temperature fluctuations. Physically, this may be explained by high velocity parcels of air being brought towards the surface by mechanical effects as opposed to buoyancy effects, since the associated temperature fluctuations are small. Near the surface, upward motion may also be more strongly associated with mechanical effects, but as the height increases and vertical motion generated by mechanical shear is weaker, there may be more warm parcels rising rapidly due to buoyancy effects as indicated by the growing region where $\theta > 0$ and $v > 0$.

The PDFs of $v\theta$ were plotted non-dimensionally to evaluate the distribution of the heat flux itself. They are presented in Figure 4.26. The PDFs of $v\theta$ are more symmetrical near the surface, but show an increasing negative skewness with increasing height.

The computation of velocity and temperature statistics at equivalent non-dimensional times for all of the experiments facilitated further analysis of the relationship between the velocity and temperature fields that was not able to be performed using solely the velocity statistics in section 4.2. To understand how the intensity of the temperature fluctuations related to increased anisotropy from the ice surface, the anisotropy ratio (ϕ) was plotted as a function of the non-dimensional RMS temperature (herein referred to as the turbulent intensity of temperature, $Ti_\theta \equiv \frac{\theta_{rms}}{\langle T \rangle - T_s}$, where $T_s = 0$°C) in Figure 4.27. A power law of the form $y = B\ x^n$ was fit to the data, and had an exponent of -0.19.

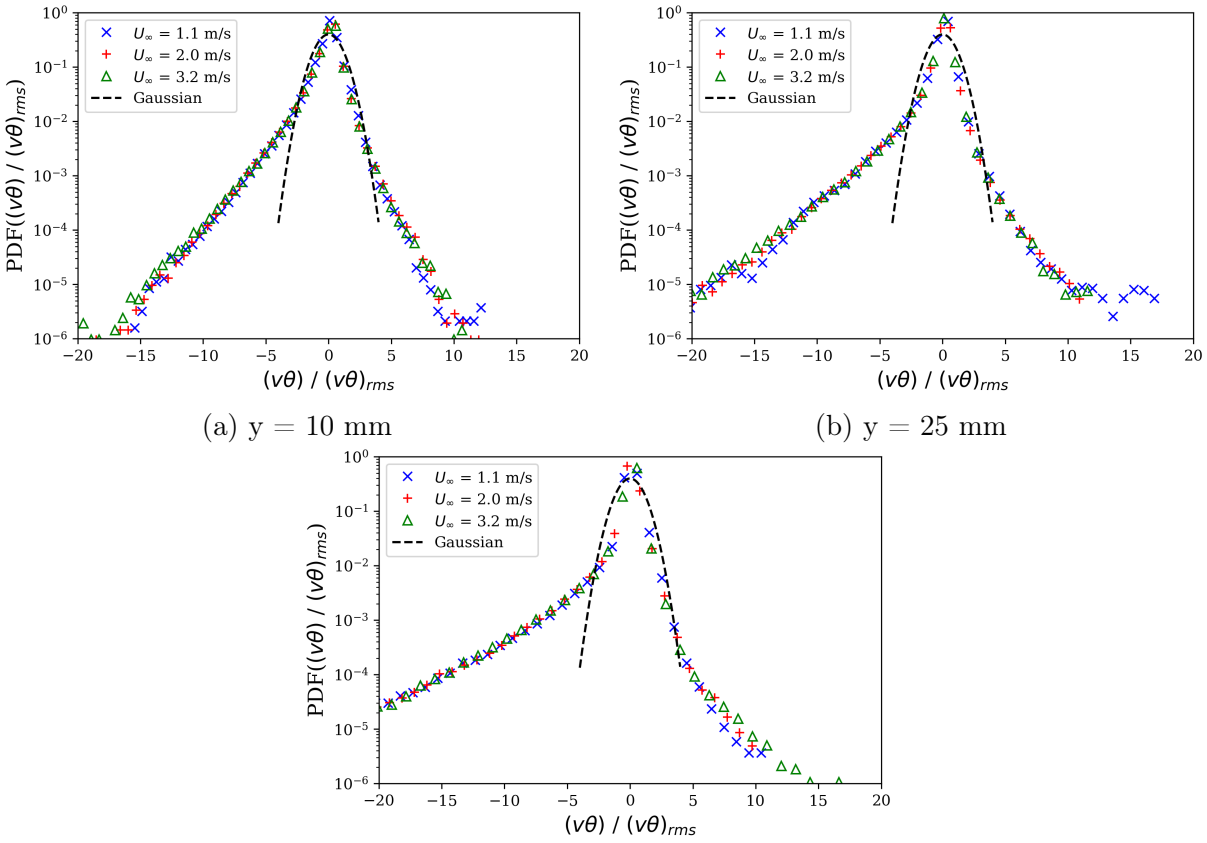

(a) y = 10 mm

(b) y = 25 mm

(c) y = 40 mm

Figure 4.26: Non-dimensional PDFs of $v\theta$ measured over melting ice.

Figure 4.27 shows that the anisotropy ratio is closer to unity when the turbulent intensity of temperature is lower. This is not an unexpected result, given that the most dramatic anisotropy should be reasonably expected to be related to higher-intensity temperature field, which is observed at lower speeds and lower heights (as discussed in the previous section). However, Figure 4.27 also shows that for the largest height (y = 40 mm, triangular markers), the turbulent intensity of temperature is less than 1%. At this height, the temperature fluctuations are exceptionally weak when compared to the mean velocity deficit ($\langle T \rangle - T_s$), such that they may be within the uncertainty of the measurements. This warranted another investigation of the relationship between the anisotropy ratio and the stratification (as quantified by the turbulent Richardson number).

To this end, the anisotropy ratio measured over melting ice is plotted as a function of Ri_t in Figure 4.28. Given the apparent collapse of the data at the lower two heights, it would appear that the outlying data at y = 40 mm is due to the fact that these data

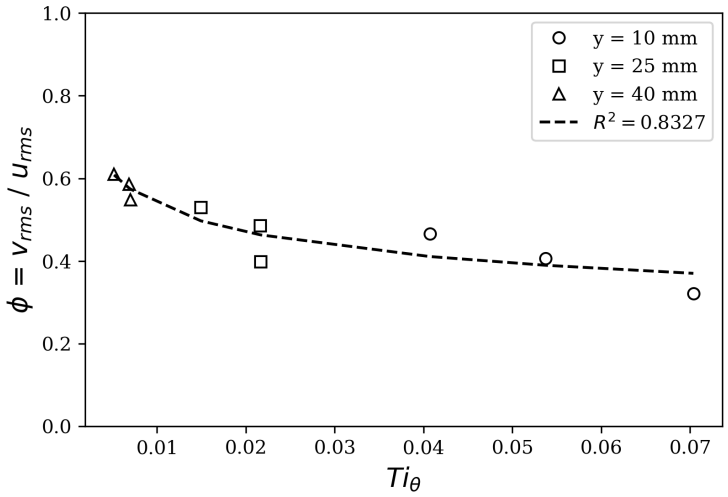

Figure 4.27: Anisotropy ratio plotted as a function of turbulent intensity of temperature. The best-fit power law was $\phi = 0.224 Ti_\theta^{-0.19}$

are in the outer, intermittent fringes of the thermal boundary layer. This conclusion is consistent with the values of $\rho_{v\theta}$ in Table 4.5, which fall in the range of -0.05 to -0.018 for the $y = 40$ mm data set, and which are substantially lower than the values for $y =$ 10 and 25 mm, which are all approximately -0.3.

A dependence of the relationship between the anisotropy ratio on the turbulent Richardson number has only been previously observed in studies investigating the downstream evolution of stratified turbulent flows (Piccirillo & van Atta, 1997; Yoon & Warhaft, 1990), whereas the anisotropy ratio has been found to be relatively constant for different levels of stratification in boundary layer flows (Williams et al., 2017). Figure 4.28 validated the observed relationship between these two quantities previously noted in Figure 4.10, with additional insight obtained from the temperature statistics. In this case, there is a clear relationship between the anisotropy ratio and turbulent Richardson number measured over melting ice for the cases where the turbulent intensity of the temperature field is greater than 1%.

In addition to the observed Richardson number scaling of the anisotropy ratio for the experiments at $y = 10$ and 25 mm, it was also of interest to investigate possible scalings of the turbulent heat flux evaluated over melting ice. To this end, the turbulent heat flux was non-dimensionalized by $\alpha\beta$ to form the turbulent Nusselt number ($Nu_t \equiv -\langle v\theta \rangle / \alpha\beta$)

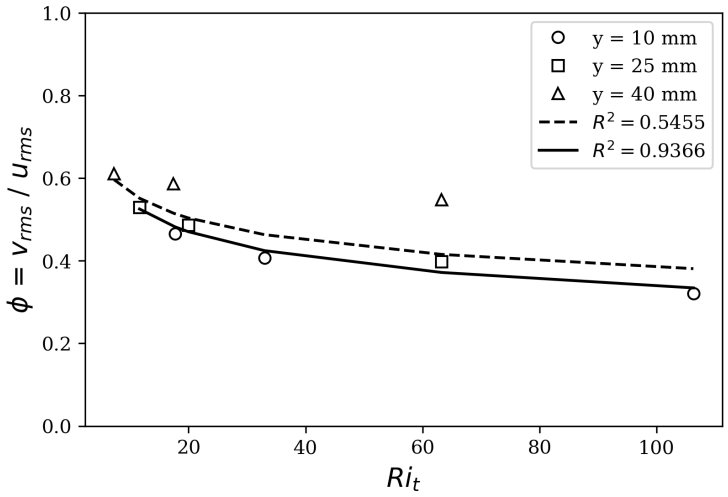

Figure 4.28: Anisotropy ratio measured over melting ice as a function of turbulent Richardson number. The dashed line represents the best-fit power law to the data using all nine experiments, whereas the solid lines represents the best-fit power law using only data measured at the 10 and 25 mm heights. The best-fit power law was $\phi = 0.856 Ri_t^{-0.20}$.

and plotted as a function of the Taylor-microscale Reynolds number. In the present work, where the flow is weakly stably stratified, the turbulent Nusselt number was also plotted as a function of the turbulent Richardson number. The plots are presented in Figure 4.29, shown with the best-fit power laws. Due to the low magnitude of the turbulent heat flux at the highest measurement height ($y = 40$ mm), two power law fits were performed. One fit was applied to all nine cases in the test envelope (dashed lines), and the other was applied to only the results from the $y = 10$ and 25 mm heights (solid lines).

The data for the $y = 40$ mm heights are significantly lower in magnitude than the other two heights. The weak turbulent heat flux at this height is presumably caused by external intermittency at the edge of the thermal boundary layer (Tennekes & Lumley, 1972), as noted earlier. The powers of the fits excluding the $y = 40$ mm data (solid lines) in Figure 4.29 (a) and (b) are 0.60 and -0.49, respectively. The exceptionally low values of the turbulent heat flux at $y = 40$ mm observed in these plots, which are inconsistent with the data fully within the thermal boundary layer, is used as justification for the omission of the $y = 40$ mm height data in the parameterization of the turbulent heat flux in section 4.5.

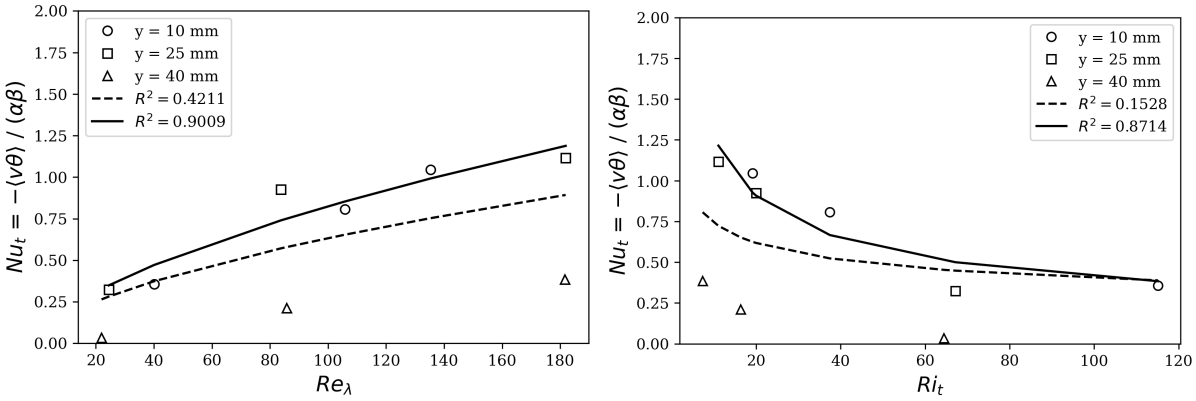

(a) Taylor-microscale Reynolds number (b) Turbulent Richardson number

Figure 4.29: Turbulent Nusselt number plotted as a function of non-dimensional quantities. Dashed lines represent the best-fit power law using all nine experiments, whereas solid lines represent the best-fit power law using only the 10 and 25 mm heights.

4.5 Parameterization of Turbulent Heat Fluxes

The preceding section presented and discussed the turbulent velocity and temperature fields measured over melting ice. However, in addition to investigating the statistical nature of weakly stratified turbulence over a phase-changing surface, an important objective of this work was the use of simultaneous two-component velocity and temperature measurements to parameterize the turbulent heat flux for the purpose of improving surface energy balance modelling of glacier melting. Data recorded at $0.1\tau_m$ (i.e. during the melting period) that were used to calculate the spectra and PDFs presented in the preceding section are used in this section to parameterize the turbulent heat fluxes. Since the turbulent temperature field and turbulent heat fluxes were found to be exceptionally weak at the $y = 40$ mm measurement height, and likely in the range of the measurement uncertainty, they are omitted from the parameterizations of this section. As such, only the results pertaining to the $y = 10$ and 25 mm heights are investigated herein.

The accuracy of the bulk method was first evaluated to serve as a baseline of comparison for the parameterization developed later in this section. To be considered a meaningful improvement to the existing bulk method, any proposed parameterization must perform better than the existing bulk method as implemented in the present work.

4.5.1 Evaluation of the Bulk Method

The bulk method is used to model the turbulent heat flux ($\langle v\theta \rangle$) using the average (i.e. bulk) streamwise velocity ($\langle U \rangle$) and temperature ($\langle T \rangle$). Given its low operational requirements (as described in section 2.5), it is the standard method used for estimating turbulent heat fluxes over melting glaciers in field studies. The bulk quantities are related to the turbulent heat flux through the use of a bulk exchange coefficient (C_H) as follows:

$$\langle v\theta \rangle = C_H \langle U \rangle (\langle T \rangle - T_s), \tag{4.15}$$

where T_s is assumed to be 0°C. While this assumption is reasonable during melt periods, it induces error when the glacier is not actively melting (Denby & Greuell, 2000). Accurately estimating the bulk exchange coefficient is crucial for the success of the bulk method, and as such, there are countless studies dedicated to parameterizing its value (Chambers et al., 2020).

A common method to estimate the bulk exchange coefficient (C_H) is using equation (2.38) from section 2.5, in which a logarithmic velocity profile is assumed, and the effects of stratification are captured using the Monin-Obukhov stability parameter. Though it is generally well-understood that glacier flows are typically katabatic (Oerlemans & Grisogono, 2002), and therefore the logarithmic profile assumption is usually invalid, the widespread adoption of the bulk method is not inhibited. When the Monin-Obukhov similarity parameter is not directly calculable (such as in the present work), it is often estimated using the bulk Richardson number (Webb, 1970). Using this method, the bulk exchange coefficient is given by:

$$C_H = \frac{\kappa}{\ln\left(\frac{y}{y_0}\right) ln\left(\frac{y}{y_{0_\theta}}\right)} (1 - 5.2Ri_b)^2, \tag{4.16}$$

where roughness parameters y_0 and y_{0_θ} are typically on the order of 10^{-3} m for a real glacier (Fitzpatrick et al., 2017).

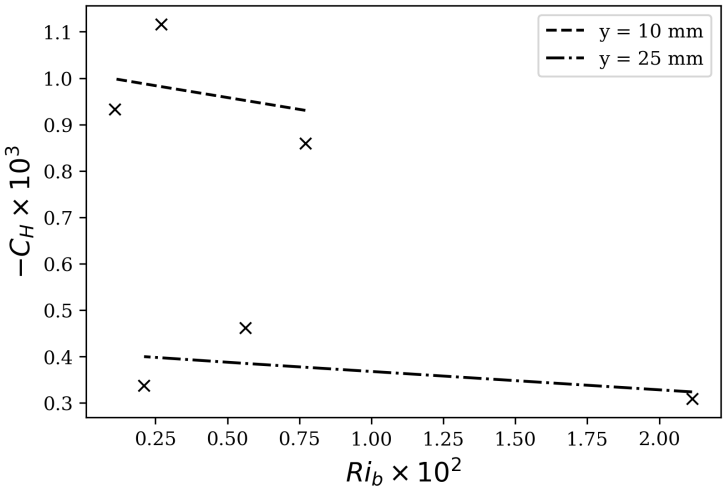

Figure 4.30: Bulk exchange coefficient fitted using equation (4.17).

To implement the bulk method in the present work, and subsequently evaluate its error by comparison to the true heat fluxes measured over melting ice, one requires knowledge of these roughness parameters to estimate C_H. Using values similar to those of real glaciers was not appropriate given the smaller scales of the present work when compared to real-world field studies. Similarly, using the RMS roughness value of the ice surface (found to be approximately 0.4 mm in section 3.2.2) was not appropriate, since the surface roughness does not share the same definition as the aerodynamic roughness. Therefore, to compare the results of the bulk method to the true values measured in the present work, the parameters y_0 and y_{0_θ} had to be estimated using other methods. To this end, the bulk exchange coefficient was first directly calculated by re-arranging equation (4.15), in which T_{ss} was used to estimate T_s. For experiments performed at the same height, y, y_0, and y_{0_θ} are all constant, and equation (4.16) reduces to:

$$C_H = K(1 - 5.2Ri_b)^2, \tag{4.17}$$

where K is a constant. Using the directly calculated bulk exchange coefficient from equation (4.15), the constant K was found using least-squares regression. Figure 4.30 shows the directly calculated bulk exchange coefficient, as well as the curve fits found using equation (4.17), which show better agreement at $y = 25$ mm than $y = 10$ mm.

y (mm)	U_∞ (m/s)	$\langle v\theta \rangle$ (m/s K)	$\langle v\theta \rangle_{bulk}$ (m/s K)	Relative Error
10	1.1	-0.0112	-0.0121	8.32 %
	2.0	-0.0275	-0.0242	-12.03 %
	3.2	-0.0341	-0.0365	7.00 %
25	1.1	-0.0048	-0.0050	4.72 %
	2.0	-0.0130	-0.0108	-16.63 %
	3.2	-0.0163	-0.0193	18.42 %
RMS Error				11.2 %

Table 4.6: True heat flux versus bulk method predictions with relative and RMS error.

The values of C_H from the curve fits were then used to estimate the true turbulent heat flux. It is important to recognize that this implementation serves as a best-case scenario for the bulk method. In reality, the bulk exchange coefficient cannot be calculated directly (as done in the present work), and there are three degrees of freedom by which errors in the estimation of y, y_0, and y_{0_θ} are introduced. In typical glacier melt studies, these parameters are difficult to model accurately. Ablation of the glacier surface will change the measurement height y throughout the course of a field observation (Hock, 2005), while estimation of the roughness lengths represents a significant challenge in the glaciology community (Chambers et al., 2020). The errors associated with estimating these parameters are considered to be higher than error associated with the theory surrounding the bulk method (Radić et al., 2017). As such, the implementation of the bulk method in the present work justifiably represents an optimal performance of the bulk method for estimating the turbulent heat flux over melting ice.

Having stated this, Table 4.6 shows the results of the predictions of the bulk method alongside the true heat flux for the six runs investigated herein. Overall, this best-case implementation shows good accuracy, with lower RMS error (11.2% in the present work) than typical real-world applications (e.g. Denby & Greuell, 2000; Fitzpatrick et al., 2017) which generally have an RMS error of around 25-30%. With a baseline level of accuracy for the performance ceiling of the bulk method having been determined, a novel method for estimating the turbulent heat flux is presented in the following section. To be a useful parameterization, the RMS error of the new method should be lower than that of the bulk method found herein.

4.5.2 Statistical Heat Flux Method

Before presenting a novel method for predicting the turbulent heat flux above melting ice, it is important to ensure that it will be of practical use to those wishing to make such predictions. Therefore, to replace the bulk method, the novel method must abide by the same operational restrictions of the equipment used in most glacier field studies. Concretely, these restrictions are that:

1. Only statistics of the streamwise velocity and temperature may be used, as typical automated weather stations only measure one (horizontal) component of velocity.

2. Free-stream quantities (U_∞, T_∞, and δ) may not be used, since knowledge of these would require the measurement of velocity and temperature at several heights such that the height of the wind speed maximum (δ) can be found.

3. Small-scale (i.e. dissipation-related) quantities such as λ and η may not be used, since automated weather stations cannot adequately resolve these scales.

4. Quantities that are only measurable using high-frequency sampling (e.g. ϵ, ℓ) may not be used, since automated weather stations do not have an adequately high sampling rate to calculate these quantities.

Given that the bulk method uses mean quantities ($\langle U \rangle$ and $\langle T \rangle$) to estimate a turbulent quantity ($\langle v\theta \rangle$), a sensible approach to improving the bulk method is to replace the mean scales of velocity and temperature with their respective RMS quantities. These serve as characteristic scales of the turbulent fluctuations, which should be more closely related to the turbulent heat flux than the mean quantities. Using these quantities, the turbulent heat flux can be re-written as:

$$\langle v\theta \rangle = \sigma u_{rms} \theta_{rms}, \tag{4.18}$$

where σ is a scaling coefficient, similar in purpose to the bulk exchange coefficient. The

product of σ, u_{rms} and θ_{rms} is referred to herein as the "statistical" heat flux, since it uses the relevant statistical quantities while sharing dimensions with $\langle v\theta \rangle$.

The exact value of the scaling coefficient (σ) can be determined analytically using the equation for the correlation coefficient of v and θ:

$$\rho_{v\theta} \equiv \frac{\langle v\theta \rangle}{v_{rms}\theta_{rms}}. \tag{4.19}$$

Using the anisotropy ratio (ϕ), v_{rms} can be replaced with u_{rms} in equation (4.19) such that:

$$\rho_{v\theta} = \frac{\langle v\theta \rangle}{\phi u_{rms}\theta_{rms}}. \tag{4.20}$$

By re-arranging equation (4.20) and combining it with equation (4.18), it can be seen that:

$$\sigma = \rho_{v\theta}\phi. \tag{4.21}$$

Therefore, knowledge of the correlation coefficient ($\rho_{v\theta}$) and anisotropy ratio (ϕ) can facilitate direct calculation of the turbulent heat flux ($\langle v\theta \rangle$) using the statistical heat flux ($u_{rms}\theta_{rms}$). This method to calculate the turbulent heat flux requires no assumptions about the surface temperature, stability conditions, or surface roughness. Unfortunately, profiles of $\rho_{v\theta}$ for a stably stratified boundary layer show complex shapes which are difficult to predict analytically (Arya, 1975; Ohya et al., 1997), especially with the limited number of measurement heights used in the present work. Furthermore, while the anisotropy was found to be strongly related to the turbulent Richardson number (Ri_t) in section 4.4, its calculation requires knowledge of the vertical RMS velocity, which is not a usable parameter given the restrictions outlined above.

It was therefore necessary to find an empirical correlation between the coefficient σ and a non-dimensional quantity which could be reasonably measured by an automated weather station over a melting glacier. Given the observed dominance of the turbulent heat flux by the turbulent velocity field in section 4.3, it is reasonable to expect that this quantity should be related to velocity statistics. To this end, a turbulent Reynolds

number (Re_y) with u_{rms} as its velocity scale and the height of the measurement (y) as its length scale was defined:

$$Re_y \equiv \frac{u_{rms} y}{\nu}. \tag{4.22}$$

This Reynolds number is similar to the turbulent Reynolds number Re_ℓ, whereby the integral length scale is replaced by the height y, since ℓ is not realistically attainable from an automated weather station. This definition bears similarity to the definitions of the Reynolds number used in stratified boundary layer turbulence, which use the free-stream Reynolds number ($Re_\delta = \frac{U_\infty \delta}{\nu}$) to characterize the flow (Arya, 1975; Ohya et al., 1997; Williams et al., 2017).

To justify the choice of y as the characteristic length scale, consider Prandtl's mixing length model, often used in atmospheric science, where it has been found to be valid approximation despite its criticisms in fundamental studies of turbulence (Chan & Sofia, 1987). The mixing length model, which is also commonly used in glacier melt studies (Hock, 2005), states that the integral length scale (ℓ) will be proportional to y (Tennekes & Lumley, 1972). Therefore, Re_y employs the foundation of Prandtl's mixing length model to replace ℓ with y in the classical turbulent Reynolds number. Since the purpose of this substitution is to make this non-dimensional quantity (Re_y) an easily measurable one in glacier field studies, in which Prandtl's mixing length model is reasonably valid, the choice of y as a characteristic length scale is sensible.

Having justified the use of the turbulent mixing Reynolds number, it was used to plot the scaling coefficient (σ) for the statistical heat flux method, as shown in Figure 4.31. A consistent power law correlation is observed between these two quantities, with a best-fit exponent of 0.34. The predicted values of σ using the power-law fit were then used to estimate the true value of the turbulent heat flux above melting ice, similar to the procedure for the bulk method. The true heat flux values are presented alongside the predictions of the statistical and bulk methods in Table 4.7.

The results show that the statistical heat flux method, using the parameterization for σ, provides accurate estimations for the turbulent heat flux, with an RMS error of

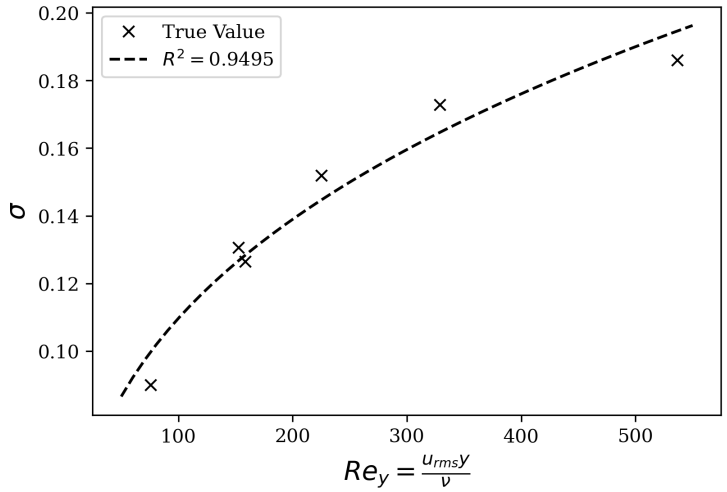

Figure 4.31: Statistical heat flux scaling coefficient σ plotted as a function of the new turbulent Reynolds number Re_y. The best-fit power law was $\sigma = 0.0228 Re_y^{0.34}$

y (mm)	U_∞ (m/s)	$\langle v\theta \rangle$ (m/s K)	$\langle v\theta \rangle_{stat}$ (m/s K)	Relative Error	$\langle v\theta \rangle_{bulk}$ (m/s K)	Relative Error
10	1.1	-0.0112	-0.0124	10.74 %	-0.0121	8.32 %
	2.0	-0.0275	-0.0267	-2.94 %	-0.0242	-12.03 %
	3.2	-0.0341	-0.0325	-4.81 %	-0.0365	7.00 %
25	1.1	-0.0048	-0.0049	1.51 %	-0.0050	4.72 %
	2.0	-0.0130	-0.0124	-4.72 %	-0.0108	-16.63 %
	3.2	-0.0163	-0.0170	4.64 %	-0.0193	18.42 %
RMS Error			-	4.9 %	-	11.2 %

Table 4.7: True heat flux versus statistical and bulk method predictions with relative and RMS error.

only 4.9% compared to the RMS error of the optimized bulk method (11.2%). The RMS error of the statistical heat flux method approaches the experimental uncertainty of the velocity measurements (4.1%), such that improved accuracy within the context of the present work is unlikely. In all but one of the six runs, the statistical heat flux method significantly outperformed the bulk method, as noted in Table 4.7.

In its current form, the newly-defined statistical heat flux method outperforms a best-case implementation of the bulk method, which has experienced years of refinement. Since the derivation of the statistical heat flux method is based on the definitions of the correlation coefficient and anisotropy ratios, there is theoretically no upper limit to its accuracy, unlike the bulk method which is limited by its additional approximations. Furthermore, there were no assumptions made about the surface temperature, roughness,

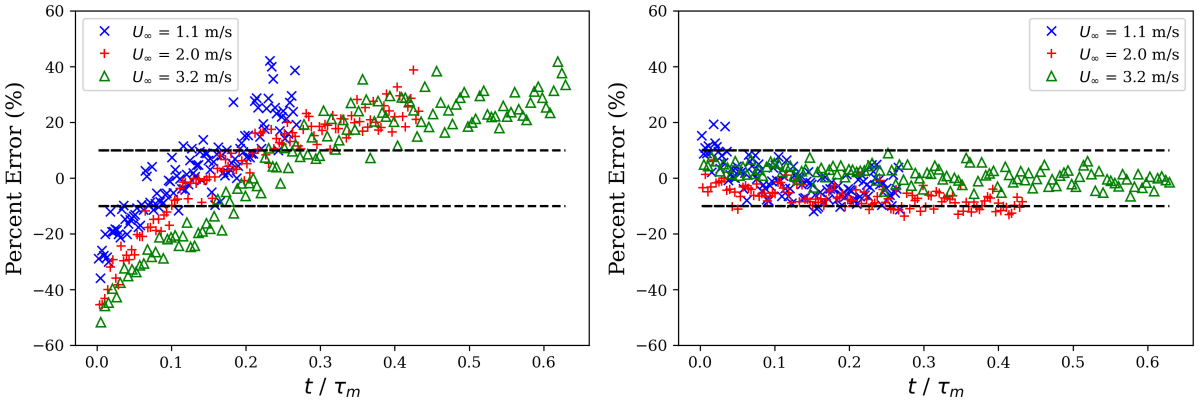

(a) Bulk method

(b) Statistical heat flux method

Figure 4.32: Percent error as a function of non-dimensional time. Dashed lines denote ±10% error.

or phase, representing another advantage of the statistical heat flux method when compared to the bulk method. Moreover, the statistical heat flux method can be reasonably applied to predict the turbulent heat flux at any stage of the melt cycle, unlike the bulk method (which relies on a 0°C surface temperature assumption). To illustrate this point, the percent error between the true turbulent heat flux and predicted turbulent heat flux was plotted as a function of the non-dimensional time for both methods at the $y = 25$ mm height in Figure 4.32. Throughout the entire melt process investigated herein, the error associated with the statistical heat flux method (Figure 4.32 (b)) is bounded by approximately ±10% (shown in dashed lines), which is significantly lower than that of the bulk method (Figure 4.32 (a)). The average RMS error throughout the course of the experiments for the bulk and statistical heat flux methods at $y = 25$ mm were found to be 13.7% and 8.4%, respectively. In addition to the enhanced accuracy for predicting the turbulent heat fluxes over melting ice when compared to the bulk method, the statistical heat flux method also offers improved performance when evaluated over a surface with changing temperature and phase.

Overall, the statistical heat flux method represents a novel way to estimate the turbulent heat flux over melting ice with half of the RMS error of an idealized implementation of the current bulk method. This improvement comes without needing to make assumptions about the surface conditions, and requires only measurements of the streamwise

velocity and temperature, which do not have stringent sampling requirements. In addition, this method can also be used to estimate the turbulent heat flux over a phase changing surface, such that knowledge of the surface phase or temperature is not necessary. Whereas the bulk method is limited by its performance ceiling for estimating the turbulent heat fluxes over melting ice (Radić et al., 2017), the statistical heat flux method suffers from no such limitation, and could theoretically offer even better accuracy if appropriate parameterizations of the scaling coefficient σ are found.

Chapter 5:

Conclusions and Future Work

The present work aimed to improve the understanding of the turbulent velocity and temperature fields over melting ice, while parameterizing the sensible turbulent heat flux. To this end, a series of turbulent flows representative of those typically seen over glaciers were reproduced in a laboratory-scale wind tunnel using an active grid to generate homogeneous isotropic turbulence with similar turbulent intensities and Richardson numbers to those observed in katabatic glacier flow. A novel glacier model was constructed to fit inside the wind tunnel. Hot-wire anemometry and cold-wire thermometry were used to make simultaneous measurements of two components of velocity and temperature, respectively, at three different heights in the turbulent boundary layer above the glacier model for three different free-stream velocities.

The statistics of the turbulent velocity field were measured over melting ice, and subsequently compared to those of the baseline flow (i.e., the same free-stream velocity, but in the absence of ice). It was found that the spectra of the streamwise (longitudinal) and vertical (transverse) velocity components did not change significantly between the experiments over ice and the baseline cases, however there were small differences observable in the tails of the PDFs. Investigations of the joint PDFs also showed a strong similarity between the experiments over ice and the baseline cases, whereas the coherence spectra showed a distinct reduction in magnitude for the experiments over ice at the lowest height, with larger reductions in magnitude being observed with increasing Reynolds number. Furthermore, decreases in the vertical velocity variance and Reynolds stress were observed over melting ice, consistent with the literature pertaining to stably stratified flows. However, an increase in the streamwise velocity variance was also observed, which has not been observed in studies of stably stratified turbulence over solid, non-melting surfaces. This increase may be attributed to the different nature of the boundary condition at the surface of the melting ice when compared to a solid surface.

The transient evolutions of the temperature and combined velocity-temperature statistics measured throughout the melting process were also investigated. Both types of statistics were found to evolve in time similarly for different heights and speeds when non-dimensionalized using a time scale associated with the bulk convective heat transfer to the surface, decreasing in magnitude as the ice surface melted. After experiencing an initial decrease, it was observed that the level of stratification (as measured by the bulk and turbulent Richardson numbers) did not change significantly throughout the course of the experiments, even though the RMS temperature fluctuation and the turbulent heat flux continued to evolve in time. This was due in part to the formulation of these Richardson numbers using the sub-surface temperature as an approximation of the true surface temperature, but was also attributed to the mean temperature measured at the measurement height, which was found to be less sensitive to continued change in the surface temperature than the RMS temperature and turbulent heat flux.

The statistics of the temperature and combined velocity-temperature fields over melting ice were then assessed during a shortened interval occurring at an equivalent non-dimensional time for all nine runs, in which an assumption of quasi-stationarity was made. PDFs of the temperature fluctuations showed non-Gaussian behaviour, unlike the PDFs of velocity which were found to be nearly Gaussian. Coherence spectra of the vertical velocity and temperature fluctuations were evaluated and found to have a distinct peak for the measurement height nearest the surface, comparing well with similar results measured over cooled water from the literature. Joint PDFs of the vertical velocity and temperature fields showed a general trend towards joint-Gaussian behaviour at larger heights, apart from an elongated tail of large, negative temperature fluctuations which were transported upward by positive velocity fluctuations.

Investigations of the correlation between the anisotropy ratio and turbulent intensity of the temperature field, as well as correlations between the turbulent Nusselt number and Reynolds and Richardson numbers showed that the largest measurement height in the present work was on the externally intermittent fringe of the thermal boundary layer.

It was therefore excluded from further parameterizations, in which a novel method for estimating the turbulent heat flux within the thermal boundary layer over melting ice was developed. This new method (herein called the statistical heat flux method) was compared to the existing bulk method, which is the most common way to estimate the sensible turbulent heat flux over melting ice in field studies of glacier melting, and was found to offer a significant improvement in terms of accuracy, having half the RMS error of an idealized implementation of the bulk method. Furthermore, the statistical heat flux method did not rely on assumptions about the surface temperature or shape of the profiles of velocity and temperature (unlike the bulk method), and demonstrated improved accuracy throughout the entire melt process (from solid ice below 0°C, to liquid water above 0°C) when compared to the bulk method.

Future Work

While the present work contributes to the understanding of the turbulent velocity and temperature fields over melting ice and offers a novel method of estimating the sensible heat flux over melting ice with improved accuracy when compared to the bulk method, it also provides many opportunities for future work.

From a fundamental turbulence perspective, the effects of stable stratification on the velocity field over melting ice can be further studied. In the present work, the velocity field was investigated for bulk Richardson numbers in the range of 0.001 to 0.05 and turbulent intensities in the range of 10-15%, which are consistent with those observed above melting glaciers. However, further studies should be performed both at greater Reynolds and Richardson numbers, to validate the observations of the second-order statistics over melting ice, as well as to determine the extent of the difference between the effect of stable stratification over a solid versus melting surface.

From the perspective of replicating katabatic glacier flows in wind tunnel experiments, the present work considers only the region below the wind speed maximum, which is the dominant region for convective heat transfer to the surface. In real-world flows, the tem-

perature profile in this region is approximately linear. However, the temperature profile in the present work was closer to the traditional logarithmic shape found in turbulent boundary layers. A more accurate model of katabatic glacier flow could be achieved by use of a turbulent jet mounted inside the wind tunnel, at varying heights above the floor. The height of the jet would represent the wind-speed maximum, and may allow for a more accurate representation of katabatic glacier flow.

Finally, from the perspective of modelling glacier melt, the present work can be easily extended to measure all terms in the surface energy budget, facilitating investigations of the relationship between each of the different heat fluxes to a melting glacier. To experimentally measure each of the relevant terms in the surface energy budget for a melting glacier, in addition to the apparatus of the present work (which allows for direct calculation of the sensible heat flux Q_H), one would require:

1. A similar glacier model outfitted with several thermocouples embedded in the ice surface to measure the ground conductive heat flux Q_c;

2. A high frequency-response humidity sensor to be used alongside an X-wire probe for calculation of the latent heat flux Q_L;

3. A thermal imaging camera to provide accurate surface temperature and albedo measurements, quantifying the net radiative heat flux Q_N, and also allowing for better parameterizations of Q_H and Q_L using accurate measurements of T_s;

4. A method for collecting and measuring the mass of meltwater after each experiment, facilitating the calculation of the total melt energy flux Q_m.

These additions would allow for laboratory studies and parameterizations of the glacier melt process which would otherwise be unobtainable through field studies, ultimately improving the ability of glaciologists and climate scientists to predict glacier melt.

References

Arya, S. (1975). Buoyancy effects in a horizontal flat-plate boundary layer. *Journal of Fluid Mechanics*, *68*(2), 321–343.

Bash, E. A., & Marshall, S. J. (2014). Estimation of glacial melt contributions to the Bow River, Alberta, Canada, using a radiation-temperature melt model. *Annals of Glaciology*, *55*(66), 138–152.

Beaulac, S., & Mydlarski, L. (2004a). Dependence on the initial conditions of scalar mixing in the turbulent wake of a circular cylinder. *Physics of Fluids*, *16*(8), 3161–3172.

Beaulac, S., & Mydlarski, L. (2004b). Inverse structure functions of temperature in grid-generated turbulence. *Physics of Fluids*, *16*(6), 2126–2129.

Berajeklian, A., & Mydlarski, L. (2011). Simultaneous velocity-temperature measurements in the heated wake of a cylinder with implications for the modeling of turbulent passive scalars. *Physics of Fluids*, *23*(5), 055107.

Bergman, T., Bergman, T., Incropera, F., DeWitt, D., & Lavine, A. (2011). *Fundamentals of Heat and Mass Transfer*. Wiley.

Bou-Zeid, E., Higgins, C., Huwald, H., Meneveau, C., & Parlange, M. B. (2010). Field study of the dynamics and modelling of subgrid-scale turbulence in a stable atmospheric surface layer over a glacier. *Journal of Fluid Mechanics*, *665*, 480–515.

Braithwaite, R. J. (1995). Aerodynamic stability and turbulent sensible-heat flux over a melting ice surface, the Greenland ice sheet. *Journal of Glaciology*, *41*(139), 562–571.

Browne, L., Antonia, R., & Chua, L. (1988). Calibration of X-probes for turbulent flow measurements. *Experiments in Fluids*, *7*(3), 201–208.

Brümmer, B., Busack, B., Hoeber, H., & Kruspe, G. (1994). Boundary-layer observations over water and Arctic sea-ice during on-ice air flow. *Boundary-layer Meteorology*, *68*(1), 75–108.

Bruun, H. H. (1995). *Hot-wire anemometry*. doi:10.1088/0957-0233/7/10/024

Chambers, J. R., Smith, M. W., Quincey, D. J., Carrivick, J. L., Ross, A. N., & James, M. R. (2020). Glacial aerodynamic roughness estimates: Uncertainty, sensitivity, and precision in field measurements. *Journal of Geophysical Research: Earth Surface*, *125*(2), e2019JF005167.

Chan, K. L., & Sofia, S. (1987). Validity tests of the mixing-length theory of deep convection. *Science*, *235*(4787), 465–467.

Cohen, A. (2019). *Influences of free-stream turbulence and char-layer porosity on the drag on windborne firebrands*. McGill University (Canada).

Cohen, L., & Hanratty, T. (1965). Generation of waves in the concurrent flow of air and a liquid. *AIChE Journal*, *11*(1), 138–144.

Comte-Bellot, G., & Corrsin, S. (1966). The use of a contraction to improve the isotropy of grid-generated turbulence. *Journal of Fluid Mechanics*, *25*(4), 657–682.

Conway, J., & Cullen, N. (2013). Constraining turbulent heat flux parameterization over a temperate maritime glacier in New Zealand. *Annals of Glaciology*, *54*(63), 41–51.

Corrsin, S. (1951). On the spectrum of isotropic temperature fluctuations in an isotropic turbulence. *Journal of Applied Physics*, *22*(4), 469–473.

Cuffey, K. M., & Paterson, W. S. B. (2010). *The Physics of Glaciers*. Academic Press.

Denby, B., & Greuell, W. (2000). The use of bulk and profile methods for determining surface heat fluxes in the presence of glacier winds. *Journal of Glaciology*, *46*(154), 445–452.

Denby, B., & Smeets, C. (2000). Derivation of turbulent flux profiles and roughness lengths from katabatic flow dynamics. *Journal of Applied Meteorology and Climatology*, *39*(9), 1601–1612.

Durst, F., Noppenberger, S., Still, M., & Venzke, H. (1996). Influence of humidity on hot-wire measurements. *Measurement Science and Technology*, *7*(10), 1517.

Fitzpatrick, N., Radić, V., & Menounos, B. (2017). Surface energy balance closure and turbulent flux parameterization on a mid-latitude mountain glacier, Purcell Mountains, Canada. *Frontiers in Earth Science*, *5*, 67.

Gatapova, E. Y., Graur, I. A., Kabov, O. A., Aniskin, V. M., Filipenko, M. A., Sharipov, F., & Tadrist, L. (2017). The temperature jump at water-air interface during evaporation. *International Journal of Heat and Mass Transfer*, *104*, 800–812.

Hewes, A., Medvescek, J. I., Mydlarski, L., & Baliga, B. R. (2020). Drift compensation in thermal anemometry. *Measurement Science and Technology*, *31*(4), 045302.

Hinze, J. (1959). *Turbulence*. McGraw-Hill Book Company.

Hock, R. (2005). Glacier melt: A review of processes and their modelling. *Progress in Physical Geography*, *29*(3), 362–391.

Jørgensen, F. E. (2002). *How to Measure Turbulence with Hot-wire Anemometers*. Dantec Dynamics A/S.

Kader, B. (1981). Temperature and concentration profiles in fully turbulent boundary layers. *International Journal of Heat and Mass Transfer*, *24*(9), 1541–1544.

Kantha, L. H., & Mellor, G. L. (1989). A numerical model of the atmospheric boundary layer over a marginal ice zone. *Journal of Geophysical Research: Oceans*, *94*(C4), 4959–4970.

Kendall, J. M. (1970). The turbulent boundary layer over a wall with progressive surface waves. *Journal of Fluid Mechanics*, *41*(2), 259–281.

King, L. V. (1914). On the convection of heat from small cylinders in a stream of fluid: Determination of the convection constants of small platinum wires with applications to hot-wire anemometry. *Philosophical Transactions of the Royal Society of London*, *214*(509-522), 373–432.

Kolmogorov, A. N. (1941). The local structure of turbulence in incompressible viscous fluid for very large Reynolds numbers. *C.R. Acad. Sci. URSS*, *30*, 301–305.

Lemay, J., & Benaïssa, A. (2001). Improvement of cold-wire response for measurement of temperature dissipation. *Experiments in Fluids*, *31*(3), 347–356.

Lepore, J., & Mydlarski, L. (2012). Finite-Péclet-number effects on the scaling exponents of high-order passive scalar structure functions. *Journal of Fluid Mechanics*, *713*, 453–481.

Lepore, J., & Mydlarski, L. (2009). Effect of the scalar injection mechanism on passive scalar structure functions in a turbulent flow. *Physical Review Letters*, *103*(3), 034501.

Lienhard, J., Helland, K. et al. (1989). An experimental analysis of fluctuating temperature measurements using hot-wires at different overheats. *Experiments in Fluids*, *7*(4), 265–270.

Litt, M., Sicart, J.-E., Helgason, W. D., & Wagnon, P. (2015). Turbulence characteristics in the atmospheric surface layer for different wind regimes over the Tropical Zongo glacier (Bolivia, 16°). *Boundary-layer Meteorology*, *154*(3), 471–495.

Litt, M., Sicart, J.-E., Six, D., Wagnon, P., & Helgason, W. D. (2017). Surface-layer turbulence, energy balance and links to atmospheric circulations over a mountain glacier in the French Alps. *The Cryosphere*, *11*(2), 971–987.

Makita, H., & Sassa, K. (1991). Active turbulence generation in a laboratory wind tunnel. In *Advances in turbulence 3* (pp. 497–505). Springer.

Mehta, R. D., & Bradshaw, P. (1979). Design rules for small low speed wind tunnels. *The Aeronautical Journal*, *83*(827), 443–453.

Mestayer, P. (1982). Local isotropy and anisotropy in a high-Reynolds-number turbulent boundary layer. *Journal of Fluid Mechanics*, *125*, 475–503.

Monin, A. S., & Obukhov, A. M. (1954). Basic laws of turbulent mixing in the surface layer of the atmosphere. *Contrib. Geophys. Inst. Acad. Sci. USSR*, *151*(163), e187.

Mott, R., Paterna, E., Horender, S., Crivelli, P., & Lehning, M. (2016). Wind tunnel experiments: Cold-air pooling and atmospheric decoupling above a melting snow patch. *The Cryosphere*, *10*(1), 445–458.

Munro, D. S. (1989). Surface roughness and bulk heat transfer on a glacier: Comparison with eddy correlation. *Journal of Glaciology*, *35*(121), 343–348.

Mydlarski, L. (2003). Mixed velocity–passive scalar statistics in high-Reynolds-number turbulence. *Journal of Fluid Mechanics*, *475*, 173–203.

Mydlarski, L. (2017). A turbulent quarter century of active grids: From Makita (1991) to the present. *Fluid Dynamics Research*, *49*(6), 061401.

Mydlarski, L., & Warhaft, Z. (1996). On the onset of high-Reynolds-number grid-generated wind tunnel turbulence. *Journal of Fluid Mechanics*, *320*, 331–368.

Mydlarski, L., & Warhaft, Z. (1998). Passive scalar statistics in high-Péclet-number grid turbulence. *Journal of Fluid Mechanics*, *358*, 135–175.

Náraigh, L. Ó., Spelt, P. D., Matar, O., & Zaki, T. (2011). Interfacial instability in turbulent flow over a liquid film in a channel. *International Journal of Multiphase Flow*, *37*(7), 812–830.

Natural Resources Canada. (2019). *Canada's Changing Climate Report*. Government of Canada.

Nicholson, L., & Stiperski, I. (2020). Comparison of turbulent structures and energy fluxes over exposed and debris-covered glacier ice. *Journal of Glaciology*, *66*(258), 543–555.

Oboukhov, A. (1949). Structure of the temperature field in turbulent flows. *Isv. Geogr. Geophys. Ser.*, *13*, 58–69.

Oerlemans, J., & Grisogono, B. (2002). Glacier winds and parameterisation of the related surface heat fluxes. *Tellus A: Dynamic Meteorology and Oceanography*, *54*(5), 440–452.

Ohya, Y. (2001). Wind-tunnel study of atmospheric stable boundary layers over a rough surface. *Boundary-Layer Meteorology*, *98*(1), 57–82.

Ohya, Y., Neff, D. E., & Meroney, R. N. (1997). Turbulence structure in a stratified boundary layer under stable conditions. *Boundary-Layer Meteorology*, *83*(1), 139–162.

Overland, J. E. (1985). Atmospheric boundary layer structure and drag coefficients over sea ice. *Journal of Geophysical Research: Oceans*, *90*(C5), 9029–9049.

Pelekasis, N. A., & Tsamopoulos, J. A. (2001). Linear stability of a gas boundary layer flowing past a thin liquid film over a flat plate. *Journal of Fluid Mechanics*, *436*, 321–352.

Pérez-Alvarado, A., Mydlarski, L., & Gaskin, S. (2016). Effect of the driving algorithm on the turbulence generated by a random jet array. *Experiments in Fluids*, *57*(2), 1–15.

Piccirillo, P., & van Atta, C. W. (1997). The evolution of a uniformly sheared thermally stratified turbulent flow. *Journal of Fluid Mechanics*, *334*, 61–86.

Pope, S. (2000). *Turbulent Flows*. doi:10.1017/CBO9780511840531

Prandtl, L. (1925). Bericht über untersuchungen zur ausgebildeten turbulenz. *ZAMM–Zeitschrift für Angewandte Mathematik und Mechanik*, *5*(2), 136–139.

Prandtl, L. (1935). The mechanics of viscous fluids. *Aerodynamic theory*, *3*, 155–162.

Radić, V., Bliss, A., Beedlow, A. C., Hock, R., Miles, E., & Cogley, J. G. (2014). Regional and global projections of twenty-first century glacier mass changes in response to climate scenarios from global climate models. *Climate Dynamics*, *42*(1-2), 37–58.

Radić, V., Menounos, B., Shea, J., Fitzpatrick, N., Tessema, M. A., & Déry, S. J. (2017). Evaluation of different methods to model near-surface turbulent fluxes for a mountain glacier in the Cariboo Mountains, BC, Canada. *The Cryosphere*, *11*(6), 2897–2918.

Richardson, L. F. (1922). *Weather Prediction by Numerical Process*. Cambridge University Press.

Sicart, J. E., Litt, M., Helgason, W., Tahar, V. B., & Chaperon, T. (2014). A study of the atmospheric surface layer and roughness lengths on the high-altitude tropical Zongo glacier, Bolivia. *Journal of Geophysical Research: Atmospheres*, *119*(7), 3793–3808.

Stiperski, I., Holtslag, A. A., Lehner, M., Hoch, S. W., & Whiteman, C. D. (2020). On the turbulence structure of deep katabatic flows on a gentle mesoscale slope. *Quarterly Journal of the Royal Meteorological Society*, *146*(728), 1206–1231.

Stull, R. B. (1988). *An Introduction to Boundary Layer Meteorology*. Springer Science & Business Media.

Sullivan, P. P., & McWilliams, J. C. (2002). Turbulent flow over water waves in the presence of stratification. *Physics of Fluids*, *14*(3), 1182–1195.

Sullivan, P. P., McWilliams, J. C., & Moeng, C.-H. (2000). Simulation of turbulent flow over idealized water waves. *Journal of Fluid Mechanics*, *404*, 47–85.

Suter, S., Hoelzle, M., & Ohmura, A. (2004). Energy balance at a cold Alpine firn saddle, Seserjoch, Monte Rosa. *International Journal of Climatology: A Journal of the Royal Meteorological Society*, *24*(11), 1423–1442.

Sverdrup, H. (1935). The ablation on Isachsen's Plateau and on the fourteenth of july glacier in relation to radiation and meteorological conditions. *Geografiska Annaler*, *17*(3-4), 145–166.

Taylor, G. I. (1938). The spectrum of turbulence. *Proceedings of the Royal Society of London. Series A-Mathematical and Physical Sciences*, *164*(919), 476–490.

Taylor, J. (1997). *An Introduction to Error Analysis: The Study of Uncertainties in Physical Measurements*. University Science Books.

Tennekes, H., & Lumley, J. L. (1972). *A First Course in Turbulence*. doi:10.7551/mitpress/3014.001.0001

Webb, E. K. (1970). Profile relationships: The log-linear range, and extension to strong stability. *Quarterly Journal of the Royal Meteorological Society*, *96*(407), 67–90.

Williams, O., Hohman, T., Van Buren, T., Bou-Zeid, E., & Smits, A. J. (2017). The effect of stable thermal stratification on turbulent boundary layer statistics. *Journal of Fluid Mechanics*, *812*, 1039–1075.

Yoon, K., & Warhaft, Z. (1990). The evolution of grid-generated turbulence under conditions of stable thermal stratification. *Journal of Fluid Mechanics*, *215*, 601–638.

Appendices

Appendix A: Noise Reduction

Like any electronic measurement device, hot-wire anemometers and cold-wire thermometers can be prone to measuring high-frequency electronic noise that is not part of the turbulent velocity or temperature signal. Signal conditioning is typically performed to minimize the effects of electronic noise, but in some cases (including the present work), additional post-processing is required. For example, consider a typical spectrum of the cold-wire noise measured at the centreline of the empty wind tunnel with no thermal forcing, presented in Figure A.1. There is an unavoidable amount of electronic (and other) noise in the signal, such as the electronic noise characterized by the large peaks at 60 Hz and 120 Hz. Therefore, post-processing was needed to remove the influences of electronic noise from the velocity and temperature statistics. In the present work, electronic noise was removed from the results in two different ways, which are described below.

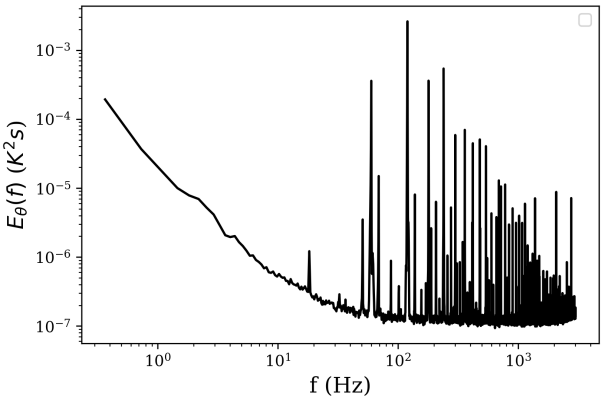

Figure A.1: Temperature noise spectrum measured in the empty tunnel with no temperature forcing at $U_\infty = 3.2$ m/s.

A.1 Removal of Noise from Temperature Statistics

When calculating the statistics of the temperature fluctuations, there is always a certain amount of noise added to the cold-wire signal. Since knowing the magnitude of this instantaneous noise at any point in time is impossible, the noise was removed on a statistical basis. To this end, it was assumed that the measured voltage fluctuation (e_m) of

the CCA was the sum of the true voltage (e_t) and voltage arising from electronic noise (e_n), such that:

$$e_m = e_t + e_n. \tag{A.1}$$

The variance of the measured voltage is then:

$$\left\langle e_m^2 \right\rangle = \left\langle e_t^2 + 2e_t e_n + e_n^2 \right\rangle, \tag{A.2}$$

which can be simplified to:

$$\left\langle e_m^2 \right\rangle = \left\langle e_t^2 \right\rangle + \left\langle e_n^2 \right\rangle + 2\left\langle e_t e_n \right\rangle. \tag{A.3}$$

Assuming that the true voltage and noise voltage are uncorrelated (such that their covariance is zero) is a reasonable assumption since the two arise from independent physical phenomena. The true variance can then be obtained as follows:

$$\left\langle e_t^2 \right\rangle = \left\langle e_m^2 \right\rangle - \left\langle e_n^2 \right\rangle. \tag{A.4}$$

By measuring the cold-wire voltage before each run, in the same flow without any significant temperature fluctuations, the variance of the noise was be obtained and used to find the true temperature variance of the cold-wire for the experiments. In this work, the noise variance was typically around $0.0081°\mathrm{C}^2$.

A.2 Removal of Electronic Noise from Spectra

In the present work, an algorithm was used to remove peaks from the spectra that were characteristic of electronic noise, replacing them with values more representative of the true signal. From KOC theory, it is known that the spectra of velocity and temperature fluctuations should be decreasing functions of frequency once in the inertial subrange of the turbulent cascade (Tennekes & Lumley, 1972). As such, any peaks observed at

frequencies of 60 Hz or higher can be reasonably assumed to be caused by electronic noise.

To detect anomalous peaks on the frequency spectrum ($E(f)$) at point i, beginning at $f_i = 60$ Hz, the two previous points (at $i-1$ and $i-2$) were used to predict the value of the spectra at point i using a linear approximation of the local gradient. The next point (at $i+1$) was never used, since it may have been an anomalous peak. If the ratio of the true value ($E(f_i)_{true}$) to the predicted value ($E(f_i)_{pred}$) was greater than 1.05, then $E(f_i)_{true}$ was assumed to be contaminated by electronic noise, and replaced by $E(f_i)_{pred}$. This process was repeated until the end of the spectrum was reached.

The use of this method allowed the shape of the spectra to be preserved, while only removing unwanted peaks related to the electronic noise. The threshold ratio for replacement, $R_r = \frac{E(f_i)_{meas}}{E(f_i)_{pred}}$, was selected to be 1.05 such that it was similar to the experimental uncertainty present in the velocity measurements. The average change in variance (i.e., the integral under the spectra) resulting from this process was approximately 2% for the velocity, and 4% for the temperature. The higher change in variance for the temperature measurements is reasonable, given that: i) cold-wire thermometry is generally more sensitive to electronic noise; and ii) the signal-to-noise ratio for the cold-wire was lower than that of the hot-wire. A typical example of the spectra shown before and after this noise removal process is presented in Figure A.2.

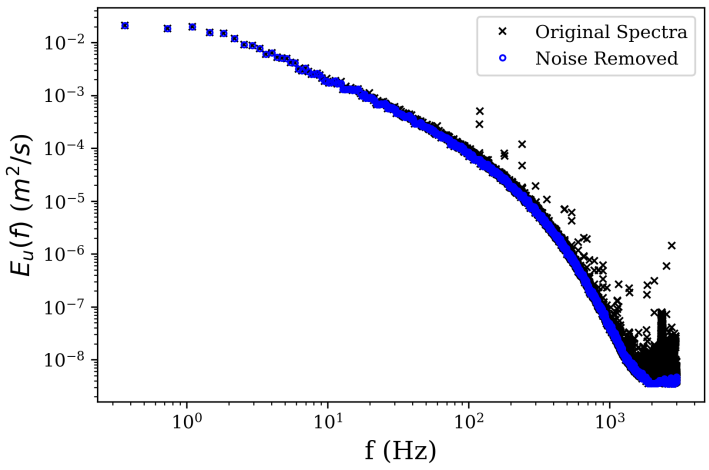

Figure A.2: Velocity spectra before and after noise removal using spectral smoothing method.

Appendix B: Uncertainty Analysis

This appendix summarizes and quantifies the important sources of error associated with the measurements of both temperature and velocity in the present work, as well as those errors involved in estimating the height of the measurement probe.

B.1 Cold-wire Temperature Measurements

The main sources of uncertainty in the cold-wire temperature measurements are the resolution of the Type E thermocouple used for calibration, error associated with the data acquisition, error associated with fitting the calibration curve, and probe positioning error.

Sensitivity to velocity changes, the presence of electronic noise, and limited frequency response are also potential sources of error when using a constant current anemometer. However, these sources of error were deemed negligible since: i) the current was selected to minimize sensitivity to velocity changes; ii) the effect of electronic noise was compensated for; and iii) the quantities investigated in this work are large-scale in nature, and thus the small-scale (high-frequency) features of the flow that approach the frequency response of the sensor do not significantly contribute to the results herein.

Thermocouple Resolution Error

The resolution of the Type E thermocouple used for calibration of the cold-wire was 0.1°C. Assuming that the error is uniformly distributed, the relative uncertainty (ξ) can be approximated as:

$$\xi_{res} = \frac{1}{\sqrt{3}} \left(\frac{0.1}{\Delta T_{max}} \right), \tag{B.1}$$

where ΔT_{max} is the maximum mean temperature defect of the flow (when compared to the ambient temperature). Taking this to be 12°C, the relative uncertainty from the thermocouple resolution is approximately 0.48%.

Data Acquisition Board Error

Since the data acquisition board converts analog voltage to a digital number, there is some error associated with this conversion. Again assuming a uniformly distributed error, following the expression of Jørgensen (2002), the relative error from the data acquisition board can be estimated as:

$$\xi_{DAQ} = \frac{1}{\sqrt{3}} \frac{1}{\Delta T_{max}} \frac{\partial T}{\partial E} \frac{E_{DAQ}}{2^n}. \tag{B.2}$$

Using the slope of the calibration curve ($\frac{\partial T}{\partial E} = 2.6469°C/V$), voltage span of the DAQ card (10 V), and 16-bit resolution (where n is 16), the relative uncertainty from the DAQ board is approximately 0.002%.

Calibration Error

After accounting for errors in the measurement of voltages and temperatures, it is possible to estimate the uncertainty from fitting the linear calibration equation to the calibration data. For each point i in the calibration curve, the mean-square error between the predicted temperature T_{pred} using the calibration equation and the true temperature T_{true} is used to estimate the calibration uncertainty as:

$$\xi_{cal} = \sqrt{\frac{1}{N-2} \sum_{i=1}^{N} \left(\frac{T_{pred} - T_{true}}{T_{pred}} \right)^2}. \tag{B.3}$$

The relative calibration uncertainty was found to be 0.002%.

Probe Positioning Error

The last source of uncertainty in the temperature measurements is from error associated with positioning of the measurement probe above the surface. As a conservative estimate, an error of 0.5mm is taken as the uncertainty associated with the height (Δy) of the probe, with a uniformly distributed error. To conservatively estimate the effect of the uncertainty in the height on the temperature measurements, the following expression is

used:

$$\xi_{pos} = \frac{1}{\sqrt{3}} \frac{1}{T_{min}} \frac{\partial T}{\partial y} \Delta y. \tag{B.4}$$

However, since the experiments taken over melting ice were transient in nature, taking instantaneous profile measurements of temperature was not undertaken. This prevents the calculation of $\frac{\partial T}{\partial y}$, which is needed to estimate the positioning error. To overcome this challenge, it was assumed that non-dimensional profiles of temperature were approximately equal to non-dimensional profiles of velocity, so that the following assumption was made:

$$\frac{\partial (U/U_\infty)}{\partial y} \approx \frac{\partial \left(\frac{T - T_s}{T_\infty - T_s} \right)}{\partial y}. \tag{B.5}$$

The approximate non-dimensional slope was 0.01 mm^{-1} at the lowest measurement height (which maximizes the uncertainty). Using this value, taking the free-stream temperature (T_∞) to be 18°C, and taking the approximate surface temperature from the embedded thermocouple (T_s) to be 0°C, it is possible to estimate $\frac{\partial T}{\partial y}$ using:

$$0.01 \approx \frac{\partial \left(\frac{T - T_s}{T_\infty - T_s} \right)}{\partial y} = \left(\frac{1}{T_\infty - T_s} \right) \left(\frac{\partial T}{\partial y} - \frac{\partial T_s}{\partial y} \right). \tag{B.6}$$

Therefore, the relative uncertainty in temperature with probe positioning was found to be 0.087%.

Overall Temperature Measurement Uncertainty

The total uncertainty from all significant error sources in the temperature measurements is estimated as:

$$\xi_{tot} = 2\sqrt{\xi_{res}^2 + \xi_{DAQ}^2 + \xi_{cal}^2 + \xi_{pos}^2}. \tag{B.7}$$

A factor of 2 is applied in order to have a 95% confidence level in the uncertainty. Using this factor, the overall uncertainty ξ_{tot} in the cold-wire temperature measurements was 0.97%.

B.2 Hot-wire Velocity Measurements

Similar to the temperature measurements, the main sources of error in the velocity measurements are from error associated with the calibration equipment, data acquisition board, calibration curve fits, and probe positioning. Since the hot-wire measurements are also sensitive to temperature, which is calculated using the cold-wire, this error must also be included.

Some other potential sources of error include humidity, drift, electronic noise, and frequency response. As discussed in Section 3.4, the effects of humidity were deemed negligible for the flows investigated in this work. Electronic noise is less significant for hot-wire anemometry than cold-wire thermometry since the signal-to-noise ratio is typically larger. The effects of hot-wire drift were deemed negligible since: i) a large top resistor was used in the Wheatstone bridge for the Dantec Streamline Pro anemometer (20Ω); ii) the wires were burned in for 24 hours before initial use, minimizing the effects of drift associated with annealing of the hot-wire sensor; and iii) changes in ambient wire resistance with temperature were accounted for when making simultaneous velocity and temperature measurements.

Calibration Jet Error

The jet used to calibrate the hot-wires has a relative uncertainty (ξ_{jet}) of 1% (Jørgensen, 2002), assuming a random normally distributed error.

Data Acquisition Board Error

Similar to the temperature measurements, the error associated with the data acquisition board is assumed to be random and uniformly distributed, such that its relative uncertainty can be estimated as (Jørgensen, 2002):

$$\xi_{DAQ} = \frac{1}{\sqrt{3}} \frac{1}{U_{min}} \frac{\partial U}{\partial E} \frac{E_{DAQ}}{2^n}. \tag{B.8}$$

Estimating the data acquisition uncertainty ξ_{DAQ} is more complex for the velocity measurements than for the temperature measurements. Using the modified King's Law equation, the velocity is found as:

$$U = \left(\frac{E^2 - A^*}{B^*} \right)^{1/\bar{n}}. \tag{B.9}$$

Since the coefficients A^* and B^* are not constant, an iterative code was created in Python to evaluate the data acquisition error by analytically finding the slope of the calibration curve for each point as:

$$\frac{\partial U}{\partial E} = \frac{1}{\bar{n}} \left(\frac{2E}{B^*} \right) \left(\frac{E^2 - A^*}{B^*} \right)^{\frac{1}{\bar{n}} - 1}. \tag{B.10}$$

The value which maximized the ratio of the slope of the calibration curve to the velocity was used to estimate the error. Using this method, the data acquisition error was found to be 0.16%.

Calibration Error

The calibration error for the velocity measurements is significantly more complex than for the temperature measurements, since the coefficients used to calculate the velocity from voltage are sensitive to changes in temperature. As a result, it the errors associated with estimating (and curve-fitting) the coefficients A^* and B^* must be included in the velocity calibration error. The relative uncertainty in the velocity calibration ξ_{cal} can be estimated as:

$$\xi_{cal} = \sqrt{\frac{1}{N-3} \sum_{i=1}^{N} \left(\frac{U_{pred} - U_{true}}{U_{pred}} \right)^2 + \left(\frac{1}{U} \sigma_{A^*} \right)^2 + \left(\frac{1}{U} \sigma_{B^*} \right)^2}. \tag{B.11}$$

As in the temperature calibration, the sum of square error between the predicted velocity U_{pred} and true velocity U_{true} is used as part of the uncertainty. It is divided by $N-3$ since there are 3 degrees of freedom (for calibration coefficients A^*, B^*, and n). The other two terms account for the relative uncertainty in velocity from curve-fitting A^* and B^* using the theory of propagation of uncertainties (Taylor, 1997). Here, the values σ_{A^*} and σ_{B^*}

are found as:

$$\sigma_{A^*} = \sqrt{\frac{1}{N-2}\sum_{i=1}^{N}(A^*_{pred} - A_{true})^2 + \left(\frac{\partial A}{\partial T}\Delta T\right)^2}, \tag{B.12}$$

$$\sigma_{B^*} = \sqrt{\frac{1}{N-2}\sum_{i=1}^{N}(B^*_{pred} - B_{true})^2 + \left(\frac{\partial B}{\partial T}\Delta T\right)^2}, \tag{B.13}$$

where the predicted values of A^* and B^* are found using the curve fit equations (3.8 and 3.9, respectively), and ΔT is the maximum variation of the calibration jet temperature during one constant-temperature calibration curve (approximately 0.2°C).

Similar to the data acquisition board error (ξ_{DAQ}), these quantities are not constant. To conservatively estimate the calibration error, a Python code was written to find the maximum calibration error. Using this method, the calibration error was found to be 1.63%.

Another point worth mentioning regarding the hot-wire calibration is the effect of the wire orientation, especially at lower flow speeds. In the calibration jet, the mean flow was in the vertical direction (parallel to the direction of natural convection from the hot-wire). However, in the experimental set-up, a 90° elbow was used to orient the hot-wires such that the mean flow was perpendicular to the direction of natural convection. Thus, at low speeds, it is important to consider contributions of natural convection to the total heat transfer from the wire to surrounding air, potentially artificially increasing the apparent velocity. The Grashof number, Gr_D is a non-dimensional quantity which represents the ratio of buoyant to viscous forces for a cylinder with diameter D. It is defined as:

$$Gr_D \equiv \frac{g\beta(T_s - T_\infty)D^3}{\nu^2}, \tag{B.14}$$

where β is the coefficient of volumetric expansion, which can be approximated as $1/T_f$ for an ideal gas, where T_f is the film temperature between the cylinder surface and ambient fluid (Bergman et al., 2011).

The Grashof number can be used with the Reynolds number to find the Archimedes number (Ar), which represents the ratio of natural to forced convection, and is defined

as:

$$Ar \equiv \frac{Gr}{Re^2}. \tag{B.15}$$

The hot-wire calibration procedure assumes a regime in which forced convection dominates the heat transfer from the wire surface, such that $Ar \ll 1$. To evaluate the significance of natural convection to the total heat transfer from the hot-wire, the maximum Archimedes number was calculated using the minimum flow speed (1.0 m/s), minimum ambient temperature in the calibration jet (12°C), average wire temperature (500 K), and wire diameter (5 μm). Using these values, the maximum Archimedes number was found to be approximately 9.3 x10^{-5}, ultimately suggesting that the effects of natural convection are negligible even for the lowest flow speeds used in the calibration and testing procedures.

Probe Positioning Error

The error associated with probe positioning was once again found by assuming a random and uniformly distributed error in the relative height. The same 0.5 mm value of Δy was used to estimate the uncertainty ξ_{pos} as:

$$\xi_{pos} = \frac{1}{\sqrt{3}} \frac{1}{U_{min}} \frac{\partial U}{\partial y} \Delta y. \tag{B.16}$$

The maximum slope of the velocity profile was found to be 0.015 m/s mm^{-1}. Using the minimum velocity measured in the experiments (0.7 m/s), the probe positioning uncertainty ξ_{pos} was estimated to be 0.62%.

Temperature Error

The velocity measurements are also sensitive to temperature, since it is used to calculate the coefficients A^* and B^* used in the calibration equation. The cold-wire temperature values are used for this purpose, so the total cold-wire temperature uncertainty (i.e. the value before the factor of 2) is used to estimate the uncertainty of the temperature

measurements on the velocity. This uncertainty (ξ_{CCA}) was 0.49%.

Overall Velocity Measurement Uncertainty

The total uncertainty from all significant error sources in the velocity measurements is estimated as:

$$\xi_{tot} = 2\sqrt{\xi_{jet}^2 + \xi_{DAQ}^2 + \xi_{cal}^2 + \xi_{pos}^2 + \xi_{tem}^2}. \tag{B.17}$$

Once again, a factor of 2 is applied in order to have a 95% confidence level in the uncertainty. Using this factor, the overall uncertainty ξ_{tot} in the hot-wire velocity measurements was 4.1%. It is important to note that this uncertainty is a conservative estimate, found by taking the maximum possible uncertainty for each of the potential error sources in the measurements.

As a way to verify this uncertainty, the velocity error (in percent) was calculated for each data point in the calibration procedure using the true and calculated velocities. The results for both hot-wire channels are shown in Figure B.1, where it is shown that the calculated velocity is typically within 2% of the true velocity, but the error can be as high as 3.5% for very low flow speeds. In all cases, the error was below the 4.1% range calculated above for 95% confidence.

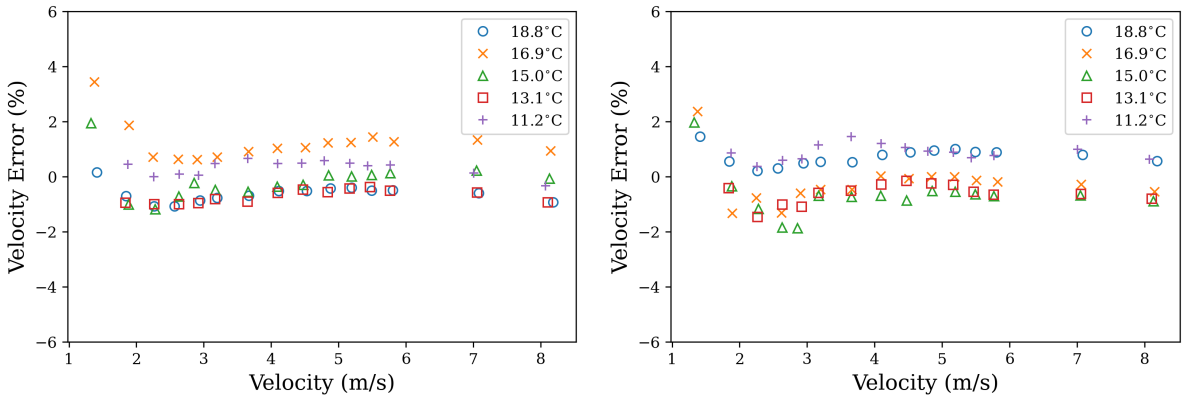

(a) Wire 1 (b) Wire 2

Figure B.1: Absolute velocity error as a percentage of true velocity.

B.3 Surface Temperature Error

The main sources of error in the surface temperature measurements were the thermocouple resolution error and the positioning error.

Thermocouple Resolution Error

As for the cold-wire measurements, the resolution of the Type E thermocouple was also assumed to be uniformly distributed, with a 0.1°C resolution. The ice temperatures were initially sub-zero and increased to approximately 0°C, where it remained for most of the experiments. Since the sub-surface thermocouple was used primarily for absolute temperature measurements (and not temperature differential measurements, unlike the cold-wire), units of Kelvin are used to estimate its error. As a result, the mean sub-surface temperature $\langle T_{ss} \rangle$ (calculated to be -1°C, or 272 K) was used to estimate the thermocouple resolution error as:

$$\xi_{res} = \frac{1}{\sqrt{3}} \frac{0.1}{\langle T_s \rangle}, \tag{B.18}$$

such that the thermocouple resolution error (ξ_{res}) was found to be approximately 0.021%.

Thermocouple Positioning Error

Since the thermocouple could not be positioned exactly on the surface of the ice, it was instead embedded below the surface at a depth of approximately 10 mm. Due to the change in temperature with depth, there was an error associated with the positioning of the thermocouple:

$$\xi_{pos} = \frac{1}{\sqrt{3}} \frac{1}{\langle T_s \rangle} \frac{\partial T}{\partial y} \Delta y, \tag{B.19}$$

where it is assumed that the error in positioning is uniformly distributed. The mean surface temperature $\langle T_s \rangle$ was once again taken to be approximately 272 K, and the uncertainty in position Δy was estimated to be approximately 2 mm. The temperature

gradient inside the ice, $\frac{\partial T}{\partial y}$ was estimated using the typical melt energy heat flux (Q_m) calculated from the meltwater mass measured after each experiment (where $Q_m = \frac{m \times L_f}{t \times A}$), and was found to be approximately 320 $\frac{W}{m^2}$. Assuming a one-dimensional temperature distribution inside the ice, and using Fourier's Law:

$$Q_m = -k_{ice} \frac{\partial T}{\partial y}, \tag{B.20}$$

the temperature gradient was estimated to be approximately 145 K/m (using k_{ice}=2.2 $\frac{W}{m \cdot K}$). With these values, the positioning error ξ_{pos} was estimated as 0.062%.

Overall Surface Temperature Measurement Uncertainty

The total uncertainty from all significant error sources in the ice surface temperature measurements is estimated as:

$$\xi_{tot} = 2\sqrt{\xi_{res}^2 + \xi_{pos}^2}, \tag{B.21}$$

wherein it was found that the total uncertainty associated with the sub-surface thermocouple embedded in the ice was 0.13% for a 95% confidence interval, corresponding to an absolute error of approximately 0.35 K for a 272 K temperature measurement.

B.4 Reference Height Error

The final important source of error in the experiments is involved with setting the probe height above the ice surface. Since the reference (i.e. "zero") height had to be determined visually before moving the probe to the measurement height, there is some error involved with the estimations of the true measurement height. As mentioned previously, the cylindrical shape of the probe restricted the minimum height between the hot- or cold-wire to be one millimetre above the surface. However, the probe was brought close enough to the surface that there would be apparent contact between the probe apparatus and the

ice surface. The error associated with the precision of the reference height is estimated to be approximately 0.5 mm, since this was the minimum distance used to adjust the probe at any point. Figure B.2 shows the probe positioned to a typical "zero" height.

Figure B.2: Probe positioned at "zero" reference height.

This uncertainty in the true height is somewhat compounded by the fact as the ice melts into water, the surface itself will regress away from the probe as the water contracts during the melting process. It was assumed that the overall change in height due to the contraction of water upon melting was negligible, since typically 90% of the ice mass remained frozen during the experiment, and therefore could be absorbed into the 0.5 mm probe positioning uncertainty.

Appendix C: Repeatability of Measurements

The repeatability of the experiments performed in this work was verified by taking repeat runs for three of the nine total test cases. The velocity statistics of the repeat runs are presented below in Table C.1. It can be seen that the repeatability of the velocity statistics is within the 4.1% uncertainty. The repeatability of the relevant temperature statistics (θ_{rms} and $\langle v\theta \rangle$) was also evaluated in time for each of the three cases presented above. The results are shown in Figures C.1 and C.2.

Achieving adequate repeatability in temperature statistics was much more challenging than for the velocity measurements. The velocity field measurements were found to be relatively insensitive to changes in the instantaneous temperature caused by day-to-day variations in T_∞ or T_s. On the other hand, temperature measurements were sensitive to the ambient tunnel temperature T_∞, the surface temperature T_s, and the measurement height. While the influence of variations in the ambient temperature and error in the measurement height were not expected to be significant to the temperature results, variations in the internal ice temperature had a significant influence on the measured statistics in the boundary layer – particularly on θ_{rms} and $\langle v\theta \rangle$.

The effect of varying ice temperatures, and subsequently ice melt rates, was minimized by beginning each run at the same surface temperature reading (approximately -10°C). However, this technique would not guarantee identical ice melting between experiments, even if other conditions were similar. This was because the temperature distribution inside the entire ice tray was impossible to know before starting an experiment – only the temperature at a single depth was known. Differences in internal temperature distri-

U_∞ (m/s)	y (mm)	$\langle U \rangle$ (m/s)	u_{rms} (m/s)	v_{rms} (m/s)	Ti (%)	-$\langle uv \rangle$ (m^2/s^2)	-ρ_{uv}
1.1	10	0.87	0.110	0.036	12.6	0.0013	0.33
1.1	10	0.85	0.106	0.035	13.3	0.0013	0.35
2.0	25	1.70	0.197	0.097	11.6	0.0077	0.40
2.0	25	1.63	0.193	0.095	11.7	0.0075	0.41
3.2	40	2.75	0.279	0.173	10.1	0.0157	0.33
3.2	40	2.84	0.284	0.176	10.0	0.0162	0.32

Table C.1: Velocity statistics for repeat runs

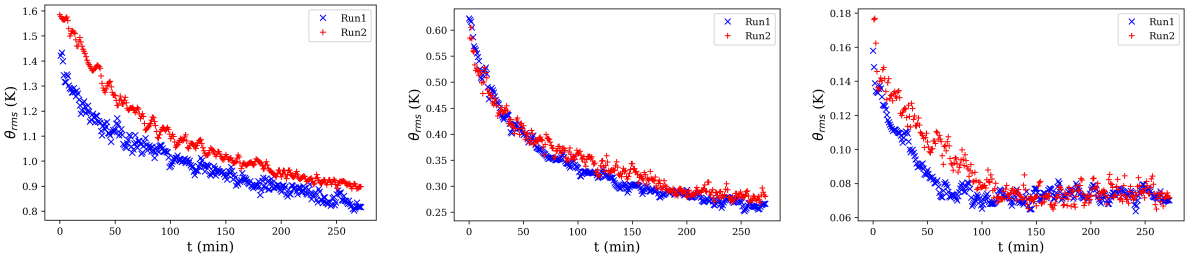

(a) U_∞=1.1 m/s, y=10 mm (b) U_∞=2.0 m/s, y=25 mm (c) U_∞=3.2 m/s, y=40 mm

Figure C.1: Dimensional RMS temperature repeatability.

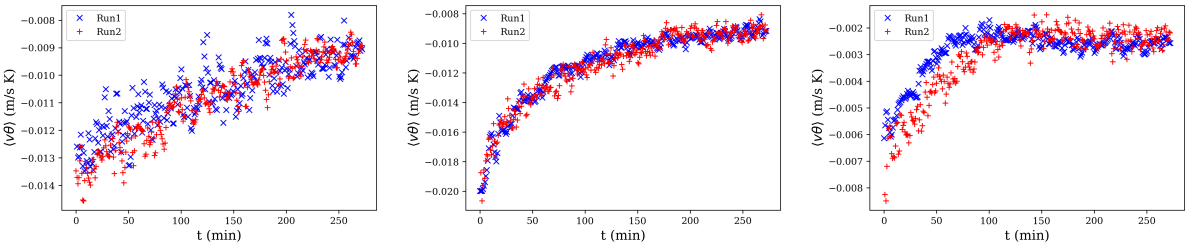

(a) U_∞=1.1 m/s, y=10 mm (b) U_∞=2.0 m/s, y=25 mm (c) U_∞=3.2 m/s, y=40 mm

Figure C.2: Turbulent heat flux repeatability.

butions would influence the melt rate of the ice, thereby influencing the evolution of the temperature statistics.

Despite these challenges, the repeatability of the RMS temperature evolution in time is shown to be reasonable in Figure C.1. Although in some cases, the internal ice temperature may cause the evolution to be slightly different for repeat runs, the overall trend in the evolution of the RMS temperature fluctuation displays sufficient repeatability. The turbulent heat flux (Figure C.2) shows better dimensional repeatability than the RMS temperature, especially for case (a). This may be a result of the velocity measurements having better repeatability than the temperature repeatability, such that the mixed (velocity-temperature) statistic will have repeatability that lies somewhere between its two individual components.